UC Santa Barbara
UC Santa Barbara Electronic Theses and Dissertations

Title
Porous GaN in LEDs and Lasers

Permalink
https://escholarship.org/uc/item/5gt0s3zw

Author
Anderson, Ryan

Publication Date
2022

Peer reviewed|Thesis/dissertation

eScholarship.org Powered by the California Digital Library
University of California

University of California, Santa Barbara

Porous GaN in LEDs and Lasers

A dissertation submitted in partial satisfaction of the requirements for the degree

Doctor of Philosophy in Materials

By Ryan Anderson

Committee in charge:

Professor Steven P. DenBaars, Chair

Professor Shuji Nakamura

Professor James S. Speck

Professor Umesh Mishra

September 2023

The dissertation of Ryan Anderson is approved.

____
James S. Speck

____
Shuji Nakamura

____
Umesh Mishra

____
Steven P. DenBaars (Committee Chair)

July 2022

Acknowledgements:

I am incredibly fortunate to have been surrounded by outstanding mentors.

I have Dr. Kathy Doverspike to thank for fostering my scientific career. I thank Prof. Steve DenBaars for giving me freedom on my projects and allowing me to study abroad in Malaysia. I was lucky to work with Dr. Dan Cohen. He says that many successful careers have been made off just chapter 2 in Coldren's book on laser diodes, but I would wager Dan has led to more. I thank him and hope one day I can pay his generosity forward.

It was a real pleasure working with fellow laser folks Jared, Haojun, Emily, Nathan, and Matt. Thank you for being locked up with me at Del Norte Nick, Antoine, Allegra, Jordan, Emma, and Ryan. Learning to surf with Kan was a welcome reprieve. But visiting Adi in the Bay has made everything better, where I'm happy to finally be moving.

Finally, thank you Mom and Dad for always encouraging me to take my own path.

Curriculum Vitae

Ryan Anderson

randerson@ucsb.edu

• Ph.D. candidate with ten years of R&D experience in academia and industry
• Developed design, growth, and fabrication of III-nitride LEDs and laser diodes

Education

University of California Santa Barbara **Sep 2017 – Jul 2022**
Ph.D. in Materials, Advisor: Steven DenBaars

University of Notre Dame **Sep 2009 - May 2013**
B.S. in Chemical Engineering

Work Experience

Graduate Student Researcher **Sep 2017-Present**
University of California Santa Barbara, CA

• Designed, grew, and fabricated III-nitride devices using metalorganic chemical vapor deposition (MOCVD), extensive characterization, and university cleanroom
• Implemented novel material porous GaN into devices leveraging unique properties

Project: High performance blue and green edge emitting laser diodes (EELDs)
• Demonstrated electrically injected EELDs using porous GaN cladding
• Quantified detrimental effects of scattering loss of porous GaN in EELDs
• Widened operating wavelength with low threshold and high efficiency

Project: Long wavelength microLEDs on silicon substrates
• Employed flexible porous templates for strain management of InGaN grown on Si

Project: Porous GaN based mirrors in vertical cavity surface emitting lasers
• Created high reflectivity mirrors with porous GaN
• Formulated simple process flow reducing VCSEL fab development time

Process Development Engineer **Jun 2013-Jul 2017**
Cree - Durham, NC
R&D for epitaxial growth of gallium nitride LEDs
• Used MOCVD to grow high brightness and efficiency GaN LEDs
• Generated lower cost, higher efficiency products using statistical analysis
• Innovated growth on alternative substrates leading to integration into factory lines
• Owned starting up experimental MOCVD reactors from assembly to production
• Devised changes to wafer carrier design, temperature targeting for higher yield
• Trained new engineers in R&D epitaxial growth department

Undergraduate Student Researcher **May 2011-May 2013**
University of Notre Dame, IN
Density functional theory study of nitrous oxide reduction (Senior Thesis)
• Simulated catalytic converter reactions for better understanding of NO_x reduction

Technical Engineering Co-op **May 2012 - Sep 2012**
General Electric - Cleveland, OH
Investigation of iron contamination in fluorescent lamps
• Diagnosed drop in lamp brightness from impurities in phosphor coatings

Technical Skills and Software

Experienced: MOCVD, material growth, GaN, process development,
photolithography, SEM, FIB, XRD, SIMS, JMP, Origin
Proficient: Lumerical (MODE), Fimmwave, Matlab, LabView, R, SQL, L-edit

Honors

• Outstanding Graduate Student Research Achievement Award 2020-2021
• Holbrook Foundation Fellowship 2018-2019
• University of Notre Dame Academic Dean's List 2013
• Loretta & John Kelly Scholarship, Pat & Cheryl Simpson Scholarship 2011-2013
• University of Notre Dame Provost's Scholarship 2009-2013

Publications

• **R. Anderson**, H. Zhang, E. Trageser, N. Palmquist, S. Nakamura, S. DenBaars, "Green edge emitting lasers with novel porous GaN cladding," *Optics Express, Under Review*, 2022
• P. Li, H. Zhang, H. Li, T. Cohen, **R. Anderson**, M. Wong, E. Trageser, T. Chow, M. De Vries, S. Nakamura, S. DenBaars, "Demonstration of 568 nm Stimulated Emission from Optically Pumped InGaN/GaN Multi-Quantum Wells" Submitted to App. Phys. Let., *Under Review*, 2022
• **R. Anderson**, D. Cohen, H. Zhang, E. Trageser, N. Palmquist, S. Nakamura, and S. DenBaars, "Nano-porous GaN cladding and scattering loss in edge emitting laser diodes," Opt. Express 30, 2759-2767, 2022
• S. Gandrothula, H. Zhang, P. Shapturenka, **R. Anderson**, M. Wong, H. Li, T. Kamikawa, S. Nakamura, and S. DenBaars, "Semipolar {20-21} GaN Edge-Emitting Laser Diode on Epitaxial Lateral Overgrown Wing " Crystals 11, no. 12: 1563, 2021
• S. Gandrothula, T. Kamikawa, P. Shapturenka, **R. Anderson**, M. Wong, H. Zhang, J. Speck, S. Nakamura, and S. Denbaars, "Optical and electrical characterizations of micro-LEDs grown on lower defect density epitaxial layers", Appl. Phys. Lett. 119, 142103, 2021
• G. Lheureux, M. Monavarian, **R. Anderson**, R. Decrescent, J. Bellessa, C. Symonds, J. Schuller, J. S. Speck, S. Nakamura, and S. DenBaars, "Tamm plasmons in metal/nanoporous GaN distributed Bragg reflector cavities for active and passive optoelectronics," Opt. Express 28, 17934-17943, 2020

• **R. Anderson**, D. Cohen, S. Mehari, S. Nakamura, and S. DenBaars, "Electrical injection of a 440nm InGaN laser with lateral confinement by nanoporous-GaN," Opt. Express 27(16), 22764-22769, 2019 **Editor's Choice**

Conference Presentations

• SPIE Photonics West - San Francisco, CA
Jan 2022

• Universal Broadband Active PIC Platform DARPA program review - Remote
Dec 2021

• Solid State Lighting & Energy Electronic Center review - Goleta, CA
Fall 2018, 2019, 2021

• International Conference of Semiconductor Materials and Technology – Malaysia
May 2018

Abstract

Porous GaN in LEDs and Lasers

By Ryan Anderson

Central to the LED lighting revolution, optoelectronics based on III-nitride materials have far-reaching applications in consumer displays, visible light communication, industrial, defense, and scientific markets. Development of (Al,In,Ga)N material growth and fabrication has matured yielding blue LEDs and laser diodes with outstanding efficiency. New technologies are needed to expand the applicable wavelength of GaN emitters. The unique optical and mechanical properties of porous GaN enable potential to disrupt traditional µLEDs, edge emitting laser diodes, and vertical cavity surface emitting lasers.

Blue laser diodes rely on index contrast provided by AlGaN or InGaN in lower cladding, but defects introduced through lattice mismatch limit the thickness and composition. Porous GaN is not only lattice matched to GaN, but has a high index contrast, making it an ideal candidate for optical confinement. Several batches of edge emitting lasers were fabricated with porous GaN. Lateral mode confinement was observed by a tapering 20% porous layer, allowing estimates for the electrical and thermal properties. Lasers with porous cladding reached threshold at 4 kA/cm^2 under pulsed operation at a wavelength of 454 nm. The low slope efficiency of 0.24 W/A and considerable excess loss over 60 cm^{-1} was attributed to scattering in parasitic porous layers. Laser action was observed under continuous wave operation with thermal rollover due to internal heating. Green lasers with porous cladding at 510 nm were fabricated fixing the etch selectivity with slope efficiency of 0.13 W/A and

threshold current density of 14 kA/cm^2. The much lower voltage kept the peak wall plug efficiency of 0.9% comparable to typical research lasers at these wavelengths, but the combination of low injection efficiency and high loss cause performance to lag behind state-of-the-art.

The dearth of high index contrast III-nitride material similarly affects visible wavelength vertical cavity surface emitting lasers. GaN VCSELs have complex fabrication schemes or excessively long difficult growths. Instead, porous GaN can be used to make epitaxial high reflectivity mirrors by electrochemical etching. Porous GaN mirrors were fabricated exhibiting more than 95% reflectivity at the target wavelength. Hybrid VCSEL cavities constructed with porous GaN and dielectric mirrors demonstrated electroluminescent spectra with narrow emission modes, but no laser action.

Improving longer wavelength efficiency also requires high quality active material. Porous GaN enables a novel method to mechanically relax InGaN and incorporate higher indium content at higher growth temperature. While this has been achieved on sapphire substrates, there are benefits and challenges associated with heterogeneous integration on silicon substrates. $In_{0.07}Ga_{0.93}N$ layers were grown on silicon with relaxation levels over 65%. Micro-LEDs grown and fabricated on top of the relaxed porous GaN templates had a 20 nm wavelength red shift in the porous devices, but with low emission power and significant leakage current.

Table of Contents

Acknowledgements: iii
Curriculum Vitae iv
Abstract vii
1. Introduction 1
1.1 Modern LED Applications 1
1.2 GaN Lasers 4
1.3 GaN Laser Applications 4
1.4 Principles of Operation 7
1.5 Key metrics of LEDs and lasers 10
1.5.1 Efficiency definitions 11
1.5.2 Methods to calculate laser gain and loss 14
1.6 III-Nitride Material System 17
1.6.1 Metal-Organic Chemical Vapor Deposition 18
1.6.2 GaN Crystal Polarization 22
1.7 The Green Gap 24
2. Porous GaN 26
2.1 Etch Mechanism 28
2.2 Porous GaN etch development 29
2.3 Quantifying pore morphology 33
3. Edge emitting lasers with porous GaN cladding 34
3.1 Laterally confined blue laser details 36
3.1.1 Lateral Confinement by porous GaN 40
3.1.2 Electrical properties 41
3.1.3 Optical properties and lasing characteristics 43
3.1.4 Thermal properties 44
3.2 Increased silicon doping in porous GaN cladding 44
3.3 New design for porous GaN cladding blue lasers 46
3.3.1 Blue laser results 47
3.3.2 Scattering loss due to NP GaN 51
3.4 Fixing etch selectivity 54
3.5 Green LD with porous GaN cladding 56
3.5.1 Green laser design and optimization 56
3.5.2 Green laser fabrication details 58

3.5.3 Green laser results 60
3.6 Porous vs InAlN cladding at longer wavelengths 67
3.7 Conclusions 69
4. Porous GaN Distributed Bragg Reflectors 71
4.1 DBR Fabrication 72
4.2 GaN VCSEL development 75
4.3 Details of VCSEL Fabrication 77
4.4 Results of VCSEL batch 80
4.5 Conclusions and future work 85
5. Mechanically relaxed templates via porous GaN on silicon substrates 86
5.1 Development of relaxed InGaN on silicon substrates 87
5.1.1 Relaxed InGaN tiles 88
5.1.2 Wavelength shifted MQWs 93
5.2 µLED Fabrication 96
5.3 Strain relaxed template conclusions 100
6. Conclusions, Outlook, and References 100
6.1 Other potential porous GaN devices 100
6.2 Conclusions and Future Directions 103
6.3 References 106

1. Introduction

While countless books, articles, journals, and conferences have documented the influence of the blue LED, it is difficult to overstate the impact that it has had on the world. GaN LEDs create light with a quarter of the energy of incandescent emission and lasts 25 times longer to failure. The US Department of Energy reports that LED lighting saved US consumers 1.3 quadrillion Btu of energy in 2018, $14.7 billion [1]. This was more than the energy generated by every solar and wind plant combined [2], and with only 30% of lighting installations converted to LED. Imagine full LED adoption and it is easy to see how they are not just a market success, but a positive technological force.

While the conversation about energy appropriately focuses on shifting to renewable sources, it should not be forgotten that reducing consumption is an equally noble accomplishment. When our planet is carbon neutral, and humanity looks back on the difficult problems it solved to prevent catastrophe from global climate change, it can argue that GaN LEDs were a major part of the solution.

1.1 Modern LED Applications

Blue LEDs are used with fluorescent phosphors to make white light. While these were first put into the market in the 1990's, many years were needed to exhibit cheap, high-volume production of consumer bulbs. This involved developing not just the LED emitter, but also the phosphor coatings, packaging, and factories. The last 20 years have

resulted in mature LEDs breaking into all aspects of general lighting, inexorably moving towards full adoption.

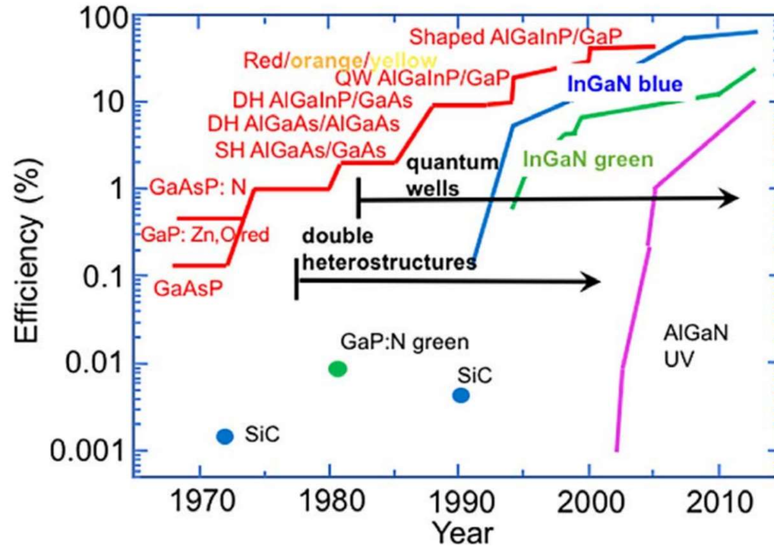

Fig 1-1: Reported LED efficiency by year noting major technological advancements in many semi-conductor material systems [3]

GaN LEDs next big market is in consumer displays. Blue, green, and red LEDs are combined to make pixels emitting across the full visible spectrum. As display products have become smaller needing higher resolution, LEDs have followed suit. Ultra-small LEDs with dimensions in the tens of micrometers have been termed microLEDs, or µLEDs. In comparison with liquid crystal displays, µLEDs can offer better display contrast, response times, and efficiency, as well as flexibility and transparency. These advantages have led to µLED to be a key technology for large displays, phones, watches, as well as nascent near-eye display technologies of virtual/augmented/mixed reality glasses.

Many of the biggest technology companies (hardware and software) have programs developing µLEDs in displays, including Apple, Google, and Meta. In May of 2022, Google acquired µLED startup Raxium in a >$1 billion sale [4]. In 2021, Facebook formally changed the company brand to Meta based on the planned Metaverse - a virtual reality universal space centered around µLED displays currently under development [5]. The massive volume of consumer products planning to use µLEDs has driven market predictions over $11 billion by 2026 [6].

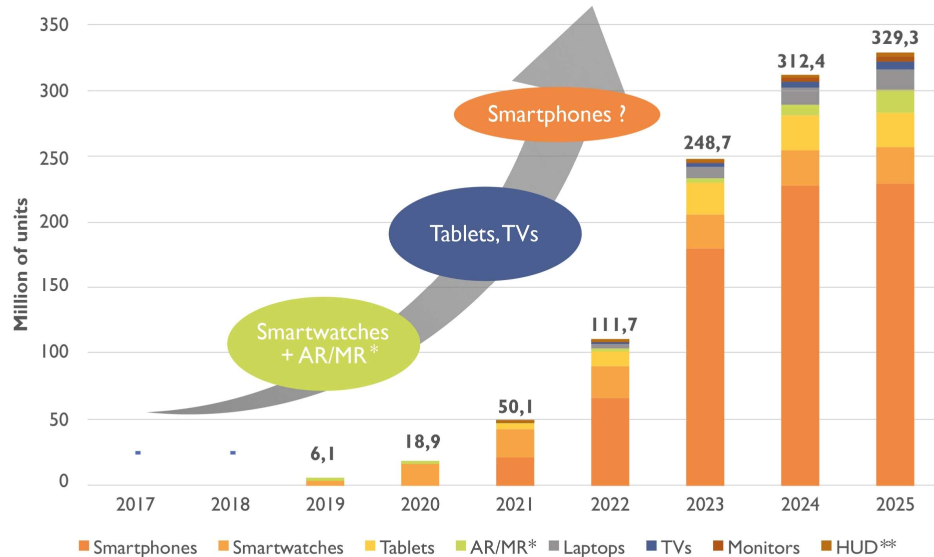

Fig1-2: µLED display volume forecast [7]

A lesser-known application for GaN LEDs is visible light communication (VLC) in light fidelity (LiFi) [8]. Real estate in radio bandwidths is running out and will only get more crowded. Visible wavelength communication based on LED modulation would open capacity to near limitless levels and could allow faster and broader freedom for data transmission. It is free of electromagnetic interference and is more secure because of line-

of-sight transmission. Finally, it provides the two-for-one task of illumination, a nice feature for an efficient world.

1.2 GaN Lasers

Laser diodes (LDs) are one rung higher on the evolutionary ladder of GaN emitters. With a few structural changes and very high drive currents, GaN LEDs turn from omnidirectional light emission to a narrow wavelength, focused beam. These simple changes offer countless applications that LED is unable to occupy.

1.3 GaN Laser Applications

The earliest GaN lasers, dim and inefficient, were used in the transient Blu-Ray technology. As GaN lasers developed higher efficiency blue emission over the last decade, they have entered the market in high brightness lighting applications. The fundamental principle of stimulated emission allows lasers to operate with high efficiency at large current densities with much less wafer area and highly directional light output. This has found a fitting application in vehicle headlights, where companies like Kyocera SLD Laser have pioneered high brightness laser lighting. Coupled with adaptive beam forming technology, which has officially been legalized in the United States in February of 2022 [9], laser headlights allow increased visibility up to 1 km distance while avoiding glare seen by other drivers.

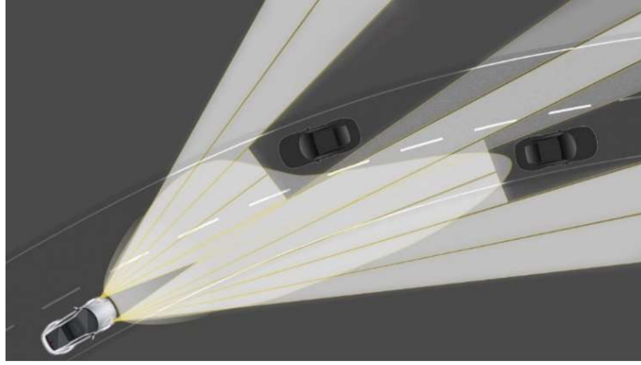

Figure 1-3: Adaptive beam forming technology has been legal in other parts of the world for several years but was only recently legalized for auto manufacturers in the United States.

GaN lasers are similarly competing with LEDs for near eye display applications. Visible wavelength lasers pair with micro-electromechanical systems (MEMS) to rapidly scan over a reflective screen. The beams are modulated to project pixels forming an image. The high brightness offered by GaN based lasers allow usability in any environment, even bright sunlight. Laser displays also have free-focus projection – the image is always in focus regardless of the presence of contacts or the ability of the user's eyes.

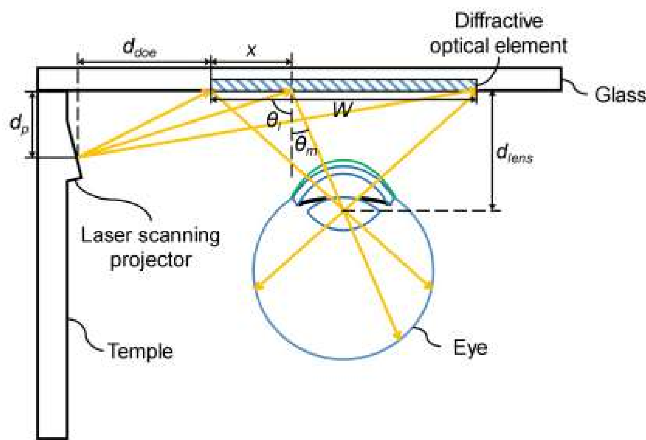

Figure 1-4: Design of a near-eye laser scanning display for augmented reality applications [10]

A unique feature enabled only by laser in near-eye display is eye tracking [11]. Lasers can be used to scan the cornea and determine the position and orientation of the eye. These measurements allow high speed tracking and predictions for where the eye is moving next. The display can then graphically render only the area where the eye is focused while leaving the peripheral at low resolution, allowing cheaper and more efficient displays.

While LEDs are near ubiquitous in lighting applications and are available as a rapid source for dual lighting/data transmission, lasers have the potential for performance advantages. Lasers have an order of magnitude higher switching speed, limited by the photon lifetime instead of carrier lifetime (as in LEDs), leading to significantly more bandwidth. They are also brighter and highly directional, increasing the range for information transmission.

There are many uses for GaN lasers beyond the capabilities of LEDs. Several applications in industrial, defense, and scientific markets require a narrow, coherent emission. For example, laser cooling can be used to bring atoms near absolute zero temperature, where fundamental quantum mechanical principles can be investigated. The laser wavelength must be finely tuned to match specific electronic transitions in the particular atom studied – for example, strontium has a transition at 461 nm, a blue wavelength ideal for GaN based emitters. While diode pumped solid state lasers (DPSLs) might also be used to create visible wavelength beams, direct emission sources avoid the efficiency loss from frequency doubling in DPSLs and are typically much simpler to fabricate.

1.4 Principles of Operation

The simplest description of an LED is a semiconductor junction consisting of a n-type region that is rich in electrons and a p-type region that is starved of electrons (rich in electron "holes") sandwiched by an intrinsic region. When an electrical bias is applied across the junction, holes along the valence energy band are injected into the active region and ideally recombine with electrons along the conduction band to emit a photon of light. The energy bandgap of the material in the intrinsic region determines the wavelength of the emitted photon, and the direction of emitted light is random. There are undesirable ways for the electron and hole to recombine that don't result in a photon emission. The first is by Shockley-Read-Hall, where a trap energy state in the middle of the band can lead to phonon or long-wavelength emission. The other mechanism is Auger recombination, where instead of emitting a photon, a second electron is elevated to an even higher energy level. This hot electron typically overshoots the quantum wells, avoiding useful photon emission.

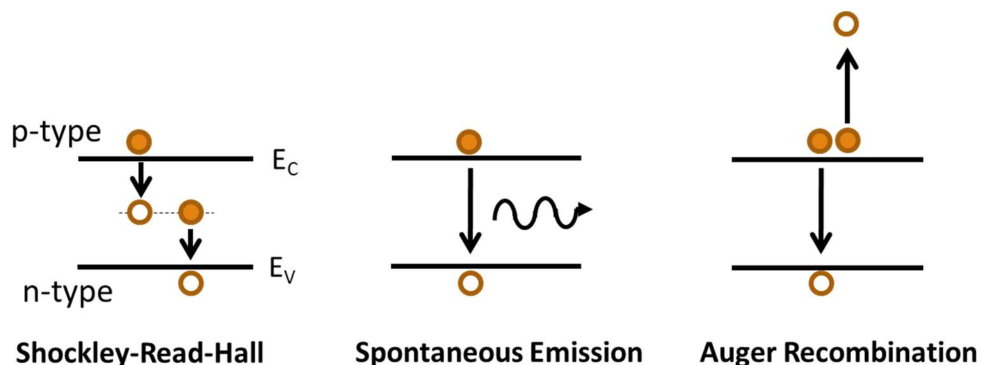

Figure 1-5: Primary recombination mechanisms in LED active region

To mitigate unwanted recombination pathways, modern LEDs use a double heterostructure. This means that the intrinsic region is made of material with a lower bandgap, creating a quantum well (QW) confining charge-carriers. Often multiple quantum wells (MQW) are used for better confinement resulting in higher efficiency. Material with a larger bandgap can also be used to block carriers. AlGaN alloys are used to block electron overshoot into the p-region in GaN based LEDs.

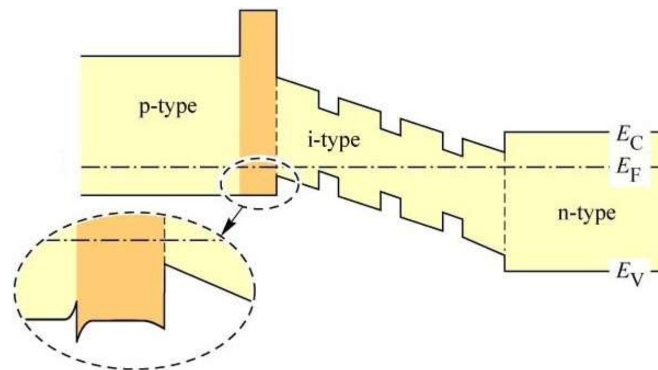

Figure 1-6: Band diagram for typical LED [12]

Lasers are based on the stimulated emission process. This occurs when photons interact with electron-hole pairs, emitting another photon in the same frequency, polarization, and direction as the first. Stimulated emission is maximized by designing a device that optically confines the photons with the charge carriers. Edge emitting laser diodes (EELDs) use cladding layers around the basic p-i-n structure that have a lower refractive index. Whereas LEDs are typically fabricated into squares for omnidirectional light output, EELDs are made into bars with reflective facets. Under operation, light is generated and guided by the cladding layers to the facet mirrors, creating feedback and

total internal reflection. As the trapped photons resonate within the cavity, forming optical modes, they interact with other electron-hole pairs. Incident photons result in stimulated emission, emitting another photon exactly in phase with the first. As the bias is increased, the number of electrons in excited states begins to exceed those at the ground state, forming a population inversion. The carrier density subsequently locks. This is where stimulated emission becomes the dominant recombination mechanism, and there is net optical amplification and gain. The result is a coherent laser beam emission out of each facet.

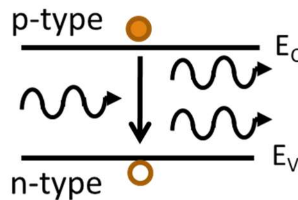

Figure 1-7: Stimulated emission in Laser active region

Another type of laser is a vertical cavity surface emitting laser (VCSEL). This device is designed to emit normal to the material surface instead of out a side facet. Instead of low index cladding, highly reflective mirrors sandwich the p-i-n diode, and the cavity mode vertically interacts with the gain medium. There are several advantages to vertical cavity emitters, but state-of-the-art GaN based VCSELs require difficult, high complexity growth and fabrication processes. Very few research groups have achieved working GaN VCSELs and improving GaN VCSEL performance is an active area of research.

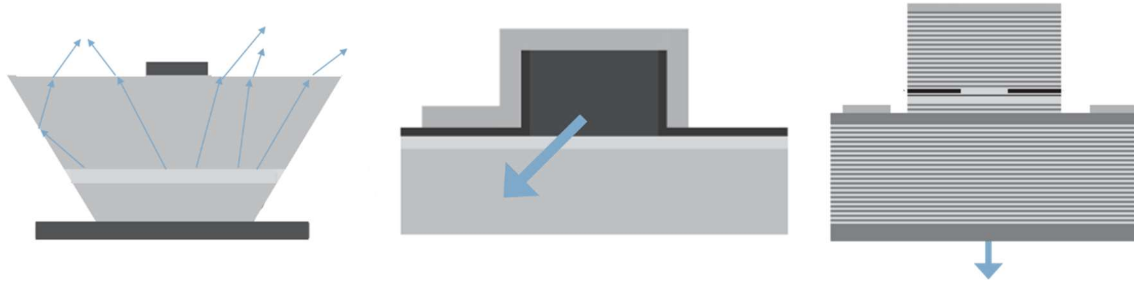

Figure 1-8: Typical two-dimensional device geometries for LEDs (left), EELDs (middle), and VCSELS (right). The blue arrow indicates the emission direction

1.5 Key metrics of LEDs and lasers

There are several important metrics to characterizing LEDs and laser diodes, and the application drives what defines a good device. Light output power, voltage, and efficiency are always key considerations. The turn-on voltage is when the first photons are emitted, and the series resistance across the junction can be found from the slope of the IV line after turn-on.

In a laser, the point at which stimulated emission overtakes spontaneous emission is called the threshold. This is where the gain of the laser is equal to the loss in a round trip of the laser cavity. As current is increased, the gain increases leading to high output powers. It is often beneficial to have low laser threshold and higher dP/dI to maximize the power, so that slope is characterized as the slope efficiency. Equations describing the current, carrier density, gain, threshold, power, and slope efficiency are outlined in chapter 2 of [13].

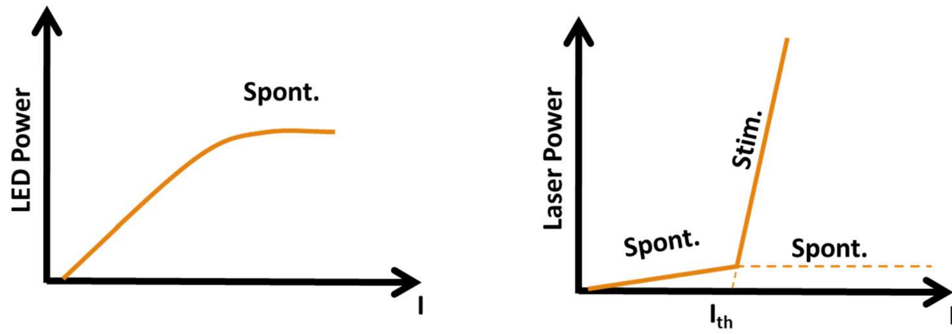

Figure 1-9: Representations of LED and laser power curves with increasing currents

While the wavelength of light emitted by an LED is determined by the bandgap, there is a range of energy states that the charge carriers occupy near the conduction and valence bands resulting in a wide spread of wavelength emission. This thermal broadening is on the order of full width at half maximum (FWHM) equal to about 20 nm for a blue emitting device. Since lasers take advantage of stimulated emission with coherent emission, linewidths are much narrower, on the order of 2 nm. In a VCSEL, the short cavity determines the wavelength and can achieve single mode linewidths lower than edge emitters down to 0.1 nm.

1.5.1 Efficiency definitions

The most general measurement for efficiency of a GaN emitter is the wall plug efficiency (WPE), also known as power conversion efficiency (PCE), representing the ratio of power emitted as light over the electrical power put in. It is useful to break this into components to understand the advantages of different devices and designs. Measuring the

emitter power as a function of current allows pulling out the external quantum efficiency (EQE) with:

$$P = \eta_{EQE}\frac{h\nu}{q}I \qquad \text{eqn 1-1}$$

where P is the measured emission power, hν is the photon energy, q is the charge of an electron, I is the current, and η_{EQE} is the EQE. For an LED, η_{EQE} is further split into the extraction efficiency (η_{ext}) and the internal quantum efficiency (η_{IQE}):

$$\eta_{EQE} = \eta_{ext}\eta_{IQE} \qquad \text{eqn 1-2}$$

The extraction efficiency accounts for the reabsorption of photons and is affected largely by the device geometry not allowing photons to escape the chip. The IQE is then the useful photon recombination rate over all possible recombination rates, described by the "ABC" model in LEDs. These are essentially three parameters fitting to the one, two, and three body recombination mechanics of SRH, spontaneous emission, and Auger recombination, respectively:

$$\eta_{IQE} = \frac{BN^2}{AN + BN^2 + CN^3} \qquad \text{eqn 1-3}$$

where N is the carrier concentration. Efficiency peaks early and falls at high current densities. Since Auger recombination is a three-carrier recombination mechanism, the rate is proportional to the third power and begins to dominate at the high current densities resulting in droop [14].

In a laser, the carrier concentration clamps at threshold, and Auger recombination is less of a problem. Though state-of-the-art GaN lasers have a lower peak PCE than LEDs,

they maximize at a much higher current density. This higher current density allows higher power densities and less chip area for useful applications. Since lasers are also highly directional, there are many applications that require another efficiency parameter measuring useful delivered light, where lasers could hold an advantage over LEDs with clever packaging and module design.

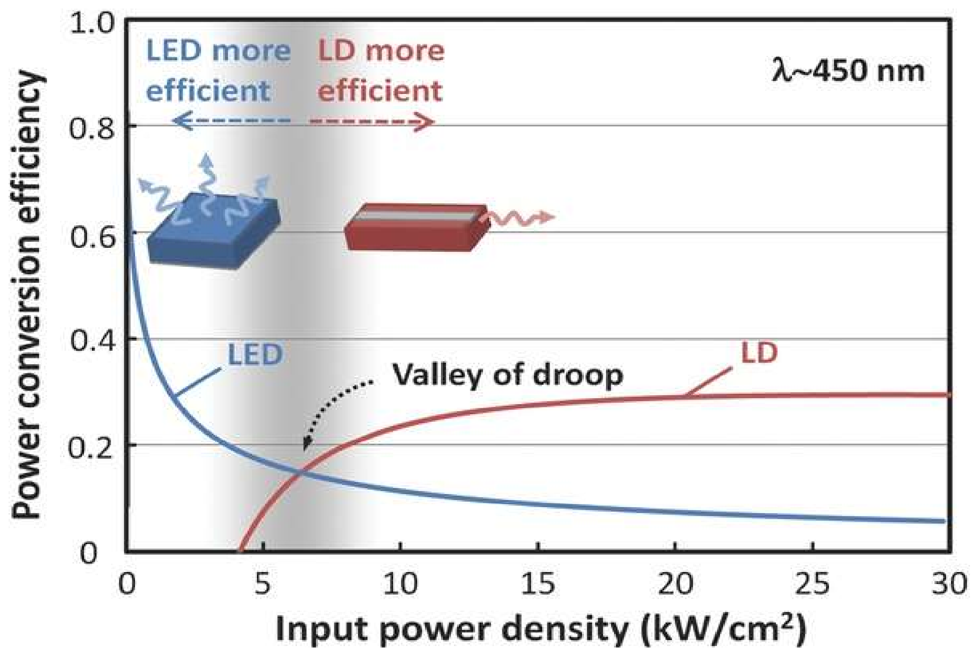

Figure 1-10: LED vs Laser Wall Plug Efficiency [15]

The low PCE of GaN lasers ultimately results in heat generation at high current densities. Rising operating temperature generally increases the current density needed to reach a particular gain. The high energy spread of carriers broadens the broadening of the gain function. There is also carrier leakage due to hot carrier overshoot, and several other parameters that result in lower operating efficiency at high temperatures [13]. To avoid

additional fabrication complexity involved with heatsinking, research grade laser diode characteristics are often measured under pulsed electrical injection before attempting continuous-wave operation. Pulsed electrical injection generates significantly less heating than DC.

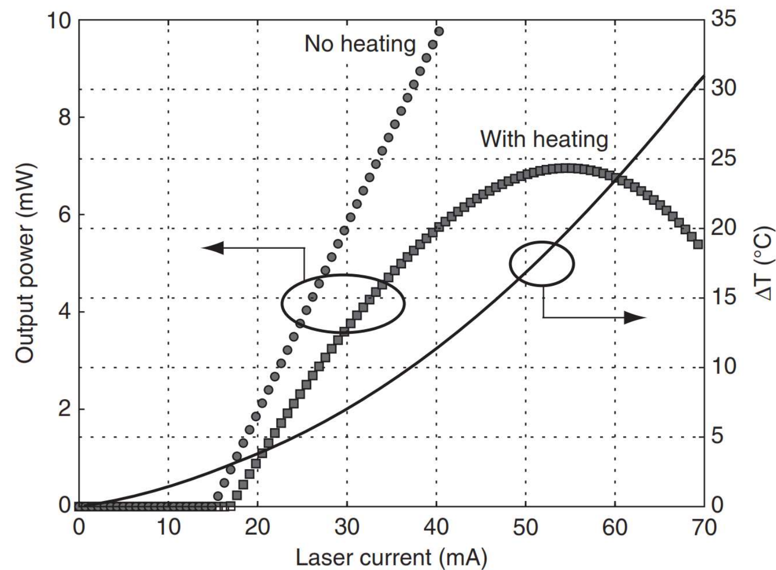

Figure 1-11: Comparison of laser diode power with and without self-heating [13]

1.5.2 Methods to calculate laser gain and loss

Understanding the optical gain and sources of loss in a laser are critical to development. There are several indirect ways to measure these values with single devices or batches of fabricated bars and test structures, a few of which we will discuss in this section.

Variable stripe Length

A common technique called the variable-stripe length method uses a series of fabricated devices with different cavity lengths. This is applied to edge emitting structures but can also be used to estimate the material gain of an active region used in a VCSEL (if the same material is used to make edge emitting devices). Plotting the inverse of the differential efficiency against the device length allows you to fit a line to estimate the injection efficiency and internal loss with:

$$\frac{1}{\eta_d} = \frac{<\alpha_i>}{\eta_i ln(1/R)} L + \frac{1}{\eta_i} \quad \text{eqn 1-4}$$

where η_d is the differential efficiency, $<\alpha_i>$ is known as the internal loss, η_i is the injection efficiency, R is the estimated mirror reflectivity, and L is the varying cavity lengths. Since the mirror reflectance is already estimated and we know the cavity lengths, we can get an estimate for α_m and find the threshold modal gain by summing the losses:

$$\Gamma g_{th} = <\alpha_i> + \alpha_m \quad \text{eqn 1-5}$$

where g_{th} is the material gain and Γ is the optical confinement factor. The confinement factor is found by solving for the optical field position in the laser structure and integrating over the active material. This paired with the measured threshold current densities can be plotted and logarithmically fit with:

$$g = g_{0n} ln\left(\frac{J}{J_{tr}}\right) \quad \text{eqn 1-6}$$

where J_{tr} is the transparency current density and g_{0n} is a relative gain factor that can be compared across lasers.

Segmented contacts

Outlined in detail by Blood [16], using a single laser bar divided into segments can allow estimations for the gain and internal loss. The bar must have an angled front facet and back facet far from the measured contacts to prevent reflections and lasing. This method again works only for an edge emitting type design. First, both front and back segments are probed at the same current density and the light is collected from the angled facet by a single mode fiber and spectrometer. Then, only the front segment is probed and measured (looking at the same optical mode). Although multiple spatial modes can propagate in the wide ridge, care must be taken to collect only light propagating in the waveguide using small numerical aperture lenses and a single mode fiber to filter spontaneous emission and scattered light. The two measurements can be related by this equation:

$$(\Gamma g_{th} - <\alpha_i>) = \frac{1}{L} ln(\frac{I_{both}}{I_{front}} - 1) \qquad \text{eqn 1-7}$$

where I is the measured intensity and the subscripts delineate which segments were probed, and are functions of wavelength. Absorption curves can then be generated by measuring intensity from only the back segment and related with:

$$(A - <\alpha_i>) = \frac{1}{L} ln(\frac{I_{front}}{I_{back}}) \qquad \text{eqn 1-8}$$

The absorption curve can then be plotted against wavelength and is asymptotic to the internal loss at long wavelengths. Once the internal loss is found, it can be added to eqn 4 and the gain curve is found. The peak gain at several current densities can then be plotted up and eqn 3 can be used again to find the gain factor and transparency current density.

Hakki-Paoli

This method can produce the gain spectrum by measuring intensity of the Fabry-Perot modes below threshold [17]. For visible wavelength lasers, the resolution of the spectrometer must be very high to measure the complete maxima and minima of the fringes. First, the depth of modulation is calculated between consecutive peaks by averaging the peak maxima and dividing by the valley in between:

$$\gamma_i = \frac{P_i + P_{i+1}}{2V_i} \quad \text{eqn 1-9}$$

The gain can be estimated at each point using:

$$\Gamma G_i = \frac{1}{L} ln\left(\frac{\gamma_i^{1/2}+1}{\gamma_i^{1/2}-1}\right) + \frac{1}{L} ln(R) \quad \text{eqn 1-10}$$

This can similarly be used for various current densities and plotted up with eqn 3, though it is limited to measurements below the lasing threshold.

1.6 III-Nitride Material System

Group III materials aluminum, indium, and gallium paired with nitrogen are generally referred to as wide-bandgap semiconductors. The various alloys of $(Al, In, Ga)_xN_y$ are capable of spanning emission wavelengths from UV to IR across the entire visible spectrum, making them exploitable for all the already mentioned applications. There are several considerations that prevent that in practice, which will be discussed at length in the next few sections.

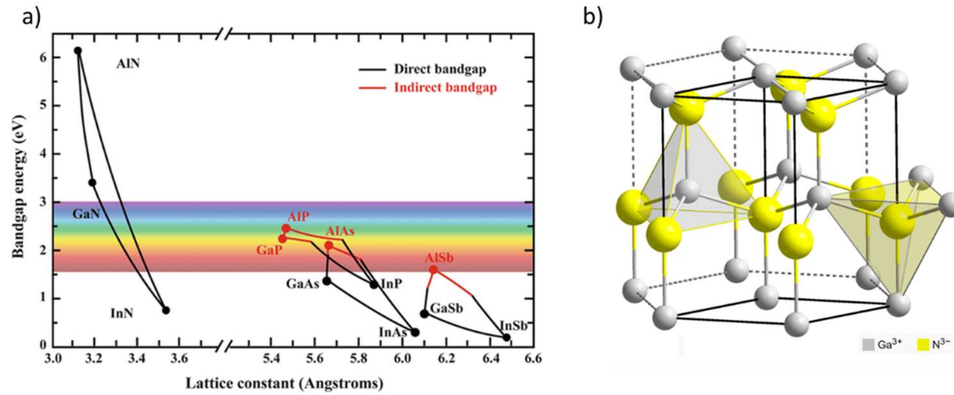

Figure 1-12: a) Bandgaps against lattice constants for common semiconductor materials [18] and b) Wurtzite crystal structure of III-Nitride [19]

While III-Nitride crystals form a wurtzite lattice, the atomic bond lengths vary greatly between AlN, GaN, and InN. The lattice mismatch between the different binary alloys induces significant strain when the disparate materials are incorporated into one structure. This limits the achievable growth compositions and is a topic of continuous development.

1.6.1 Metal-Organic Chemical Vapor Deposition

Several methods exist to grow III-Nitride materials, but the current method of choice for manufacturing GaN LEDs and lasers is Metal-Organic Chemical Vapor Deposition (MOCVD) due to its ability for high-volume production and stellar growth quality of crystalline material. This technique involves injecting highly volatile metal-organic precursor gases into a heated chamber. The reactants are pyrolyzed into constituent components and absorbed onto a substrate crystal.

Substrate and Reactants

Choice of substrate depends on the application. LEDs are least susceptible to defects and have been heterogeneously grown on silicon, silicon carbide, and sapphire using some sort of buffer. Threading dislocations are commonly around $1x10^8$ cm^{-3} or higher for these types of growths. Sapphire is almost uniformly the LED substrate of choice due to its high availability and low cost. Since lasers operate at much higher current densities and have optical constraints, they are extremely prone to failure from defects. Lasers require fewer defects (~$1x10^6$ cm^{-3}) for high reliability and need to be grown either homogeneously on bulk GaN substrates or with advanced growth techniques such as epitaxial lateral overgrowth (ELOG).

Metal-organic precursors are useful for crystal growth because of their high volatility. They are picked up by the push gases of either N_2 or H_2, and ammonia (NH_3) is used as the source of nitrogen. Trimethyl Gallium (TMG) and Triethyl Gallium (TEG) are the common sources for gallium. TEG is more expensive but allows higher quality layers due to lower carbon incorporation. Carbon is an n-type impurity and gets trapped in the lattice due to incomplete decomposition of the methyl groups on the surface of the growing layer. The ethyl groups in TEG are more stable after decomposing due to β-elimination, and thus are more easily removed from the reaction surface and have less incorporation into the crystal [20]. Keeping carbon from incorporating into the active region is critical for high quality material growth. Trimethyl Indium (TMI) and Trimethyl Aluminum (TMA) are used for the indium and aluminum sources, respectively. Disilane (Si_2H_6) is used as a silicon

dopant source for n-type material, and Bis(cyclopentadienyl)magnesium (Cp_2Mg) is used for the p-type dopant.

The p-side is doped with Mg and is almost always grown last for a few reasons. Doping GaN p-type requires annealing to remove hydrogen passivation [21], and the hydrogen needs open area to diffuse from the crystal. Mg also tends to stick to the chamber sidewalls [22], leading to a memory effect where Mg can incorporate into the structure later than intended. This can be bad for layer definition and future growths.

System Design

Several types of reactors have been developed over the years to improve crystal growth quality. In all cases, alkyls are picked up through bubblers, carried into a top flange, and injected into a heated chamber over a substrate. The growth conditions can vary wildly. Veeco dominated the reactor market for several years making a closed-coupled showerhead design, where the gases are uniformly spread over high rpm platter with a large area. The reactor height is very short so that the boundary layer stays uniform over the substrate. AIXTRON now leads industrial reactor sales with 75% market share using a planetary rotation design [23]. Wafers are held by a rotating platter, but also rotating within pocket for very high uniformity conditions.

The LED and laser material in this thesis were all grown using Professor Shuji Nakamura's special two-flow reactor design [24]. This design enables uniform growth entirely at atmospheric pressure.

Flow Conditions

Many factors need to be considered when growing LED and laser material. Faster growth rates are generally desired for short recipe times but need to be balanced with crystal quality. The active region is the recombination center and needs very high crystal quality and are grown slower than other layers in the stack using TEG. Indium incorporation is extremely temperature dependent; even minor run-to-run variations affect wavelength targeting in several ways. This means for visible wavelength emission the active region needs to be grown cold to incorporate proper indium levels. Crystal morphology is also highly dependent on the temperature, so each layer composition needs to be carefully optimized for the ideal growth temperature.

Several dimensionless numbers for mass and heat transport need to be considered to realize desired fluid flow in the reactor chamber. Laminar flow is necessary to achieve a flat boundary layer and thus uniform crystal growth across the wafer, so the Reynold's number for each process condition needs to be under 2300. The Rayleigh number describes whether the flow is in the conductive heat transfer regime. It needs to stay under 1700 or else heat transfer will be dominated by convection, leading to non-uniform heating. Finally, the Grashof number over the square of the Reynolds number needs to be less than 0.3 to ensure forced convection as the dominant force over free convection in the chamber. It is important to calculate the transport parameters for both push gas flows considering the large differences in density and thermal conductivity for H_2 and N_2. There are other growth quality considerations when choosing carrier gas. Hydrogen naturally etches the GaN surface due to higher desorption rates of nitrogen in the crystal [25]. This

however can lead to better layer growth quality, such as preventing V-defect formation [26]. Hydrogen should also be used for the magnesium containing layers. Studies have been performed by Van De Walle et al using Density Functional Theory, finding that Mg-H complexes have lower formation energies in the GaN crystal than the native defect of nitrogen vacancies. The same study showed that Mg doping is higher when compensated with a hydrogen atom, meaning higher miscibility in the GaN crystal [27]. These are both beneficial to Mg doping in a GaN crystal layer. Other studies suggest that that Mg:GaN grown with nitrogen push gas has better Mg incorporation, but a hydrogen push gas has better Mg activation as well as well as better structural quality than the same layers grown using nitrogen [28].

More recent investigations, however, have had conflicting results. It has been found that using nitrogen as a push gas for the upper pGaN layers can give lead to improved surface morphology following growth [29]. Some also report growing full LED structures with only nitrogen push gas can perform better under electroluminescence than an LED using hydrogen for p-type GaN [30]. Alternate growth temperatures were needed for each push gas, but nevertheless an interesting result. These show that even selection of carrier gas is an active area of research.

1.6.2 GaN Crystal Polarization

The wurtzite crystal structure of GaN has an inherent polarization field. This has far-reaching consequences when it comes to GaN optoelectronic device properties. The *c*-plane internal polarization field significantly bends the quantum well energy bands. This

shifts the electron and hole wavefunctions to opposite sides of the well, reducing overlap and quantum efficiency. This is known as the quantum confined Stark effect (QCSE), and it is deleterious to all III-Nitride emitters. Laser diodes are particularly impaired by this separation of charge: at high current densities, coulomb screening of the electric field causes a large blue shift in the emission wavelength – this in turn requires higher indium content to reach longer wavelengths, making charge separation even worse [21]. This has led to research interest in non-polar and semi-polar GaN planes as substrates.

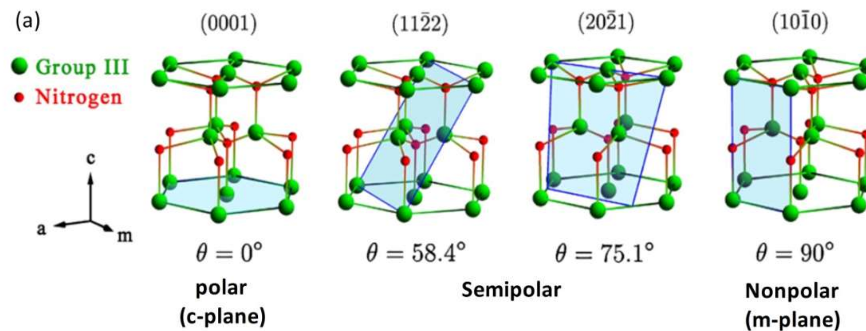

Figure 1-13: Varied semi-polar planes of GaN [31]

Non-polar and semi-polar GaN planes have crystal symmetry reducing or eliminating the internal piezoelectric fields. This has several benefits. It allows bands to flatten during operation, improving electron and hole wavefunction overlap and radiative efficiency. Quantum wells can be grown with wider widths, which allows a lower carrier density for a particular current injection. As the bias is increased the band-bending is less severe, resulting in lower wavelength shifts at higher current density. This has a dual

benefit for GaN lasers, not only relieving the negative effects of QCSE, but improving the material gain.

Growth mechanisms across the various GaN planes are different and lead to a slew of varied growth failures. Basal plane growths, especially on heterogeneous substrates, result in threading dislocations and V-shaped pits, which are currently under research for their good qualities for longer wavelength LEDs [32]. V-pits are absent on GaN semi-polar planes but growing beyond the critical thickness for lattice mismatched layers like AlGaN or InGaN results in growth defects such as misfit dislocations [32]. For these reasons, LEDs are generally grown on *c*-plane while lasers have had more success with semi-polar substrates, such as those grown by Kyocera SLD Laser.

1.7 The Green Gap

While III-Nitride emitters span UV to IR, in practice they are very good at blue, peaking around 420 nm but dropping off elsewhere. The issues associated with UV are largely outside the scope of this thesis, which will focus mostly on the problems with green, yellow, and red emission, discussed from this point on as “long-wavelength” LEDs relative to peak performance. There are several problems associated with long wavelength GaN emitters that are well known, and some that are not. Achieving high efficiency long wavelength emission in the III-Nitride material system has been an active area of research for decades, and there is still work being done to accomplish that goal.

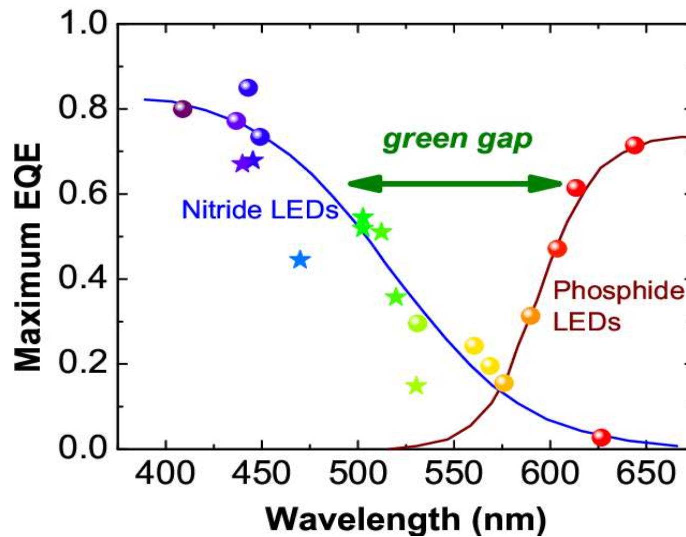

Fig 1-14: Peak external quantum efficiency of reported LEDs as of 2016 [34]

QCSE decreases radiative efficiency due to lower electron/hole wavefunction overlap [35]. This effect strengthens at longer wavelength emission when there is higher indium content and deeper wells. Another well-known problem is the lattice mismatch between InGaN and GaN. Compressive strain is introduced into the crystal when high indium content alloys are grown with GaN buffer layers. The accompanied strain must relax when indium alloys are grown beyond a critical thickness. This manifests in different mechanisms depending on the GaN growth plane used, but a few examples are V-pits on *c*-plane, misfit dislocations on semi-polar planes, or even indium segregation [36]. Another difficulty is the growth temperature. Indium containing layers require relatively colder temperatures to incorporate and need even colder temperatures for higher indium content. Temperature plays a key role in growth quality, and colder temperatures allows contaminants to incorporate into the lattice. Growing hotter after a InGaN layer can lead to

diffusion of the lower layers [37], and so thermal management of the MOCVD growth parameters is important

GaN lasers are hindered even more by these effects. There are few reports of GaN EELDs past 550 nm [38-39], whereas the longest VCSEL is at 560 nm [40]. The first issue is that material gain is simply lower for higher indium content layers. The momentum matrix elements calculated in Table 4.1 of [13] show indium contents required for green emission to be about a third of blue emission quantum wells, and this has been corroborated by experimental measurements [41]. Additionally, the higher current densities required by GaN lasers mean they suffer from an even larger wavelength blue-shift at operation due to the QCSE. This means the indium content must be increased even further. This then leads to problems with growth temperature and strain management. Finally, traditional GaN lasers need cladding layers with high optical refractive index contrast. The lower cladding is generally limited to material that can be grown by MOCVD, and so is usually composed of AlGaN or InGaN alloys that are lattice mismatched, causing further constraints for the active material indium incorporation. While growing on GaN semi-polar planes should increase the material gain relative to *c*-plane and alleviate the QCSE, innovative solutions will need to be researched to solve the efficiency problem at green, yellow, and red in GaN material. This is where research into porous GaN comes in.

2. Porous GaN

Nano-porous GaN (NP-GaN) has become a major research subject over the last few years for its unique optical and mechanical properties in the III-Nitride material system. The

advantages offered by this nascent material have the potential to enable disruptive advances in the increasingly mature industry of visible wavelength LEDs and laser diodes. The work in this dissertation is focused on leveraging NP-GaN to improve performance of several GaN photonic devices.

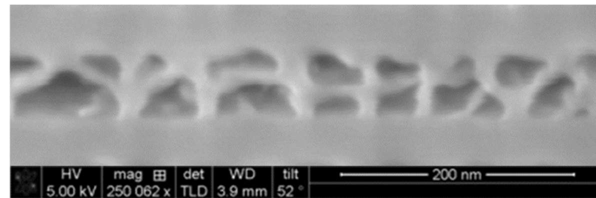

Figure 2-1: Scanning electron micrograph of porous Gan material

NP-GaN has been used for optical properties in lasers. Several groups have made distributed Bragg reflectors (DBRs) in VCSELs [42-43]. Work from UCSB will be discussed fully in chapter 4 of this dissertation. NP-GaN has further been used in edge emitting laser diodes (EELDs) as a waveguide. Chapter 3 in this thesis is about using NP-GaN as a cladding layer in nitride EELDs for blue and green wavelengths.

Early work used NP-GaN's distinct morphology for mechanical advantages. Soh [44] etched a top layer of NP-GaN as a template for growth of high quality GaN buffer layers with fewer misfit dislocations and strain relaxation. Zhang used a NP-GaN template for LED liftoff [45]. An LED stack was grown on a NP-GaN template using MOCVD, simultaneously transforming the NP-GaN into micro-scale pillars. The LED mesas were then bonded to an alternative substrate, where the structurally weak pillars were cleaved for flip-chip processing. Pasayat [46-48] used the porous GaN as a compliant strain relief layer in a

template for growing relaxed µLEDs on sapphire. This dissertation will discuss follow-up experiments attempting to grow relaxed templates using NP-GaN on GaN on silicon substrates in Chapter 5.

2.1 Etch Mechanism

Formed by a wet electrochemical (EC) etch, the mechanism to make NP-GaN is reported in detail by Zhang *et al* [49]. Silicon-doped n-GaN is submerged in acid electrolyte with a platinum wire cathode. As a constant bias is applied, the conductive n-GaN is anodized. Holes are generated at the interface of the semiconductor and electrolyte, the GaN surface is oxidized, the products are dissolved into the electrolyte, and then the products are transported away from the surface. The result is a conductivity selective etch - the most conductive n-type layers are made porous. If an electrically conductive top surface is exposed, the pores nucleate at the top and work downward. If covered by dielectric or non-conductive material, and there are windows to conductive material, the pores will open in the conductive layers and undercut resistive material. This is valuable for enabling useful device architectures.

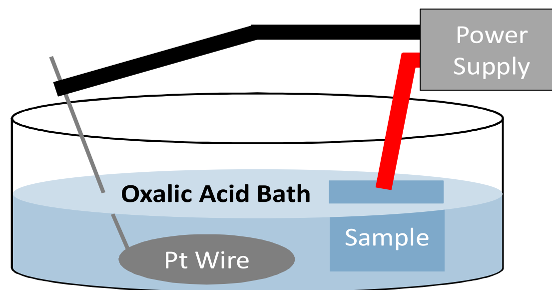

Figure 2-2: schematic of porous GaN electrochemical etch setup

2.2 Porous GaN etch development

The parameters of the electrochemical etch can be manipulated to adjust the properties of the porous material. Varying the layer doping concentration and the applied bias can reach different pore sizes and porosity. Individual etch setups will have different current pathways and resistance, so etch calibrations need to be run to see the unique process window.

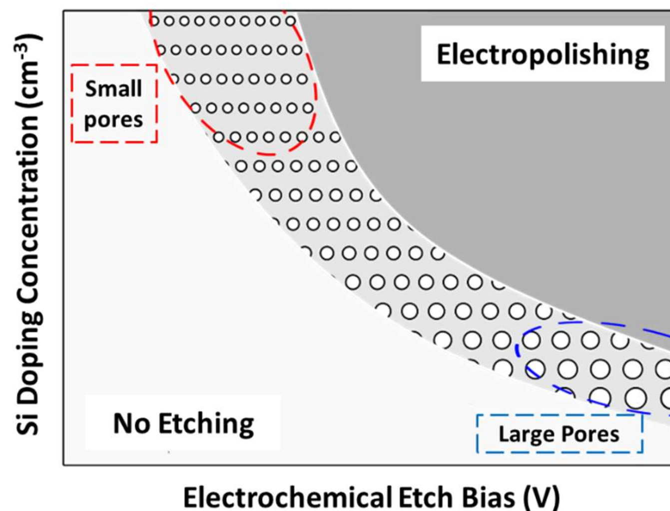

Figure 2-3: Effect of silicon doping and applied bias on porous GaN morphology

The etch can be seen by optical microscope because of the change in average refractive index, hence a change in color. The etch can be stopped, inspected for undercut distance, and restarted, though minor variations in the placement of the sample can cause small changes in the porous material before and after the pause. Sweeping out dissolved Ga products may also lead to varied electrochemistry at the interface. The best way to fully

characterize the morphology is with focused ion beam (FIB) and scanning electron microscopy (SEM). Though pores can be seen on a trench sidewall by SEM, the morphology can often vary greatly from the porous material deeper into the material, so using focused ion beam to characterize the inner NP-GaN is paramount.

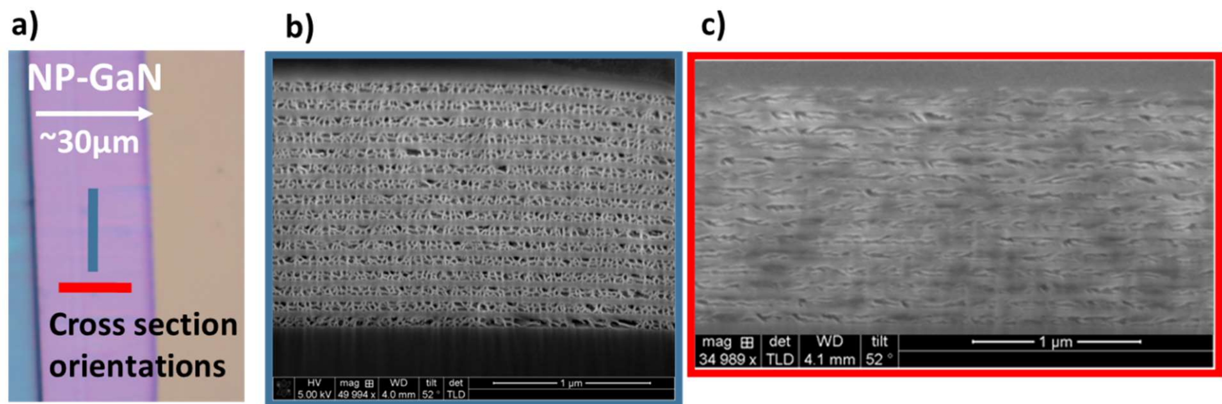

Figure 2-4: a) Optical top-down view of porous GaN DBRs with the porous material proceeding from the trench left-to-right. b) This is an SEM image of the porous GaN with FIB cross section cut perpendicular to the etch direction. c) This is the same sample SEM image of porous material cut parallel with the etch direction. The porous material is pipe-like. In this image, the etch proceeds from the left to the right.

The electrochemical etch setup was comprised of a Keithley power supply connecting the positive lead to conductive tweezers holding the sample in an oxalic acid bath. The etch was found to be more predictable if held by a soldered indium dot to promote contact from the substrate to the tweezers. The negative lead was attached to a platinum wire also submerged in the bath. The surface area and form factor of the wire was intended to be the same across all etches. While stirring the mixture during the etch

did not show an appreciable effect on the porosity, it was found to make etch results more predictable. The mix was stirred sed at approximately 150 rpm to promote dissolution at a of the oxidized GaN material.

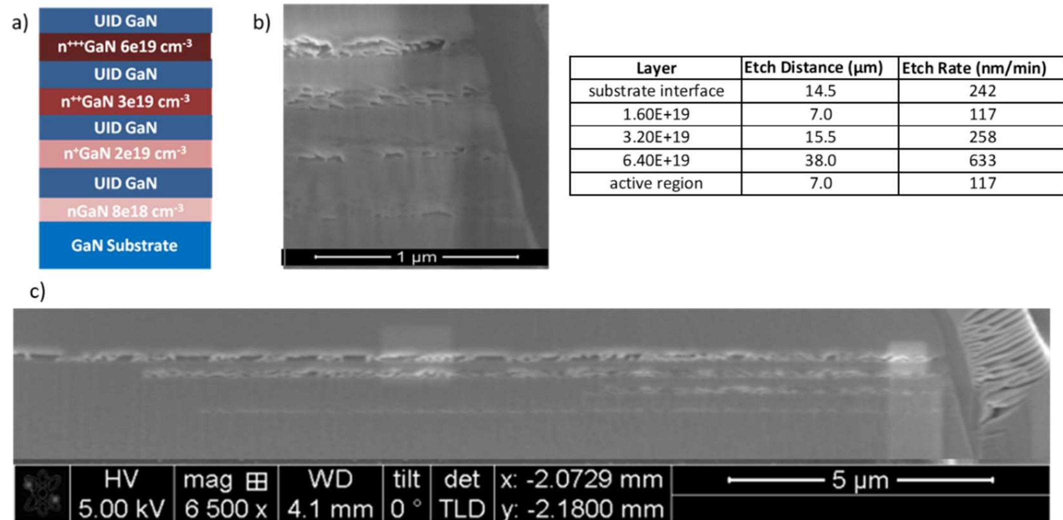

Layer	Etch Distance (μm)	Etch Rate (nm/min)
substrate interface	14.5	242
1.60E+19	7.0	117
3.20E+19	15.5	258
6.40E+19	38.0	633
active region	7.0	117

Figure 2-5: a) epitaxial layer stack grown with varied doping levels and b) SEM of layers electrochemically etched. c) shows the full etch distance to estimate the undercut etch rate. Etch conditions were 4 V for 1 hr

There are many parameters that play a role in the pore morphology. The etch rate also varies with the doping level. The strength of the acid was found to increase the size of the pores and speed of the etch. The oxalic acid was mixed from a dehydrated crystal source, and so etch calibrations are needed after every new variable mixture. While we did not investigate photosensitivity, we covered the etch setup to avoid possible photo-enhancement of the electrochemical etch.

Since the etch relies on conduction pathways through the sample to the tweezers and power supply, the current density through individual layers affects the porosity. That

means larger samples or larger etch volume could decrease the porosity of etched material. Every new structure with different amounts of etched material needs to be calibrated. It also means the amount of sample dipped in solution influences the etch conditions. This is easily seen when measuring the current over time of the etch. As the etch proceeds and the layers become porous, there is less area exposed and the current drops along with a reduction in etch speed.

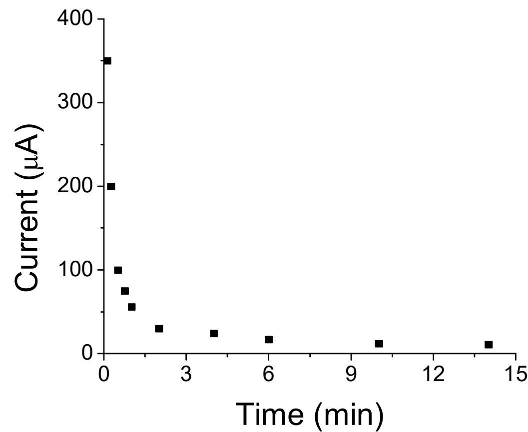

Figure 2-6: Etch current over time

There were small differences in the etch results by GaN plane. The work in this thesis was mainly performed on GaN semi-polar planes. While the c-plane etch was omnidirectional, the semi-polar planes etch rate was slower in the *c*- direction. There was no major difference in the etch rates between 20-21 and 20-2-1.

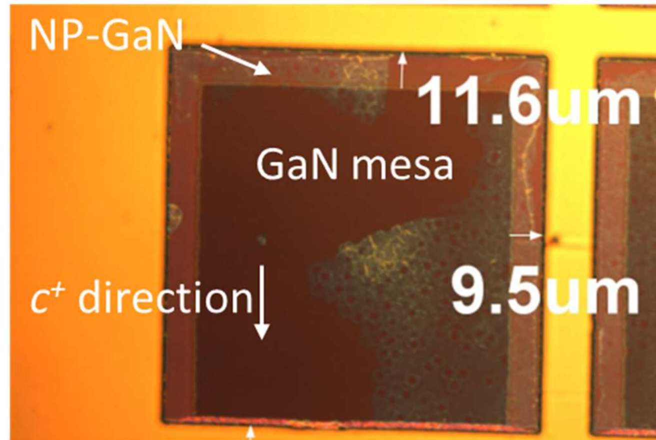

Figure 2-7: Top-down view of a doped GaN mesa after a 5V etch for 30 min on 20-2-1 GaN plane. The lighter colored material is the porous GaN undercutting a SiO_2 hardmask. The c^- direction is a slower rate.

2.3 Quantifying pore morphology

Image analysis is needed to quantify the apparent porosity from an SEM. While a simple image threshold can be done of the 2D cross section, it has high variation resulting from image contrast and brightness. A more consistent method to quantify the porosity can be used with machine learning algorithms such as the open-source software Ilastik [50]. The algorithm is trained by inputting several images and defining porous and non-porous regions. It can then more consistently assess porous regions in future uploads to find statistics on size, density, porosity, and distribution.

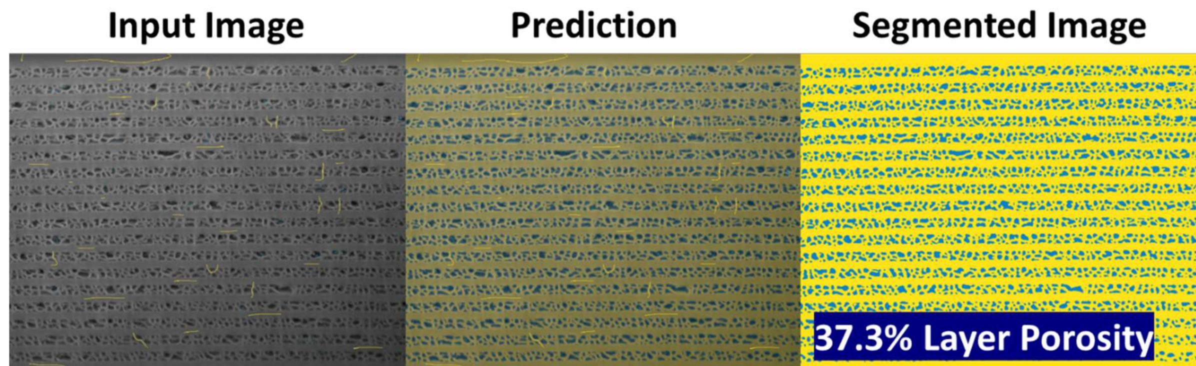

Figure 2-8: FIB cross sectional SEM of porous GaN DBR run through Ilastik. The first Input Image is training, the second is the machine learning algorithm showing where the pores are in the image, and the final segmenting to get the porosity measurement

There are other ways to achieve more accurate measurements for the porosity such as gravimetric analysis or FIB tomography paired with reliable ellipsometric measurements [51]. These could help modeling the index profiles, but for the purposes of this dissertation, the simple image analysis was considered a good enough metric for porosity accounting for the variability in the measurement in our laser device designs.

3. Edge emitting lasers with porous GaN cladding

III-Nitride based EELDs are generally grown on bulk GaN substrates and use some combination of InGaN, GaN and AlGaN to form the active region, waveguide core and cladding layers. While the basal *c*-plane growth orientation is the most common, lasers fabricated on semipolar substrate are expected to have higher gain but have a lower tolerance for thickness and composition of the cladding layers due to early onset of misfit

dislocations. There are several techniques that have been marginally successful, such as intentionally relaxed growth interfaces [52] and limited area epitaxy [53]. The work relevant to this thesis used NP-GaN cladding as an alternative to traditional AlGaN material in an optically pumped EELD [54]. The advantage is the large refractive index offered by porous GaN material while remaining lattice matched, avoiding the introduction of damaging misfit dislocations. Higher index contrast is enabling for laser design to improve mode confinement over the active region.

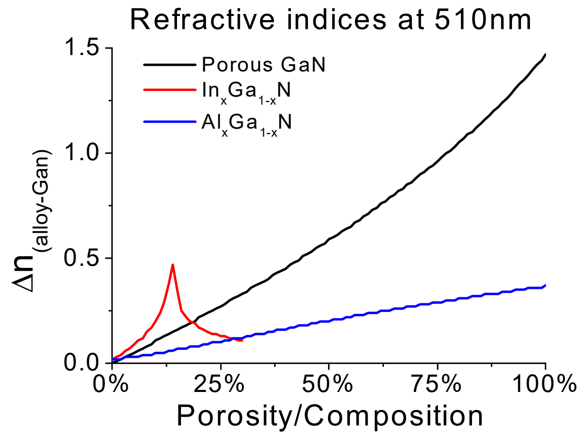

Figure 3-1: Refractive index contrast of porous GaN against competing materials. The data is at 510 nm to highlight the advantages of porous GaN especially at longer wavelengths.

This chapter will discuss work on using porous GaN in electrically injected lasers following the major publications from our research group. The first section is on GaN EELDs with NP-GaN resulting in lateral optical confinement. The proceeding section concerns second batch of blue lasers fixing the porosification front and successfully applying porous GaN as a cladding layer. This includes a discussion on the detrimental effects of scattering

loss in NP-GaN material. The final section is about designing a new batch of NP-GaN clad lasers moving to green emission wavelengths, where the porous GaN exhibits more of an advantage as a cladding material. Gain and loss calculations using the variable stripe and segmented contacts methods will be compared. Finally, designs focused on broadening the applicable wavelength for GaN lasers beyond green into yellow are included. These are comparisons of NP-GaN to InAlN as a potential cladding material as a method to close the green gap.

3.1 Laterally confined blue laser details

Using the lessons learned from electrochemical etch calibrations in Chapter 2, EELD structures were fabricated with NP-GaN material intended to use as a cladding layer. The design was based on internal UCSB blue EELD laser diodes. While the NP-GaN material is expected to benefit from higher refractive index at green wavelengths or longer, blue lasers were targeted first because they are higher gain material and easier to fabricate a device with laser behavior. The epitaxy was grown using an atmospheric pressure MOCVD reactor on the $(20\overline{2}\,\overline{1})$ semipolar plane of a bulk GaN substrate provided by Mitsubishi Chemical Corporation.

The initial n-GaN buffer layer was 400nm thick doped with Si at 8 x 10^{18} cm^{-3}, followed by 800 nm thick of 2 x 10^{18} cm^{-3} Si-doped n-GaN, both at 1180°C. Next was a 65 nm thick $In_{0.06}Ga_{0.94}N$ waveguide doped with Si at 2 x 10^{18} cm^{-3} grown at 965°C, a 20 nm thick unintentionally doped (UID) GaN, and a 2-period multiple quantum well (MQW)

active region with 3 nm thick $In_{0.18}Ga_{0.82}N$ QWs and 7 nm thick GaN barrier layers grown at 890 °C, ending on a barrier. Two quantum wells have been found to be the optimum tradeoff between gain and ability to pump all wells. A 20 nm thick p-$Al_{0.28}Ga_{0.72}N$ electron blocking layer (EBL) was grown at 1000 °C, doped with Mg targeting 3 x 10^{19} cm^{-3}, followed by a 65 nm p-$In_{0.06}Ga_{0.94}N$ waveguide layer, grown at 965 °C with 1 x 10^{19} cm^{-3} of Mg doping. A final 270 nm thick p-GaN layer was grown targeting 2 x 10^{18} cm^{-3} for the first 250 nm and 1 x 10^{20} cm^{-3} for the final 20 nm, grown at 1000 °C.

After a 15 min in an atmosphere furnace at 600 °C to activate the p-type GaN, the sample was taken to the clean room to fabricate devices. Using photolithography and Cl_2 reactive ion etching, a trench was etched 3 µm deep and 30 µm wide with a 300 nm SiO_2 hardmask. This was formed parallel to the surface projection of the *c*-axis so that it would later be positioned 3 µm from the laser ridge, needing this orientation to leverage the higher gain of the semipolar plane. The ultimate laser bars included widths of 2.5 µm and 8 µm, as well as lengths of 900 µm, 1200 µm, 1500 µm, and 1800 µm. A metal contact was evaporated onto the backside of the sample using to use as the anode for the electrochemical etch with composition 1.5 nm of titanium, 50 nm of aluminum, 100 nm of nickel, and 300 nm of gold. Held by conductive tweezers in a 0.3 M oxalic acid bath, an electrochemical etch was performed at 6.5 V for 1.5 hours on the setup discussed in Chapter 2. The forceps must be held above the solution to avoid a short in the circuit, with the result that part of the sample remains unetched and useful as an experimental control to the NP-GaN lasers. After the etch, the porous GaN was found to undercut laterally approximately 17 µm from the trench. The sample was then cleaned with aqua regia at 225

°C and 1:3 HNO_3:HCl for 30 min to strip remaining backside metal, as well as buffered HF to remove the hard mask.

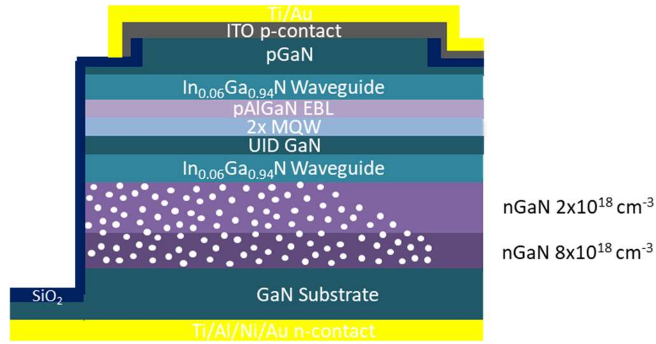

Figure 3-2: Schematic for epitaxial structure. Baseline is non-porosified.

Details for the remaining processing can be found in [55], but involve a self-aligned ridge etch, indium tin oxide (ITO) deposition for the p-side contact and cladding, p-side metal deposition, facet formation with chemically assisted ion beam etching (CAIBE), and backside metal deposition. The resulting structure is shown above in Fig 3-2.

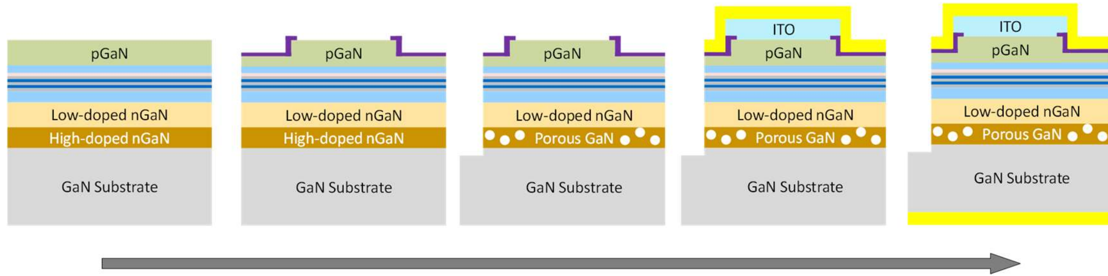

Figure 3-3: Edge emitting laser process flow diagram

The samples were inspected by SEM and it was found that the electrochemical etch was not selective to the intended cladding layer. While the 8 x 10^{18} cm^{-3} Si-doped layer was the target, the 2 x 10^{18} cm^{-3} Si-doped n-GaN layer was also etched. It can also be seen that the NP-GaN slopes down approximately two thirds of the way across the ridge. The bulk non-porous area is where we ultimately see the lasing mode, discussed in the next section. While this problem was unintentional, it allowed us to guide our examination of the lateral and transverse optical and electrical confinement separately.

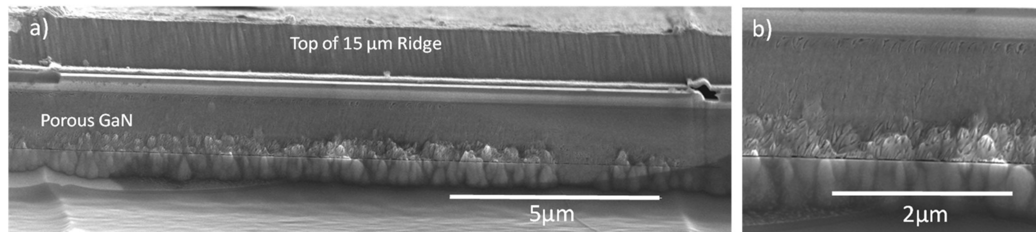

Figure 3-4: Scanning electron micrographs of 1200 µm x 15 µm NP facet. a) Full ridge and b) close view of porous morphology

Using the image analysis technique from chapter 2, the porosity ranged between the etched layers from 15% - 25%. The tapered etch profile suggests there to be a difference between the various etched layers, though no measurable difference was seen by our image analysis metric. These estimates are the basis for our simple laser design simulations below. It should also be mentioned that the NP-GaN led to roughness in the etched facet, but this was low in the device stack and was far outside the range of the optical mode.

3.1.1 Lateral Confinement by porous GaN

The EELDs were tested under pulsed electrical injection, with a pulse width of 500 ns and a duty cycle of 5%. Images were taken of the nearfield emission profile during operation of two representative 900 µm x 15 µm devices, one with NP-GaN and one without. The standard GaN device shows relatively uniform emission across the entire device ridge at both low current density and high current density, where it is behaving as a laser. Looking at the NP-GaN clad device, the spontaneous emission at low currents is uniform across the ridge. The high current testing shows that it is reaching laser threshold, but only on a very small portion of the ridge coinciding with the bulk GaN region of the device seen in SEM.

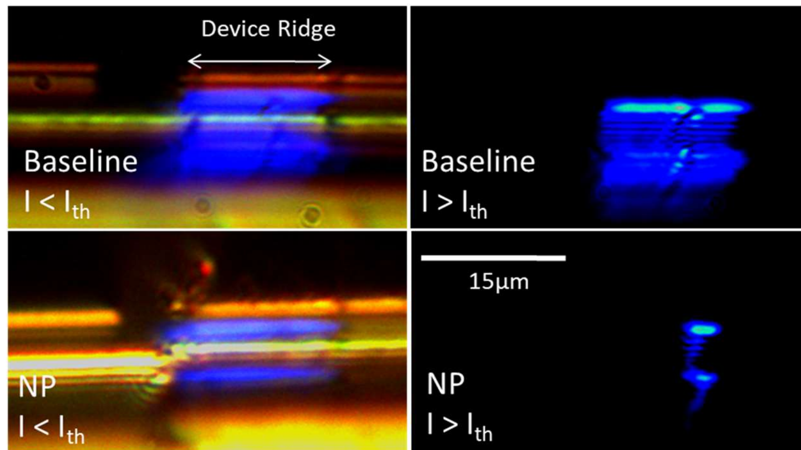

Figure 3-5: Near-field emission profiles of laser ridges under operation at 50x magnification. Left images are below laser threshold, right images are above laser threshold. Top images are for the baseline, bottom are for the porous laser.

Using the commercial finite difference mode solver FIMMWAVE [56], optical modes were simulated to help explain this laser behavior. The NP-GaN profile was estimated as a tapering profile of the porous front, assuming refractive indices for the GaN at 2.47 and porous GaN at 2.25 by using the volume average theory model [57]. The mode profile shows agreement with the lasing mode shown by near-field imaging, with a narrow mode optically confined to the bulk part of the ridge.

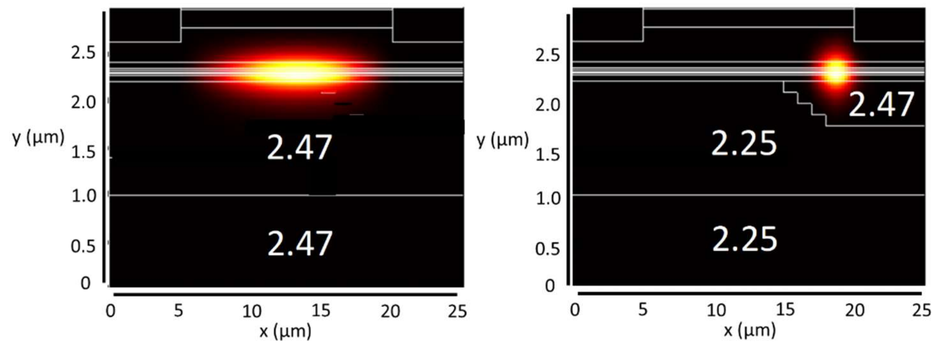

Figure 3-6: Simulated optical modes of the baseline and tapered NP-GaN EELDs. Numbers in white are the refractive indices of GaN and NP-GaN.

3.1.2 Electrical properties

A comparison of the light-current-voltage (LIV) characteristics of 900 μm x 15 μm bars helps evaluate the electrical characteristics of the porous GaN material. The threshold current density (J_{th}) of the baseline was 2.6 kA/cm^2 with a slope efficiency of 0.85 W/A at a peak wavelength of 430 nm. The NP-GaN laser had a J_{th} of 4.8 kA/cm^2 and slope efficiency of 0.14 W/A. The excess voltage of the porous laser was 2.8 V across a 1.2 μm thick layer at 7.4 kA/cm^2. This suggests the electrical resistivity of the porous material to be 3.2 Ω-cm,

higher than what has been reported in literature [58] and what will be seen in future experiments. It is difficult to tell why the NP-GaN resistivity for this batch is so high, but we speculate it is because of the order of magnitude lower Si doping in other nGaN layers.

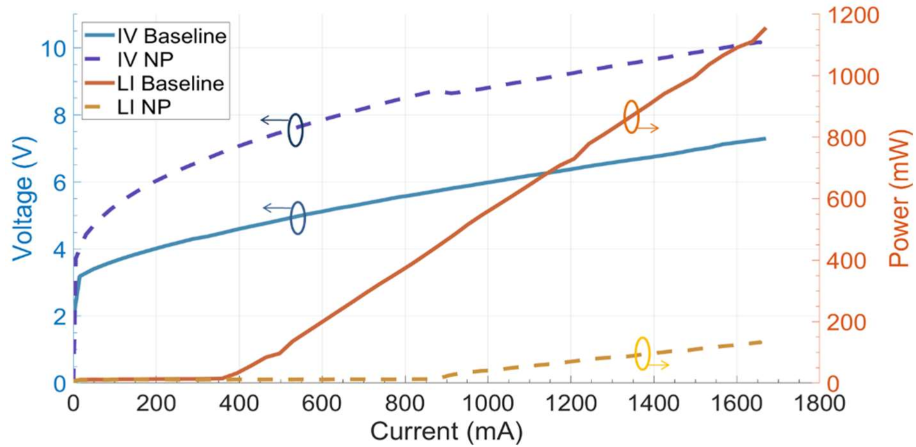

Figure 3-7: Pulsed LIV plot for 900 μm x 15 μm size ridges comparing baseline against NP EELD. Light was collected from both facets using Thor Labs integrating sphere.

Current injection was not limited by the NP-GaN, suggested by the uniform emission at low current densities in near-field imaging. It is also not scattering because the high current density imaging shows no scattering above laser threshold. Estimating the spreading resistance of the thin pGaN layer as 150 Ω for holes from the center of the ridge to the center of the lasing mode, it is only 4 Ω vertically through the NP GaN. The problem then becomes low injection efficiency.

3.1.3 Optical properties and lasing characteristics

The poor efficiency of the NP-GaN laser must be explained by low injection efficiency or high internal loss. The variable stripe length method of plotting the inverse of the differential efficiency against the cavity length found an injection efficiency for the baseline of 63%. This could not be performed for the NP-GaN lasers because only a few devices reached laser threshold. Since the lasing mode was only on a small portion of the ridge, we assume carriers outside the lasing mode were wasted, and scale the injection efficiency by a quarter of the baseline to 16%. The mirror loss is then estimated as 6.5 /cm, giving us a high internal loss of 35 /cm, more than double the 16 /cm calculated for the baseline.

We didn't see any impact of the porous GaN on the vertical mode because it was already confined by the InGaN waveguide layers, calculating overlap as only 0.01%. We assume optical scattering from the porous layer did not play a role in the lasing mode for these devices. For the same reason, there was no change in the mode overlap with the p-side material or ITO compared to the baseline.

We note the possibility of etching of the active material. Though not visible in any of our FIB-SEM examinations, we cannot rule out that it was exposed during the etch and was lightly etched porous. The best evidence against this was from micro-fluorescence imaging, which did not show any difference in emission between areas on an etched ridge and areas outside the etched regions.

3.1.4 Thermal properties

Testing was done varying the pulse with and duty cycle to better estimate thermal properties of the porous GaN material. A 1 μs pulse width was kept constant while decreasing the period to reach duty cycles from 1% to 94% and measuring peak wavelength. The temperature dependence of wavelength was measured previously at 0.03 nm/k, which was used to find the temperature dependence on power dissipation: 27 K/W for the baseline and 44 K/W for the NP GaN lasers.

Using a 2D finite element method solver [59], the continuous wave performance was simulated to estimate heat generation. The resistivities used for the pGaN was 1 Ω-cm, nGaN 2×10^{-3} Ω-cm, NP-GaN 3.2 Ω-cm, and anode contact layer at 5×10^{-5} Ω-cm^2. 12 W/m-K was used to simulate the interface between the backside Au metal contact sitting on the rough copper stage heat sink at 20 °C. Setting the thermal conductivity of the porous GaN layer to 4 W/m-K gave good agreement between the model and the actual temperature rise at 1 A operating current for both the baseline and porous lasers. This falls well within the reported range for porous GaN thermal properties between 1-15 W/m-K [58].

3.2 Increased silicon doping in porous GaN cladding

The electrochemical etch used to form NP GaN is conductivity-selective, so tightly controlled porous layers requires careful design and growth of doped n-GaN layers. To see the porous GaN used as cladding, the electrochemical etch selectivity must be improved to the target layer. The strategy to improve selectivity was to use higher doping of a target cladding layer and lower etch voltage to prevent the other layers from etching. Starting with

a series of simple growth experiments, the laser stack was designed with a higher doped nGaN layer intended to be electrochemically etched into porous cladding.

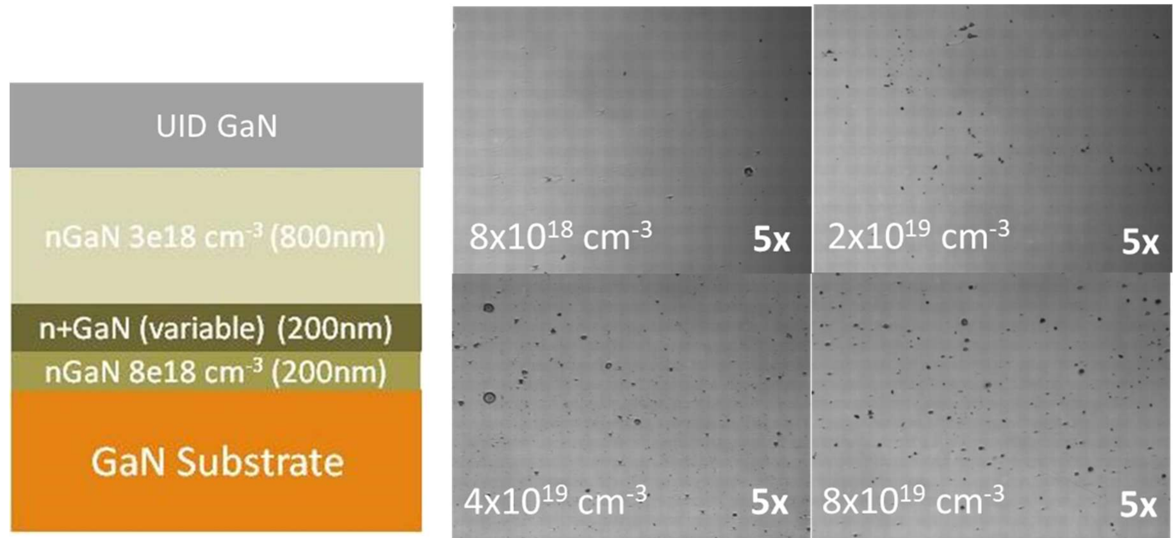

Figure 3-8: Test structure layer stack and optical microscope images of epi growth morphology with higher Si doping in target cladding layer. Higher doping led to large density of pit defects nucleating in the highly doped layer.

Higher doping during growth of the target cladding layer resulted in deep pit defects detrimental to laser device performance. A balance was struck to reach as high of doping as possible for etch selectivity. It was decided in future runs to use 3×10^{19} cm^{-3} where the pits only affect a small portion of devices but still get the added benefit of higher etch selectivity.

3.3 New design for porous GaN cladding blue lasers

The epitaxial structure using a higher doped cladding layer was designed to match optical mode confinement with a laser using typical material for cladding. The structure and calculated optical mode profile are seen in Fig. 3-9. The growth and fabrication were similar to the first batch. Still grown with atmospheric pressure MOCVD on the $(20\bar{2}\bar{1})$ plane, the main difference was adding in the 200 nm highly doped layer to the epi stack. A GaN buffer of 400 nm of unintentionally doped (UID) GaN and 400 nm of 2×10^{18} cm^{-3} Si-doped n-GaN was grown at 1180 °C. Then, 180 nm of heavily Si-doped n-GaN (3×10^{19} cm^{-3}) was grown, intended to serve as the n-side cladding after later porosification. This was followed by 240 nm of lightly Si-doped n-GaN and 100 nm of n-$In_{0.01}Ga_{0.99}N$, both at 2×10^{18} cm^{-3} and 1000 °C, before 35 nm of UID GaN and a quantum well (QW) active region with 2 periods of 3 nm $In_{0.18}Ga_{0.82}N$ QWs and 7 nm GaN barrier layers grown at 863 °C. After ending on a barrier, a 20 nm p-$Al_{0.28}Ga_{0.72}N$ electron blocking layer (EBL) was grown at 1000 °C doped with 3×10^{19} cm^{-3} Mg, and 1000 °C p-GaN with 2×10^{18} cm^{-3} for 200 nm and 1×10^{20} cm^{-3} for 20 nm.

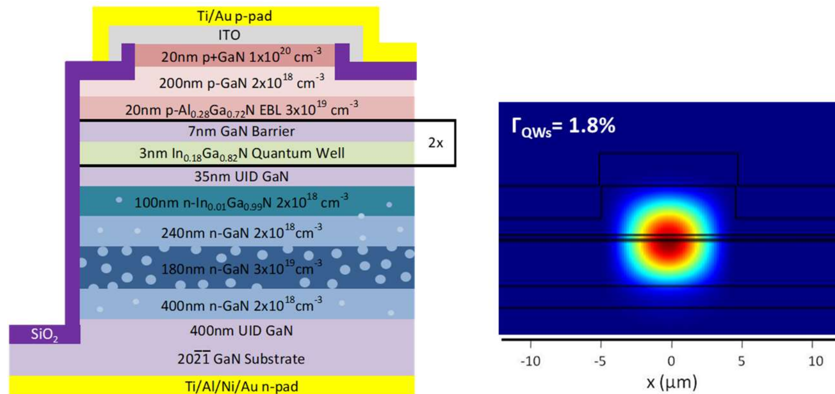

Figure 3-9: NP GaN device schematic and simulated mode profile with optical confinement factor of the mode over the quantum wells

After etching the trench, an indium dot was soldered onto the sample instead of a backside metal pad for holding in the acid. The sample was electrochemically etched under 5 V of applied voltage for 7 hrs. These were then fabricated into bars in an identical manner to the first batch of porous GaN lasers. Pulsed measurements for under 500 ns pulses with 0.5% duty cycle. The substrate was thinned to 150 µm and soldered to a copper block heat sink for CW testing.

3.3.1 Blue laser results

While the porous cladding devices were designed with higher silicon doping for better etch selectivity, SEM of the facet reveals the lower doped layers were still porous. This was only at 3%, versus the target cladding layers 33%, it is the source of issues discussed in the following sections. It can also be seen that the substrate/epi interface was etched. This consistently happens even with GaN-on-GaN substrate growth, and we attribute it to contaminants at the growth surface, though this is only speculation. Several

devices were cross sectioned with FIB to verify the porosity is uniform across the ridge and is assumed to be so for each measured bar.

The thicknesses of particular layers were measured from the SEM image. Using VAT to estimate the index of the porous material, and simulations from the mode-solver package of Lumierical [60], the modal confinement was calculated to be 1.8% over the active region. Since the UCSB laser structure uses thin pGaN with ITO cladding instead of pAlGaN cladding, the mode profile is asymmetrically towards the n-type GaN. While the porous cladding was expected to balance the mode, inspecting the profile shows that the epitaxial design could still be further improved to increase the modal confinement over the wells.

A representative 1200 µm × 8 µm ridge was measured under pulsed electrical injection and reached laser threshold at a current density of 4 kA/cm^2 with an emission wavelength of 454 nm. Devices held above the surface of the acid during the etch did not reach threshold because they were not made porous and had no n-side cladding.

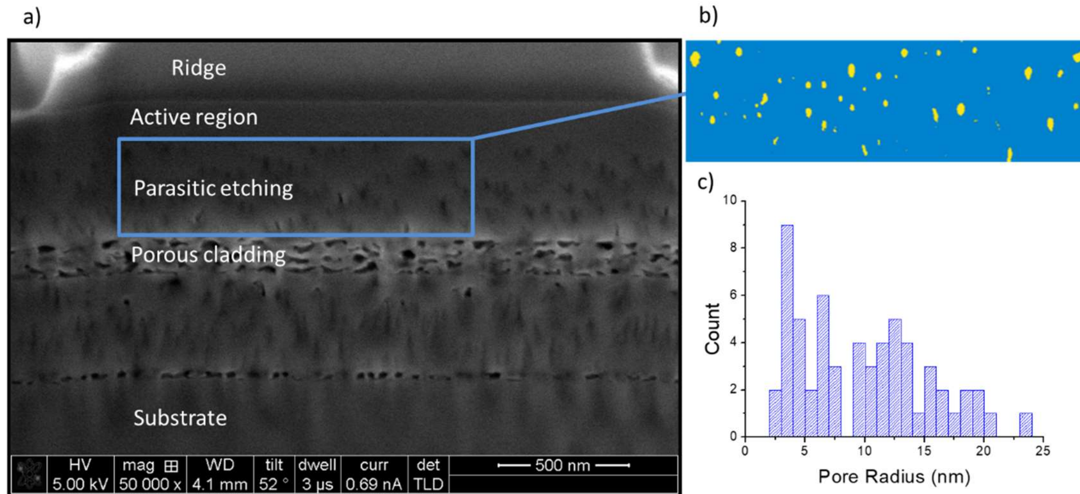

Figure 3-10: Scanning electron micrograph a.) of CAIBE facet, b.) segmented to extract porosity in layer of interest, and c.) pore distribution above target layer

The current path is presumed to be through the unetched material remaining in the porous layer since the n-side contact is on the backside of the substrate. It is thought that the electrical conductivity of the porous layer is not compromising performance since the resistance of the laser is not significantly higher than previous reports [41]. By estimating the nGaN resistivity as 1×10^{-3} Ω-cm, we can calculate the resistance across the porous GaN. An approximately 30% porous layer would have about 1.3×10^{-3} Ω-cm in we neglect scattering, but probably less than 1×10^{-2} Ω-cm if electrical scattering is considered, adding only a negligible 2 mΩ to the total resistance.

The slope efficiency is 0.24 W/A, very low compared to past traditional lasers which have been reported as high as 1.4 W/A [41]. Using the variable stripe length method with an assumed mirror loss of α_m = 14.3 cm^{-1}, the injection efficiency is 60% but with very high internal loss of $\langle\alpha_i\rangle$ = 82 cm^{-1}. As a confirmation, segmented contacts were measured

yielding a similar value for internal loss, $<\alpha_i> = 65\ cm^{-1}$. This high loss comes from scattering in pores of the unintentionally etched low doped nGaN layers. Though the porosity is low, the optical mode overlaps with this region by 30%, resulting in a high impact on the overall loss.

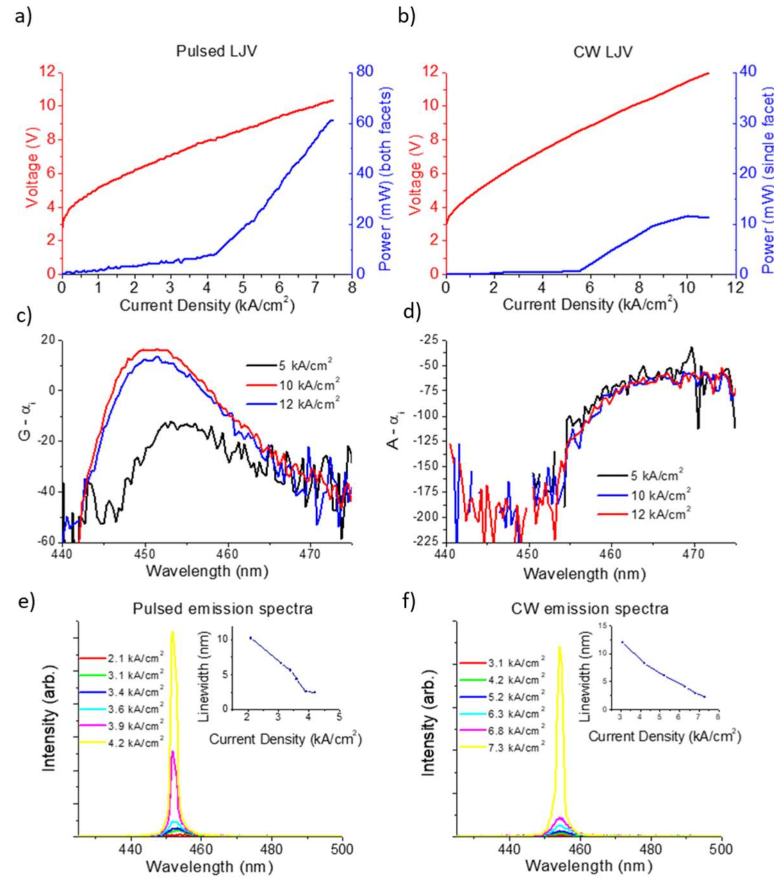

Figure 3-11: a) Pulsed LJV and b) CW LJV. Segmented contacts were used to measure c) gain curves and d) absorption curves at varying current density under pulsed operation. e) Pulsed emission spectra and inset linewidth. f) CW emission spectra and inset linewidth. Spectrometer resolution is 2 nm. Device dimensions are 1200 µm × 8 µm.

The porous devices reached threshold under continuous wave operation at an even higher current density of 5.5 kA/cm2 and lower slope of 0.06 W/A. The power also drops off because of the heat generating in the active region – as discussed in the last batch, the low thermal conductivity of the porous GaN layer presents a difficult problem for heat sinking and needs to be investigated.

Calculating the differential modal gain found it to be low at 4.5 cm/kA. Using the injection efficiency and confinement factor, the material gain was only 600 /cm at 4 kA/cm^2. There is little explanation why the gain would be so low for this material, but one clue could be that a typical cladding laser was also fabricated from this batch with low gain, suggesting growth issues at the time of this device development.

3.3.2 Scattering loss due to NP GaN

Though several groups use Rayleigh, Mie, or Tyndall frameworks to evaluate scattering, the porous GaN material is complex and pipelike in three dimensions. Lumerical finite domain time dependent (FDTD) modeling was used to estimate the scattering of the porous material [60]. A cylinder representing a single pore was positioned perpendicular to the optical field, and the pore size and distance from the active region were varied. The refractive index for the porous material was found using VAT, with a pore assumed to be filled with air and have a refractive index of 1.0. The longitudinal simulation length was 4 μm, with a time of 1000 fs and time steps of 0.01 fs each. The model used and automatically generated mesh with minimum spacing of 5 nm, and a finer mesh was added over the pore. Symmetry was used across the lateral direction, and perfectly matched

layers were used for all boundary conditions. The source for the FDTD simulation was the fundamental optical mode.

The optical transmission past a single pore was calculated as a ratio by integrating the power over the entire waveguide 3 μm behind the pore over the power immediately before interaction with the pore.

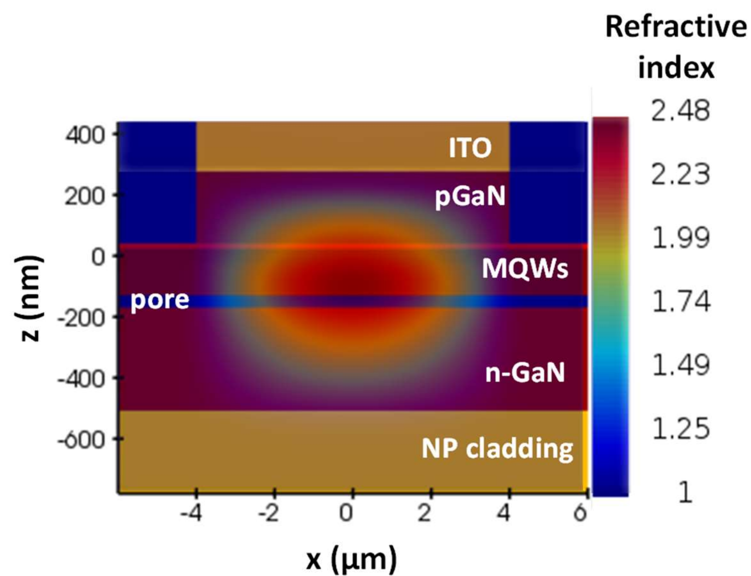

Figure 3-12: Optical mode profile overlaid on index map for the laser structure with single pore used to model scattering

Large pores closer to the MQW active region have a tremendous effect on the transmission because this was where the optical field is largest. Using the distribution of pores measured at the facet, there are only a few pores larger than 20 nm which are spread across the entire area. This justifies the assumption that they will not interact, and these pores can be treated independently. Converting to a distributed loss can be done

with α_{sc}=(1/L)ln(1/T). T is the total transmission, and L is the length over which the pores are distributed. The high measured loss of 82 /cm can be explained by even a few large pores near the quantum wells per micron in the laser cavity, which is confirmed to be the case upon inspection of the laser facet. Though the porous cladding is filled with very large pores in very high density, the index contrast is large enough to prevent significant overlap with the optical mode. The scattering in this layer is likely low because the mode overlap is only 0.13%.

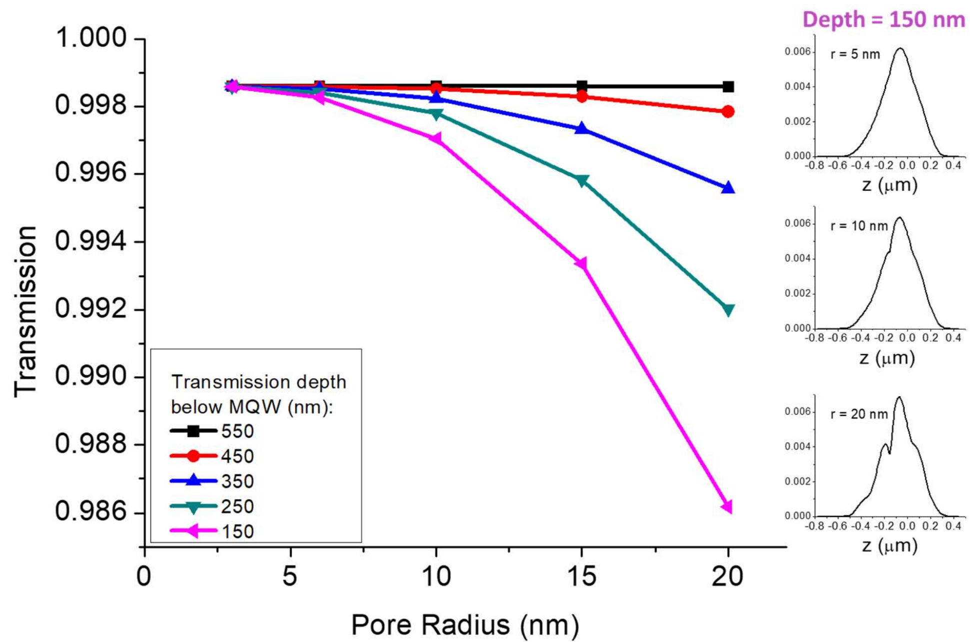

Figure 3-13: Transmission past pores modeled by FDTD. The mode profiles for three different pore sizes at a pore depth of 150nm are shown on the right

Since only the largest pores have an outsized impact on the loss, we can attempt to use the Rayleigh model for scattering considering only the big pores. The spacing of the

large pores is approximately 100 nm, and assuming this is also the case in the third dimension, the void density is 10^{15} cm^{-3}. Only counting pores bigger than 10 nm, with a median void radius of 13 nm, which could be small enough to apply the Rayleigh model. The scattering loss due to pores in silicon has been investigated analytically to be:

$$\alpha_{sc} = N_s(\pi a^2)\frac{8}{3}\left(\frac{2\pi a m_2}{\lambda_{vac}}\right)^4\left(\frac{m^2-1}{m^2+2}\right)^2 \qquad \text{eqn 3-1}$$

where N_s is the volume density of the scattering centers, a is the void radius, m_2 is the refractive index for GaN, m for a void is $1/m_2$, and λ_{vac} is the propagating light in free-space wavelength. Plugging in values for our porous GaN material calculates to be 80 cm^{-1} and well in agreement with the measured loss.

3.4 Fixing etch selectivity

The problem of parasitic etching must be fixed to improve the excess loss. The conductivity of the target layer must be increased relative to the parasitic layers. It would be ideal to increase the Si doping even more to achieve even smaller pores, but as shown earlier this can lead to pits and morphology problems in the crystal growth. While there are techniques such as flow modulation epitaxy, other doping sources like germanium [43], or using other growth planes [42], an easier solution is to decrease the doping in the parasitically etched layer. Dropping the nGaN layer doping from 2×10^{18} cm^{-3} to 2×10^{17} cm^{-3} should prevent parasitic etching, and not significantly affect the voltage. Electron mobility for the 400 nm thick layer should increase from 100 cm^2/V-s to 200 cm^2/V-s [61] assuming

the Si donors are fully activated. Though this increases the layer resistance by 5x, it should only lead to an extra 0.02 V penalty at 4 kA/cm^2 in a 1200 µm × 8 µm ridge.

Laser structures were grown to verify the significance of doping in this layer. Epitaxial "quicktest" was used as feedback to check the voltage. This is where indium dots are soldered onto the grown sample, one on the p-type material and one in contact with the n-type and tested under CW current at 20 mA collecting the light output and IVs. This measurement has arguable correlation to fully fabricated lasers, but we wanted to make sure there were no large discrepancies.

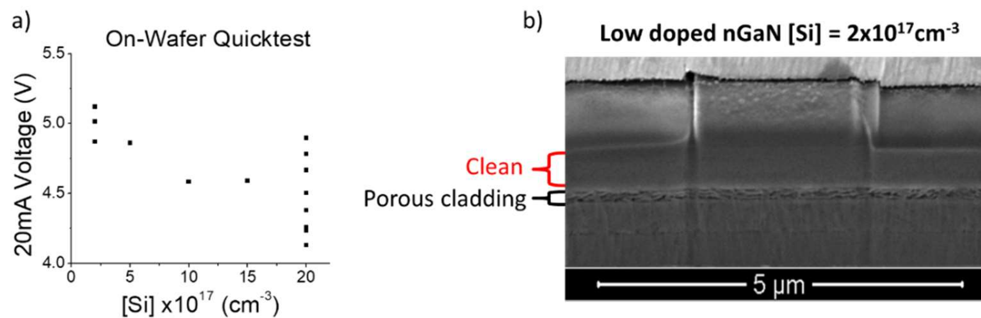

Figure 3-14: a) Epitaxial quicktest voltage with varied doping of low-doped nGaN layer and b) cross sectional SEM image of etched laser structure with perfect etch selectivity

Dropping the doping led to approximately 0.5 V higher voltage at 20 mA, but completely cleaned up the etch selectivity. This is the condition we would continue with when fabricating new lasers, and as it turns out did not affect the voltage of a fabricated device too much.

3.5 Green LD with porous GaN cladding

At longer wavelength emission (green or yellow), the radiative efficiency for GaN drops off. Reaching threshold must have high modal confinement at these wavelengths, but the index contrast for typical III-Nitride cladding layers decreases with a narrower bandgap, weakening the confinement. This makes using NP GaN cladding even more beneficial at long wavelength emission because it maintains high index contrast. Computational studies have shown that NP GaN can increase the optical confinement factor 350% over GaN or AlGaN cladding in a green laser [62]. With the newly fixed porous GaN etch, we moved forward designing green EELDs based on the newly fixed porous GaN etch conditions.

3.5.1 Green laser design and optimization

Green EELDS with NP GaN cladding were designed based off previous best UCSB semi-polar green lasers [63]. The growth substrate was changed to bulk GaN prepared with the $20\bar{2}1$ orientation because it has been shown to allow higher indium incorporation into the active region. The waveguide indium content was reduced to move away from generating misfit dislocations. A highly doped layer was inserted with a Si concentration of $3x10^{19}$ cm^{-3} and other nGaN layers doping were reduced to $1x10^{17}$ cm^{-3} matching the best etch selectivity conditions.

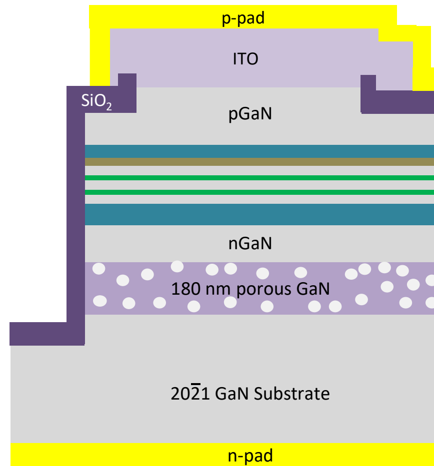

Figure 3-15: General structure for porous GaN green laser

Optical mode simulations were done using Lumerical mode solver [60] to find the optimal placement of the NP GaN cladding and to gain an understanding of how each parameter affects the confinement. Taking the thickness less than 100 nm was an issue, but above that there was little improvement. It is also beneficial to keep the porosity above approximately 30%. Placement of the cladding layer was optimal at approximately 160 nm depth from the active region.

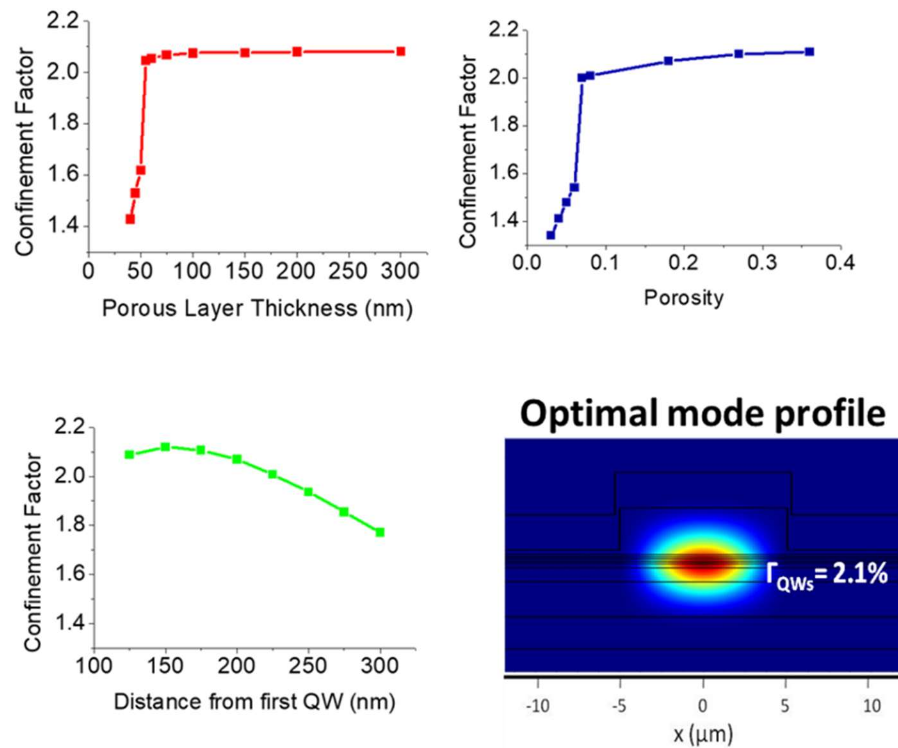

Figure 3-16: Optimization of confinement factor by varying NP-GaN cladding parameters

3.5.2 Green laser fabrication details

Beginning with a 400 nm low Si-doped $2x10^{18}$ cm^{-3} GaN layer used for current spreading in the electrochemical etch, the intended porous layer was grown at $3x10^{19}$ cm^{-3} and 180 nm thick, both at 1180 °C. The temperature was then dropped to 965 °C and the doping taken low to 1 x 10^{17} cm^{-3} to avoid parasitic etch paths during the EC etch, as seen in past studies [64,65]. While 160 nm was the optimal distance from the first quantum well, there were growth morphology issues when the highly Si doped layer was not smoothed out by low doped nGaN. 100 nm of n-GaN was grown and a small amount of indium was incorporated for 80 nm of approximately n-$In_{0.02}Ga_{0.98}N$ before dropping the temperature

again to grow the multiple quantum wells (QWs). This led to a 2.1% confinement factor. 20 nm of UID GaN was grown at 850 °C followed by two periods of approximately 3 nm $In_{0.25}Ga_{0.75}N$ QWs at 760 °C with a 10 nm GaN barrier back at 850 °C. The temperature was increased to 915 °C for the p-side, and a 10 nm p-$Al_{0.28}Ga_{0.72}N$ electron blocking layer (EBL) was grown with 3 x 10^{19} cm^{-3} of Mg doping. A 15 nm p-$In_{0.05}Ga_{0.95}N$ waveguide was grown on top of that, and finally with a two-step pGaN with 245 nm doped at 2 x 10^{18} cm^{-3} and 20 nm doped at 1 x 10^{20} cm^{-3} for electrical contact to ITO.

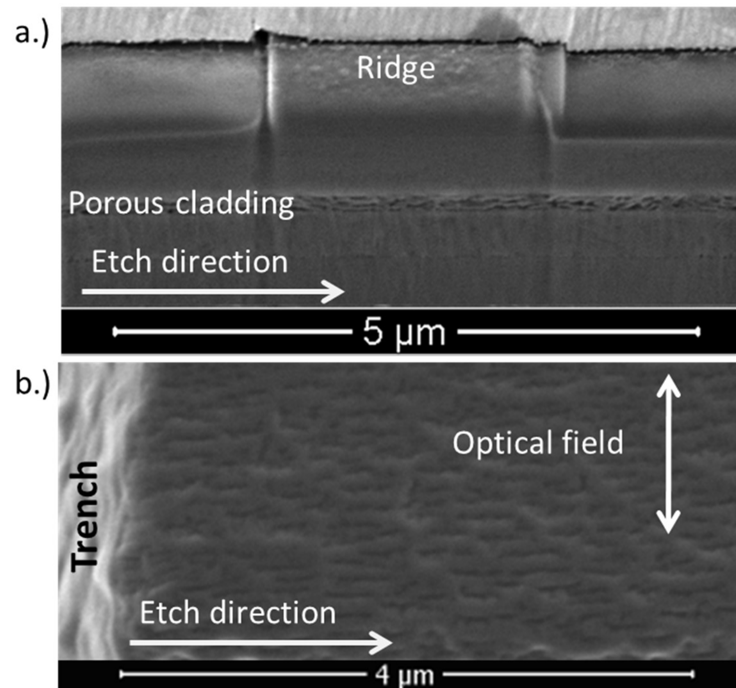

Figure 3-17: a.) Scanning electron micrograph of LD cross section and b.) plane view of porous layer opened by focused ion beam

EELD devices were fabricated the same as previous batches. Electrochemical etch conditions were 5.5 V for 150 min resulting in a porosity of approximately 30%. On-wafer pulsed measurements were at 500 ns with 0.5% duty cycle, and light was collected with a

lens into an integrating sphere. The lens was close enough to the sample to gather light from the facet as well as reflections off of the substrate. CW measurements were taken after soldering the sample to a copper block heat sink.

3.5.3 Green laser results

Pulsed electrical injection measurements shows uniform far-field emission pattern at a wavelength of 510 nm with a slope efficiency of 0.13 W/A. While the maximum power output measured was 150 mW, this was limited by the pulse generator. These results are comparable to some of the best green lasers from this group [63], with lower power but much lower voltage of 7.5 V resulting in a higher peak WPE of 0.9%.

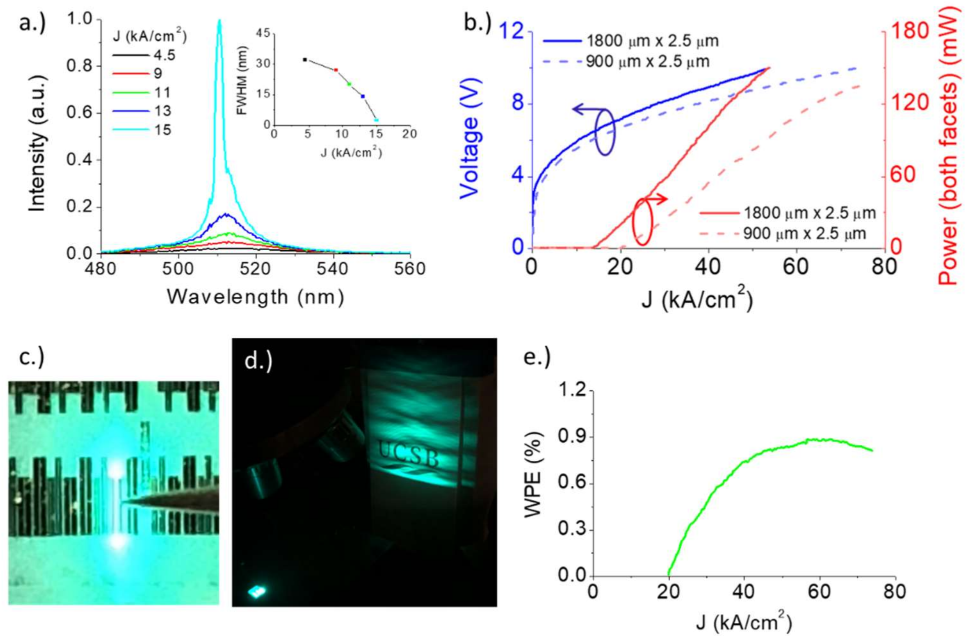

Figure 3-18: a.) EL spectrum inset with FWHM of 1800 µm x 2.5 µm ridge, b.) LJV comparison for two ridges c) Optical microscope image of device under pulsed electrical testing, d.) far-field emission, and e.) peak WPE for a 900 µm x 2.5 µm ridge.

The best threshold current density measured is 14 kA/cm^2 for the longest bars (1.8 mm). High current density operation results in low injection efficiency due to hot carriers overshooting the quantum wells and EBL. The variable stripe method confirms the injection efficiency to be only 16%. There are many reasons that could be causing low injection efficiency. It has also been shown that high indium content quantum wells can exhibit local alloy fluctuations [66]. While it is difficult to characterize without destructive methods, these also impact carrier injection.

Changes to the p-side growth conditions may be a factor causing lower injection efficiency. Previous reports have elaborated on “dark triangle” defects associated with high indium content wells [63], which were ameliorated with colder temperature growth of the p-type layers. Our growths decreased the EBL and pGaN growth temperatures by 40 °C from standard conditions to fix the defective layers, but it’s possible unintended side effects to the doping, or aluminum composition in the EBL affected the injection efficiency. Secondary Ion Mass Spectroscopy could be done to provide evidence for this but requires destruction of the sample. Past experiments have shown that simple optimization of the p-side doping and material quality may also lead to better injection efficiency [41,67].

Reaching longer wavelengths also becomes difficult with high threshold current density because of the spectral blue-shift. While growing on semi-polar planes manages QCSE, we still see a shift over 10 nm when increasing the current density from 4 kA/cm^2 to 14 kA/cm^2. Since we have calculated the optical confinement factor to be a reasonable 2.1%, the threshold current density is likely limited by low material gain or high loss.

We evaluated these parameters with both the variable stripe and segmented contacts characterization methods. The injection efficiency was mentioned above, and the loss calculated with the variable stripe method was found to be $\langle \alpha_i \rangle_{var\text{-}str}$ = 36 /cm. Using this with the mirror loss (estimated as perfectly etched facets) and the optical confinement factor, we can plot up the gain at threshold several devices. With the segmented contacts measurements, we plot up the gain and absorption curves to find the $\langle \alpha_i \rangle_{seg\text{-}ct}$ = 45 /cm, reasonably close to our last estimate. The peaks of the gain curve are also plotted as a function of current density and match well within the points from the variable stripe length method.

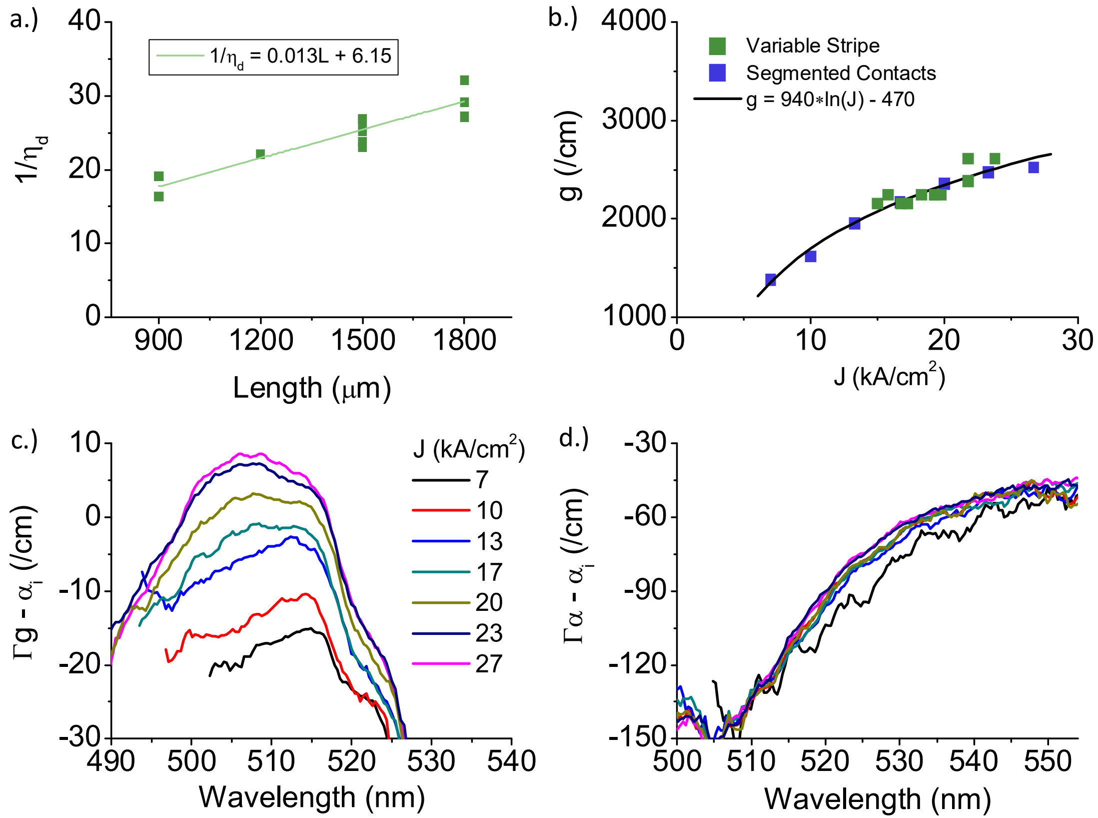

Figure 3-19: a.) Variable stripe length method plotting ridge width against the inverse differential efficiency, b.) material gain calculated from two methods, c.) gain curves and d.) absorption curves from segmented contacts measurements

There are several sources of loss hindering laser performance. Using coefficients from [68] with the simulated optical mode profile, we estimated the free carrier absorption for individual layers presented in Table 3-1. The high doping of the porous cladding layer has such a low mode overlap that the absorption due to free carriers is actually very small. This time the highest absorption is seen in the p-side at $\langle\alpha\rangle_{abs}$ = 23 /cm, which is usually the case for GaN lasers. Better designed lasers see less than 10 /cm [69] of total absorption losses, and future designs will need to balance optimization of the confinement factor with

lower absorption losses in the p-side. There may also be room to reduce p-side Mg doping, but may come at the cost of operating voltage.

Table 1: Values used to estimate free carrier absorption

Layer	carriers (cm^{-3})	Γ (%)	$<\alpha>_{abs}$ (/cm)	$\Gamma<\alpha>_{abs}$ (/cm)
ITO	-	0.3	2000	5.4
p-cladding	3×10^{19}	32.6	41.3	13.5
p-waveguide	1×10^{19}	4.6	18.1	0.8
EBL	2×10^{19}	3.2	26.7	0.9
QW	2×10^{19}	2.1	90.0	1.9
n-waveguide	2×10^{18}	22.0	2.1	0.5
n-cladding	2×10^{18}	15.2	0.7	0.1
porous	3×10^{19}	0.4	41.3	0.2
			Sum	23.2

Though this new laser was highly selective to the target NP GaN cladding layer during the electrochemical etch, there may still be scattering in the porous material. We had previously ignored scattering losses in the porous layer because the modal overlap is low, but the pores are large, averaging more than 40 nm radius when looked at by cross sectional SEM perpendicular to the etch front. We can roughly estimate the scattering as Rayleigh spheres using equation 3-1. Averaging the density of pores using the vertical and transverse plane cross sectional SEM images, we get approximately 1.5×10^{14} cm^{-3}. With a 0.38% modal overlap, the scattering loss is estimated at $<\alpha>_{sc}$ = 21 /cm. We recognize the potential inaccuracy in using Rayleigh spheres as a model for scattering in what are clearly elongated micropipes, but it provides a reasonable account for excess loss, and we'll leave it up to future researchers to perform a full FDTD treatment.

While scattering loss was much lower than the previous batch, it calls into question the ability of porous GaN lasers to compete with state-of-the-art EELDs for performance. The excess loss must be reduced, though there are often tradeoffs. Increasing the porosity can be accomplished by increasing the etch voltage, but this may cause parasitic etching in other layers and increase pore size. Since scattering loss rises to the fourth power with pore size [70], and modal overlap decreases at a low rate relative to porosity after 30% (optimization of confinement factor in section 3.5.1), this path is untenable. Increasing the doping could also increase the porosity while maintaining pore size, or even reducing the pore size by allowing lower voltage. This is the best strategy but will require novel techniques to grow thick layers with very high silicon content while maintain smooth and defect free crystals.

The material gain was fit with $g = g_{on}\ln(J) + C$ to find a gain factor of g_{on} = 940 /cm. Proportional to the momentum matrix element, values comparing different InGaN compositions are in [13]. Green compositions (~24 Indium) are approximately one third of the values for blue compositions (~15% Indium). The gain factor for a semipolar two QW blue laser [41] is g_{on} = 3200 /cm, suggesting that our green EELDs could still use some optimization of the active region material to improve the gain.

While devices were tested under CW electrical injection, laser threshold was not achieved. Linewidth narrowing occurs up to 9 kA/cm^2, which nearly matches the pulsed testing characteristics. After 10 kA/cm^2, the linewidth jumps back up, the spectral intensity peaks, then begins to fall as the wavelength red-shifts. Oscillations form in the spectrum

that are large enough for our low-resolution detector to capture. The redshift and intensity decrease are signs of heat generation.

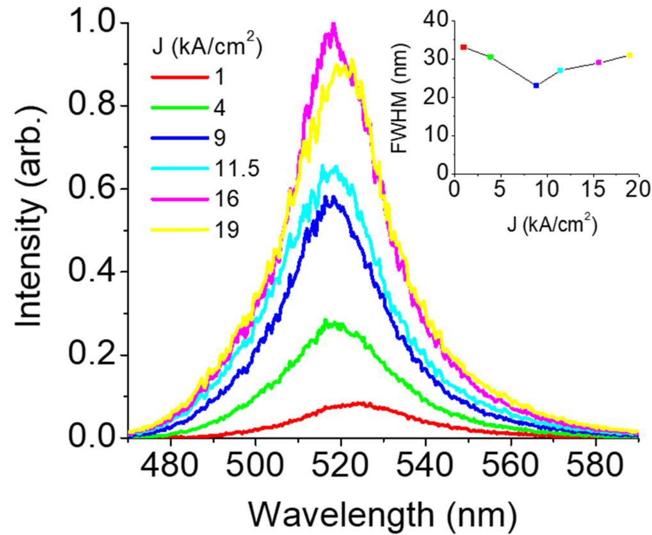

Figure 3-20: EL spectra under CW testing for 1800 µm x 2.5 µm bar soldered to copper block. Inset is the FWHM increasing current densities.

An 1800 µm x 2.5 µm bar was instantly driven to 20 kA/cm^2, where a far-field laser emission pattern was observed and recorded for 32 milliseconds, then vanishing as the laser dropped below threshold. We can use this information to estimate the temperature dependence due to the increase in threshold current density. The thermal conductivity for GaN is 130 W/m-K, while 30% porous GaN is approximately 7 W/m-K [71]. Using 2.67 in [13], the heat flow can be modeled as two dimensional through the 330 µm bulk GaN substrate. This calculates thermal impedance Z_{Tsub} = 0.8 K/W. Heat flow through the porous layer can be modeled as one dimensional since it is only 180 nm thick, with $Z_{Tporous}$ = 0.6

K/W. Summing these gives Z_T = 1.5 K/W, which for the given current and V = 7.2 V results in a temperature rise ΔT = 9.7 K from room temperature. Now using the threshold current density at room temperature Jth = 15 kA/cm^2 with $I_{th} = I_0 \exp(T/T_0)$, we can solve for the characteristic temperature T_0. This represents the temperature dependence of threshold current. Values less than 100 need thermoelectric cooling [13], and in this case is 34 K.

The porous GaN contributes roughly one third of the total thermal impedance, but there are other relatively simple ways to improve the CW performance without needing to adjust the porous GaN conditions. Removing the substrate with photoelectrochemical etching [72] allows only a very thin GaN layer between the active region and heat sink, dropping the thermal impedance in half with a temperature rise only ΔT = 5.5 K. Dropping the threshold current density by reducing absorption and scattering losses is the next big step. If reduced to 4 kA/cm^2, the temperature rise at threshold drops to a reasonable ΔT = 1.1 K above room temperature.

3.6 Porous vs InAlN cladding at longer wavelengths

While the present work has so far been focused on making higher performance green lasers, there is a push to broaden the applicable wavelength of GaN based lasers to yellow and beyond. Direct emission yellow semiconductor diode lasers have not yet been achieved, yet there are several applications, for example in laser cooling to execute cold atomic physics experiments. The sodium atom has an atomic transition at 589 nm, and a collimated narrow beam could be used to cool an ensemble of sodium atoms to near zero Kelvin where photon entanglement may be studied. While other semiconductors can use frequency doubling to

reach this wavelength, these are very inefficient, and a direct emission laser would be a superior source of photons.

There are few reports of GaN EELDs beyond 550 nm lasing wavelength. The longest wavelength lasers use a combination of InGaN waveguides and AlGaN or InAlN cladding to optically confine the lasing mode. At 589 nm, lattice matched InAlN is the only material capable of providing adequate mode confinement for a laser. This alloy is notoriously difficult to grow, requiring long growth times and narrow process windows for temperature, gas flow, and growth rates [73]. Thermal properties for this material are also lacking.

NP GaN could be an effective alternative to InAlN, and 589 nm emission laser designs were modeled using the mode solving package in Lumerical [60] comparing the various parameters. Starting with the green laser designs, waveguide and cladding stacks in the n-side were replaced with porous GaN or InAlN. The number of quantum wells was increased to five with higher indium composition accounting for the low gain expected in an active region at this wavelength.

Only 100 nm of 35% porous GaN material was needed to get an optical confinement factor of 7%. Since the index contrast of porous GaN is so much higher than InAlN at 589 nm, the thickness of InAlN had to be doubled to reach the same confinement factor. The optical mode penetrates deeper into the InAlN cladding, but the scattering losses introduced by porous GaN cladding is concerning enough to warrant any claims about excess loss. It is expected that additional absorption losses in the InAlN cladding will be matched by scattering losses in the porous layer.

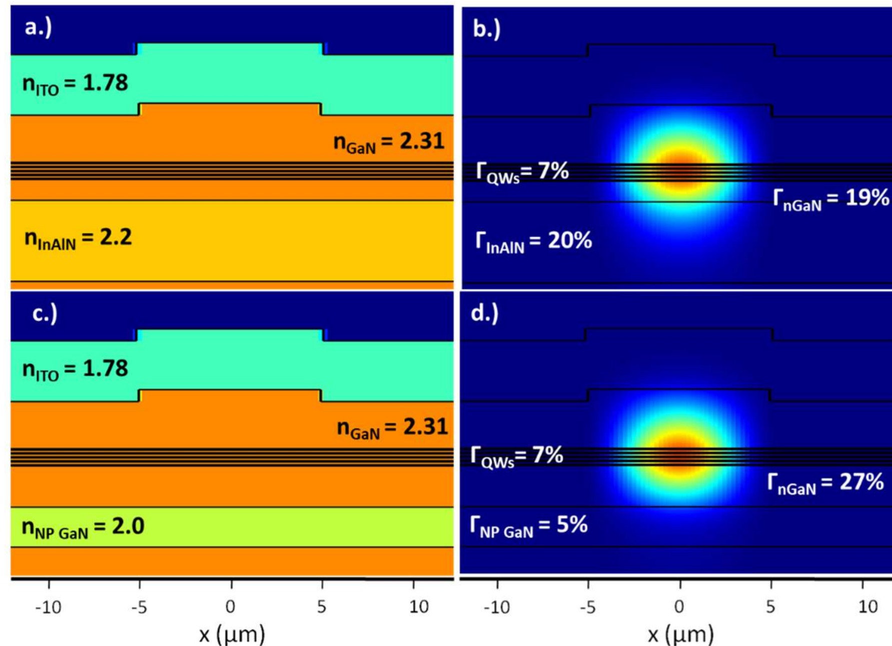

Figure 3-21: EELD designs targeting 589 nm emission a.) InAlN cladding refractive indices, b.) NP GaN cladding refractive indices c.) InAlN cladding fundamental mode, and d.) porous cladding fundamental mode

The thermal conductivity of the 30% porous GaN and InAlN layers are very close at 7 W/m-K [71,74]. Under CW operation there should be a small temperature rise in the InAlN cladding because the layer is twice as thick. While the temperature rise depends strongly on the laser performance, for a 1200 µm × 8 µm laser stripe, the NP GaN cladding impedance would be 1.5 K/W whereas the InAlN would double to 3 K/W.

3.7 Conclusions

The optical properties of porous GaN have been implemented into III-Nitride edge emitting laser diodes on semi-polar substrates. Initial lasers showed confinement of the optical mode in the lateral direction, pushing the beam emission towards one side of the ridge. While parasitic etching prevented a useful improvement to the laser, electrical,

thermal, and optical properties of the porous GaN material were characterized and compared to reported values in literature.

A new batch of lasers was fabricated with higher doping to improve the etch selectivity of the porous material. Though the parasitic etching was not solved, blue lasers were fabricated with porous GaN successfully confining a lasing mode in the transverse direction. Laser action was also seen under continuous wave operation, though the power rolls over quickly due to excessive heat generation. The exorbitant internal losses were associated with scattering in unintentionally etched layers, with numerical modelling used for evidence.

Parasitic etching in lower doped layers was reduced with a combination of higher doping in the target layer and lower doping in layers outside the target with minimal effect on the operating voltage. Updated conditions were applied in green edge emitting lasers, where the NP GaN cladding showed better performance. The green lasers had lower measured loss than previous batches targeting blue. They were comparable in performance to previous best UCSB lasers which used typical cladding, but optimization of the p-side and modelling of the absorption losses is needed to improve the threshold current and slope efficiency. Though the green lasers did not reach threshold under CW testing, there are methods to improve the heat dissipation that may alleviate performance impact. A fundamental solution to lower porous GaN conductivity is still lacking.

Finally, modelling was performed targeting even longer wavelength lasers in the yellow-orange part of the spectrum at 589 nm. Comparisons were made between porous

GaN cladding and lattice matched InAlN. Though NP GaN is an exciting technology to improve long wavelength III-Nitride lasers, there are drawbacks that need to be considered.

4. Porous GaN Distributed Bragg Reflectors

Visible wavelength VCSELs are a research topic for many advantages over their edge emitting laser counterparts, including low beam divergence, low thermal wavelength shift, low power consumption, and high manufacturability. While significant progress has been made in recent years, VCSELs have yet to realize high power and efficiencies performance, inhibited by complex growth and processing.

Since the gain medium of a VCSEL is in the vertical direction, there is significantly lower gain volume interacting with the optical mode. Laser design requires very strong DBR mirrors at or above 99.5% reflectivity to form the optical cavity. While other III/V material systems can easily grow epitaxial DBRs by MOCVD, III-Nitride alloys have a wide variance in lattice constants that make growing DBRs very difficult. The strength of the DBR is determined with:

$$R=\left(\frac{n_{GaN}(n_2)^{2N}-n_{air}(n_1)^{2N}}{n_{GaN}(n_2)^{2N}+n_{air}(n_1)^{2N}}\right)^2 \quad \text{eqn 4-1}$$

Where n is the refractive indices, the substrates indicate the material (1 and 2 for alternating index layers of the DBR), and N is the number of loops. Early DBRs used AlGaN/GaN as the reflective materials, but the tensile strain leads to film cracking that limits the AlGaN composition. With restricted composition, the index contrast remains low, and many periods need to be used, extending growth times and resulting in difficult to achieve uniformity.

Lattice matched InAlN has been used to make high quality DBRs but is compromised by the same issues with growth times and uniformity, needing upwards of 80 periods for high reflectivity [75]. The alternative used at UCSB is a flip-chip structure, where dielectric DBRs are deposited on both sides of the active region [76]. This process has successfully made VCSELs with output power of a several mW, but the complex fabrication introduces problems with heat generation, high processing times, and poor yields. Performance for these “dual-dielectric” DBRs has now lagged behind “hybrid” DBR structures, where the n-type DBR is epitaxially grown and the p-type is a deposited dielectric DBR [75]. Hybrid type GaN VCSELs have achieved over 16 mW output power [77].

NP-GaN offers a lattice matched material with high index contrast. The NP-GaN porosity is easily controlled by epitaxial conditions and is electrically conductive, meaning it can be used to make high quality DBRs. A few groups have now shown VCSELs with this material on c-plane and on m-plane [42,43], but the advantages of NP-GaN material have pushed this group to pursue NP GaN DBRs on semi-polar planes using a buried tunnel junction style contact.

4.1 DBR Fabrication

DBR structures were grown and fabricated to check for quality before implementing into optoelectronic devices. A 300 nm-thick unintentionally doped (UID) GaN buffer layer was first grown at 1180 °C, followed by 16 pairs of alternating doped and UID GaN layers with thicknesses of 60 nm and 45 nm, respectively, targeting the specific stop-band wavelength of 420 nm. The n-type doping was 5.5×10^{19} cm^{-3} measured by SIMS.

Rectangular trenches were etched forming windows to the highly doped material, an indium contact was soldered onto the sample, which was subsequently electrochemically etched at 4 V of applied bias for 2 hrs with 200 rpm stirring.

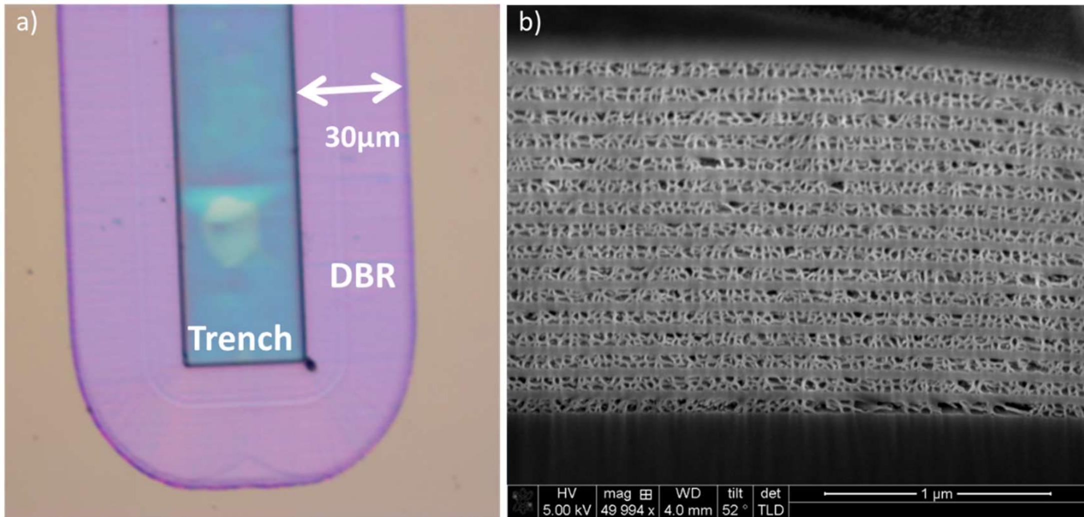

Figure 4-1: a) Top-down optical microscope image of porous DBR from edge of trench. B) FIB cut SEM of porous GaN DBR taken perpendicular to etch front.

Optical microscopy shows the porous GaN lateral etch distance creating a DBR mirror within 30 µm from the edge of the trench. Cross sectional FIB and SEM indicated a porosity of approximately 50% with pore sizes between 30-50 nm, with a refractive index estimated at 1.83 by VAT (Volume Average Theory) at 440 nm. To estimate the strength of the DBR, a commercial Thin-Film UV-Vis spectrometer (Filmetrics F10-RT-UVX) was used. Since highly reflective dielectric based DBRs have been fabricated at UCSB, a 12 pair SiO_2/Ta_2O_5 DBR deposited on a polished sapphire substrate was used to calibrate the reflectivity measurements.

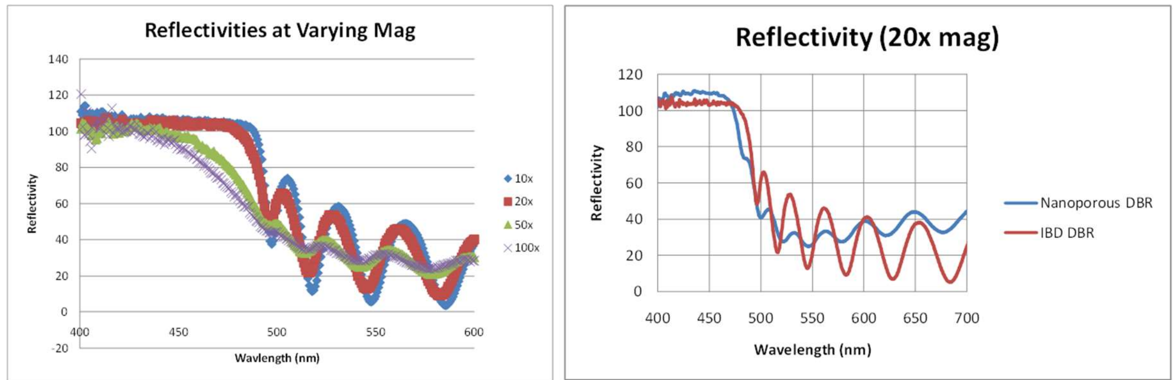

Figure 4-2: a) Reflectivity spectrum for dielectric DBR at different magnification levels. Higher mag shows washing out fringes in spectrum. b) Measured reflectivity of porous and dielectric DBR deposited by Ion Beam Deposition (IBD)

The DBR is over a very small area (30 μm), so reflectivity must be detected through a lens. While low magnification shows good agreement between measured reflectivity and an ideal DBR, higher magnification uses large numerical aperture lenses. This lowers the acceptance range for reflected light, resulting in a narrower stop-band emission as well as washed out fringes as seen in Fig 4-2. The other major issue is sensitivity at high reflectance values. As can be seen from the recorded spectrum, it is difficult to measure reflectance near 100%, and the recorded measurements for both the porous DBR and dielectric DBRs resulted in reflectivity over 100%. This is physically impossible, but we presumed that the porous mirrors are near 100% or close enough to attempt fabricating a VCSEL device.

4.2 GaN VCSEL development

The initial VCSEL design started with previous work out of UCSB. Instead of a dual-dielectric design, the n-side DBR was simply replaced with a NP GaN DBR. This was uniquely based on the semi-polar $(20\bar{2}\bar{1})$ substrate and buried tunnel junction contact to provide lateral electrical and optical confinement. The unique features of this design compared to other research group VCSELs are detailed in Table 4-1 below.

Table 4-1: Key features of UCSB design compared to reported VCSELs with porous DBR

Mishkat-Ul-Masabih *et al* [42]	UCSB	ElAfandy *et al* [43]
▪ DBR Si doping 1e19 cm^{-3} ▪ 16 period DBR ▪ m-plane ▪ 8λ cavity ▪ ITO, ion implant ▪ 3.5mW, 410nm	▪ DBR Si doping 6e19 cm^{-3} ▪ 16 period DBR ▪ 20-2-1 plane ▪ 9λ cavity ▪ BTJ	▪ DBR Ge doping 6e19 cm^{-3} ▪ 25 period DBR ▪ *c*-plane ▪ 6λ cavity ▪ ITO, SiO_2 ▪ 0.15mW, 435nm ▪ Conductive DBR

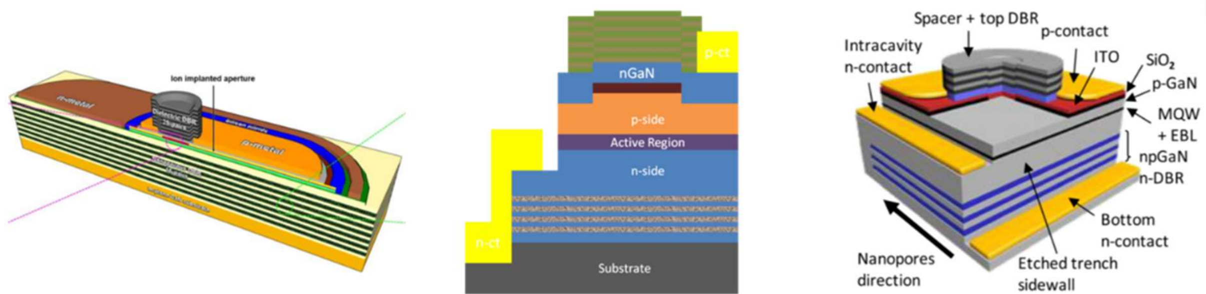

A few high-level considerations for designing and fabricating GaN VCSELs will be discussed in the following paragraph, but a thorough guide can be found in Kearns *et al* [78]. Sandwiching laser material between two highly reflective mirrors forms an optical cavity. The cavity is only partially filled with gain material, so the standing wave of the

electric field that forms within the cavity should be maximized over the active material to augment gain. Loss should also be minimized by minimizing overlap of the standing wave with regions that are highly absorbing at the target wavelength. The high doping inherent in buried tunnel junction architectures would typically be a major source of loss, so the optical field must be carefully designed for a minima in this region of the cavity.

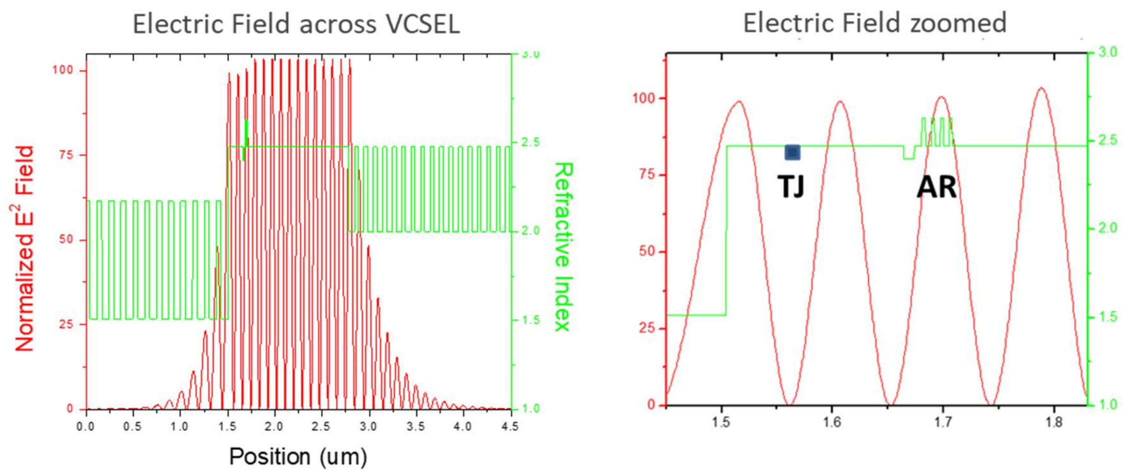

Figure 4-3: Profile of the electric field across the entire VCSEL structure mapped by refractive index. The axes are zoomed in on the right to focus on minimization of the field over the tunnel junction and maximization of the field over the active region.

The emission wavelength of a VCSEL is determined by the cavity length. The length of a round trip in the cavity must be a multiple of the emission wavelength for resonance to occur. Since the cavity in our VCSEL design is relatively short (approximately 10x the wavelength), this means that layer thicknesses must be tightly controlled. Aligning the

resonance modes to the peak of the gain media as well as the DBR stopband wavelengths is one of the difficult challenges when fabricating a VCSEL.

4.3 Details of VCSEL Fabrication

VCSEL material was grown with MOCVD on the $(20\bar{2}\bar{1})$ plane of a bulk GaN substrate. The DBR had the same growth conditions as detailed in section 4-2, with the addition of four more loops to the porous DBR to ensure high reflectivity. Following growth of the highly doped DBR with 16x loops, temperature was dropped to 1000 °C to grow 20 nm of low Si-doped nGaN for current spreading and 390 nm of very low Si-doped nGaN for smoothing out the morphology. The temperature was dropped again to approximately 865 °C to grow 270 nm of UID GaN for mode placement, and to prepare for growth of the quantum wells. Two loops of a 3 nm quantum well composed of $In_{0.18}Ga_{0.82}N$ with 7 nm GaN barriers were grown. Then the temperature was raised back to 1000 °C to grow a 10 nm p-AlGaN doped with Mg at 3×10^{19} and a pGaN low at 2×10^{18} cm^{-3} for 105 nm. Finally, 10 nm of very highly doped p+GaN was grown at approximately 1×10^{20} cm^{-3} Mg for the tunnel junction contact.

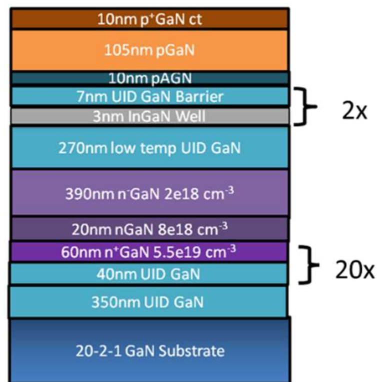

Figure 4-4: NP GaN VCSEL layer stack

Photolithography was used to pattern a buried tunnel junction, and samples were briefly etched with a BCl_3/Cl_2 RIE for several seconds creating an aperture approximately 15 nm in height. After the photoresist was removed, samples were cleaned in aqua regia, BHF, and solvents to prepare the surface for a regrowth in the MOCVD chamber. The temperature of the chamber was ramped up to 1000 °C and 10 nm of highly Si-doped nGaN was grown at 1×10^{20} cm^{-3} to complete the tunnel junction. Then, roughly 80 nm of low doped 2×10^{18} cm^{-3} nGaN was grown as a current spreading layer burying the tunnel junction.

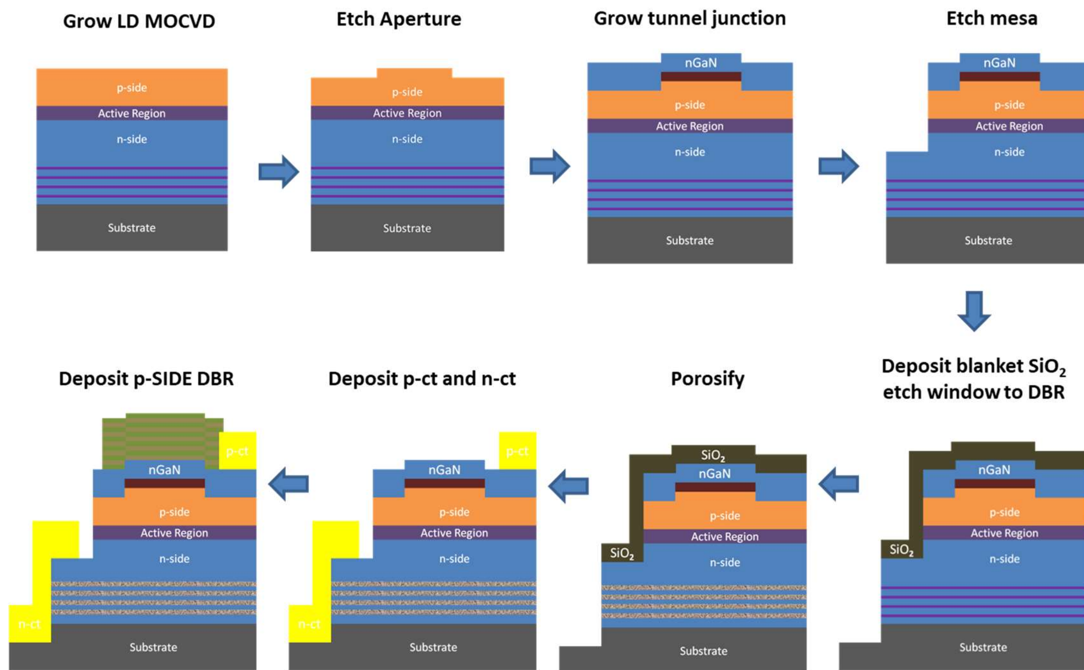

Figure 4-5: VCSEL fabrication process flow

Mesas were etched using Cl_2 reactive ion etching, opening the n-type material for later contacts. 200 nm of SiO_2 was then deposited as a hard mask, and trenches were

opened next to the mesa as a window to the highly doped material below, again with BCl_3/Cl_2 based RIE. Indium was soldered onto the side of the sample, which were then electrochemically etched to porosify the n-side DBR at 4 V for 2 hours matching the conditions u calibration samples. At this point the reflectivity of the lower DBR is measured. Metal pads are simultaneously deposited on the p-side as well as a universal n-contact. Finally, the p-side DBR is deposited on top of the aperture. This was done via ion beam deposition as 12 loops of SiO_2/Ta_2O_5 targeting 435 nm as the middle of the DBR stopband with thicknesses of the SiO_2 = 74 nm and Ta_2O_5 = 50.5 nm.

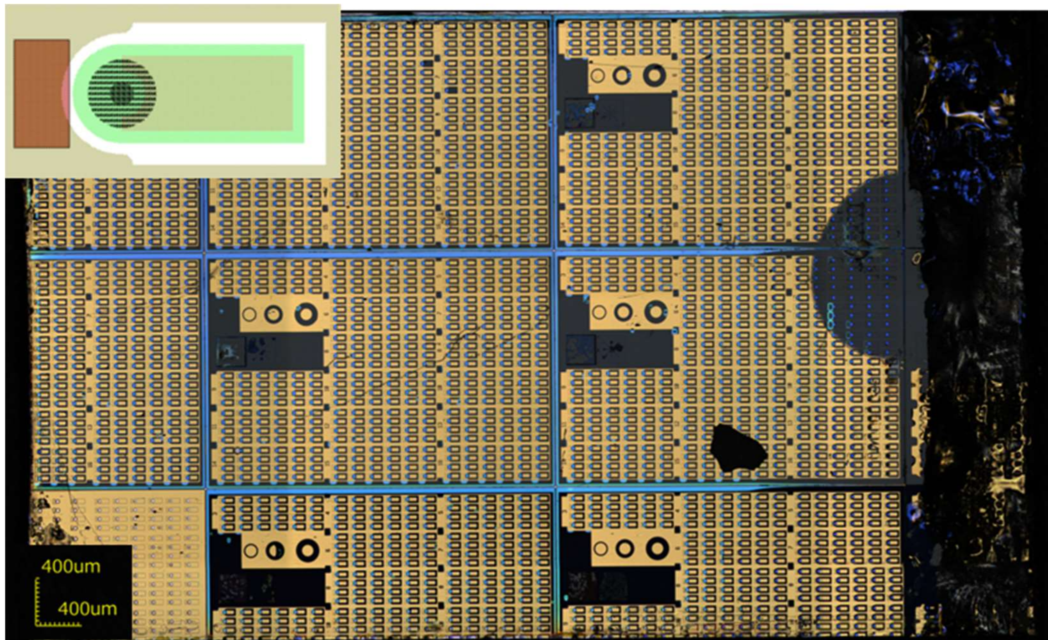

Figure 4-6: Optical image of completed sample inset with mask layout for an individual device. Dark area on right is remaining indium contact where the tweezers hold the sample during the electrochemical etch.

Electrical testing was taken under pulsed conditions at 200 ns pulses with 0.5% duty cycle. Since the tunnel junction is buried during MOCVD growth, the contact is activated through slow burn-in by continuous wave testing until the spontaneous emission is uniform across the aperture, then pulsed LIV measurements are taken.

4.4 Results of VCSEL batch

Devices were electrically tested depositing metal pads and before the p-side DBR. Testing the spectral peaks can inform the design of the p-side DBR, since a passive spacer layer can be added underneath the DBR targeting a desired cavity thickness. The peaks in the spectrum correspond to the resonant wavelengths in the cavity and vary widely across the device. We attribute this to variations in porosity, the cavity length, and the emission wavelength of the active region in different areas of the sample. This can be a good thing, since minor variations across the sample provide experimental comparisons across the same epitaxial growth conditions. Variations in the porosity may negatively affect the porous DBR reflectivity and could be a hindering factor in our development of NP GaN VCSELs, discussed further below. Since there was such a wide variance in the resonant cavity peaks, no spacer layer was added to the p-side DBR deposition, and completed devices were now tested.

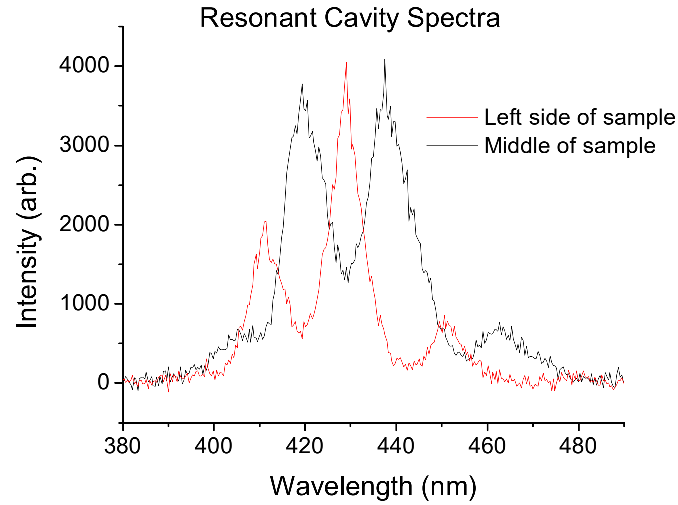

Figure 4-7: Resonant cavity spectral peaks under electrical testing (with porous DBR only)

Narrow emission peaks were observed, but there was no laser behavior. The porous GaN DBR was designed to have higher reflectivity than the upper DBR promoting lasing out of the top facet, but spectra were measured from both sides and found similar emission characteristics.

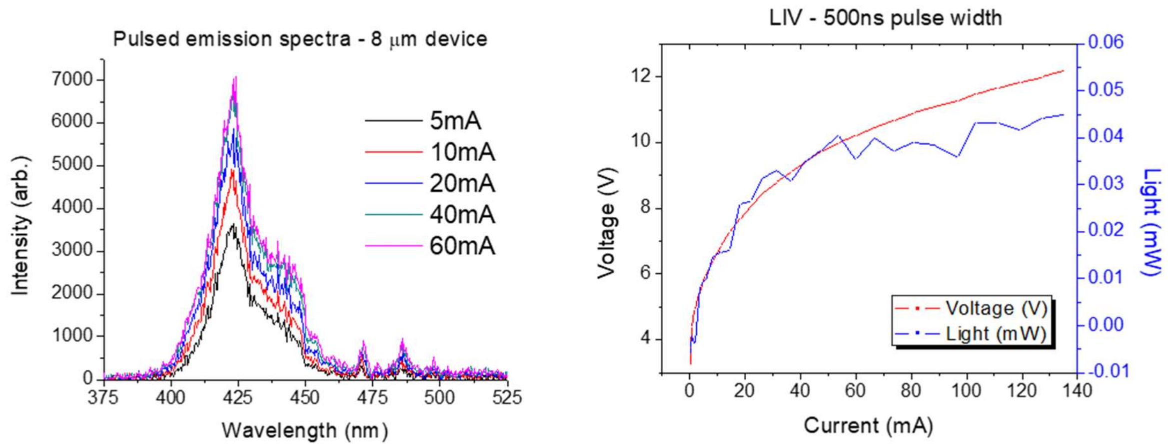

Figure 4-8: Spectral intensity of pulsed electrical operation increasing current and LIV plots for a representative 8μm device

Inspection of the IV curve shows a very slow rollover. While the device turns on around 4 V, it is with very high resistance and takes significantly higher current to flatten. Similar behavior has been seen with buried tunnel junction type contacts in this group on working VCSEL devices [79]. Though it may not be an ideal IV curve, it is likely not the key issue preventing laser threshold.

From the images taken of the device under operation, the emission is uniform across the circular aperture, but there is a bright semi-circle in the lower part of the image. This is amplified spontaneous emission that reflects off the lower porous DBR but outside of the upper dielectric DBR. This is responsible for the wide emission peak measured in the spectrum between 400-450 nm.

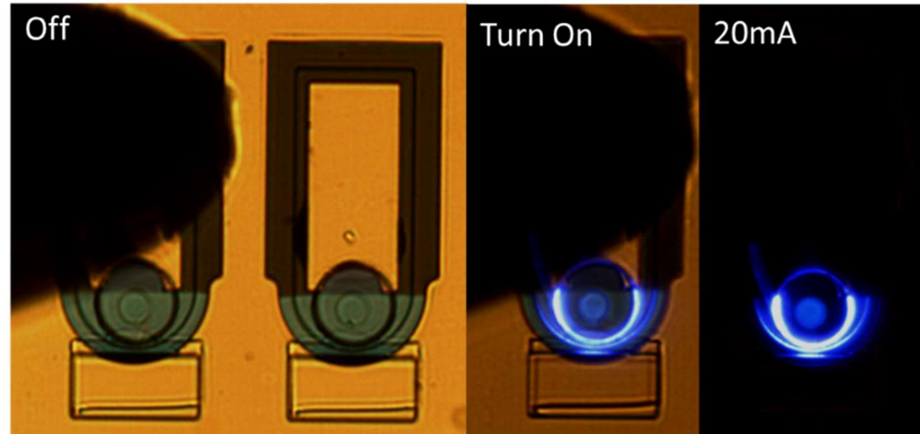

Figure 4-9: Top-down optical images of porous GaN devices under operation. There is no laser behavior.

There are several possible reasons the porous GaN VCSEL devices did not achieve laser action, but significant evidence suggests the porous DBR is not strong enough. The porous DBR is the only difference from the working devices in [79], as the material growth

quality, cavity design, and buried tunnel junction contact are nearly identical. There are also clues from the reflectivity spectrum calling into question the true reflectivity of the measured mirror.

It becomes difficult measuring the reflectivity spectrum near 100% as it relies significantly on the source used for calibration and local features. A reflectivity spectrum was taken of a dielectric DBR known to be ~100% reflectivity at two locations and a 5% difference in the peak reflectivity was measured.

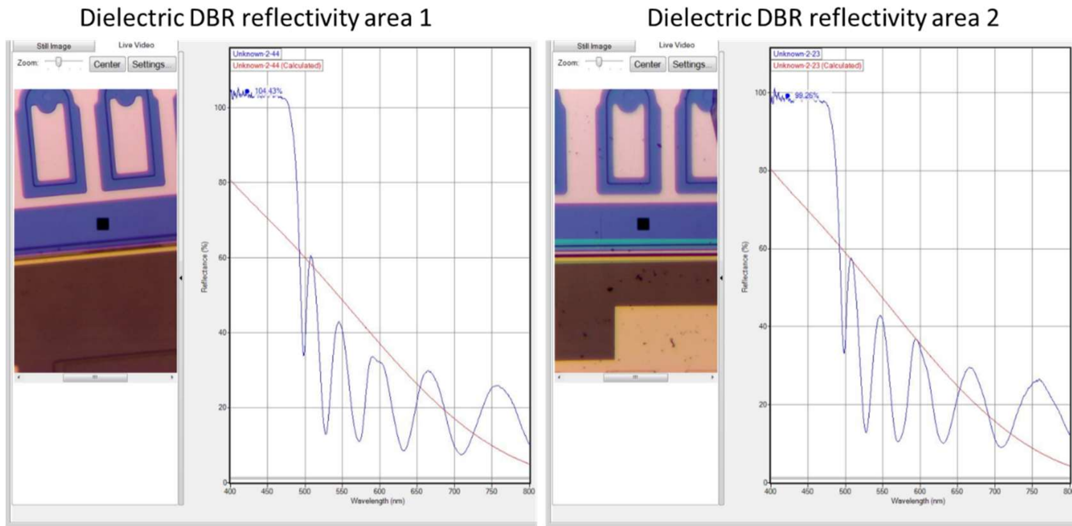

Figure 4-10: Difference in dielectric DBR reflectivity spectrum taken at locations a few hundred microns away on the same sample deposition

There are also inconsistencies found in the porous DBR uniformity across the sample. While the samples have a mostly uniform DBR reflecting wavelength, there are differences in the microstructure. The cross-sectioned SEM shows many large pores opening on one side of the ridge. As learned from analysis of the scattering loss in edge

emitting lasers with porous GaN cladding in chapter 3, the largest pores have an outsized effect on scattering. These undoubtedly contribute to increased loss and is likely one of the reasons preventing the devices from reaching laser threshold.

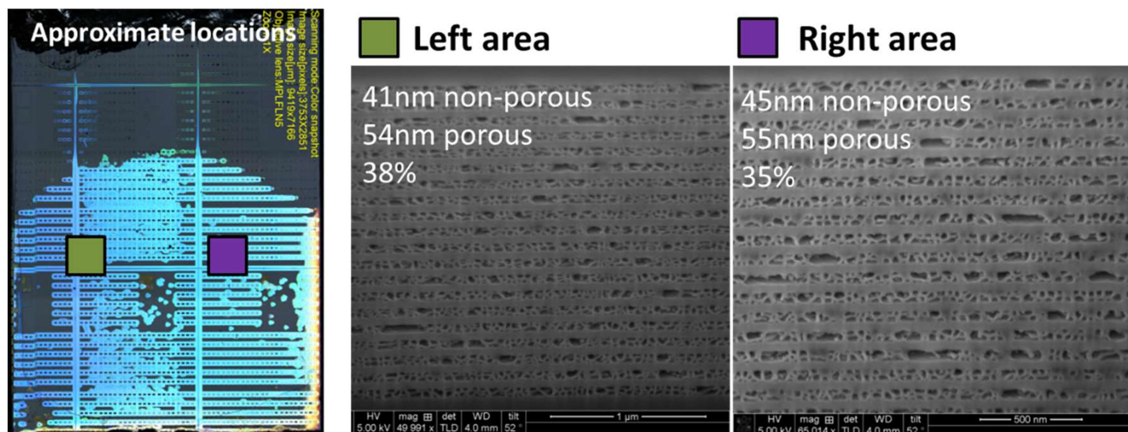

Figure 4-11: Top-down optical microscope image of porous DBR sample including locations of cross sections taken by FIB cut SEM.

Deviations in the porous DBR also led to discrepancies in the reflectivity spectrum. The reflectivity of the porous DBR below the laser stack did not match calculated reflectivity for a DBR underneath a laser cavity. As can be seen from the measured data, the peaks are spaced a little wider than the model, but there are extra oscillations at the top of the stop band. If this were truly near 100% reflective, the peak of the DBR stopband should be nearly flat as in the model.

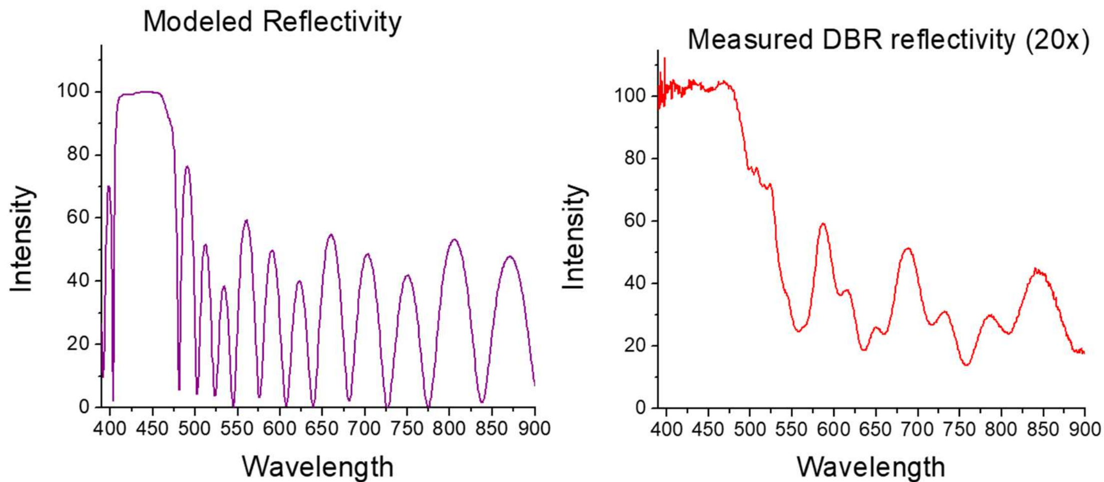

Figure 4-12: Calculated reflectivity spectrum for porous GaN DBR and laser layer stack (using VAT for porous layers) compared to measured reflectivity spectrum

This evidence is presented to call into question the actual strength of the porous DBR. VCSELs depend on mirrors with more than 99.5% reflectivity and are nearly impossible to make when the variation is as high as we have seen, and when the measurement sensitivity is lacking.

4.5 Conclusions and future work

Porous GaN DBRs with high reflectivity were fabricated, though they still have issues with uniformity and occasionally very large pores. It is difficult to determine the true reflectivity given the current measurement setup. Hybrid VCSEL devices were fabricated with a lower porous GaN DBR and an upper dielectric DBR. While there was evidence of spectral emission narrowing, they did not reach laser threshold. Uniform porous DBRs need to be engineered to produce more predictable reflectivity spectra. A more reliable way to measure reflectivity over a small area is also needed. Once the mirror is fixed, other issues

improving the design, contact, and material quality will follow and it is likely UCSB will be able to fabricate a porous GaN VCSEL.

5. Mechanically relaxed templates via porous GaN on silicon substrates

Nascent technologies associated with µLED displays rely on color mixing of direct emission red, green, and blue emitters. While blue and green LEDs based on GaN have high brightness and efficiency, efficiency drops at longer wavelengths (ie red) due to material lattice mismatch, QCSE, and indium decomposition at high MOCVD growth temperatures. AlInGaP based LEDs have a clear advantage in efficiency over III-Nitride LEDs at red wavelengths, such as 630 nm, but succumb to issues with sidewall recombination and heating effects in devices with very small dimensions. AlInGaP LED performance decreases when mesa edge length drops below 100 µm, but nosedives under 20 µm in the dimensions needed for µLED displays [80]. While GaN LEDs have higher efficiency at these dimensions, they are still sub-par at only ~3% EQE. Increasing quantum efficiency of long wavelength LEDs is an active area of development [81].

Fixing the green gap requires increasing the indium composition in the quantum wells while maintaining high efficiencies. The lattice mismatch between GaN and InGaN is a severe problem hindering efficiency and leading to defect incorporation into the crystal. Growing quantum wells on top of a relaxed InGaN template avoids the additional strain induced with InGaN on GaN. There are several methods employed by researchers in III-Nitride material growth to develop a relaxed InGaN template for growing efficient long

wavelength InGaN emitters. Not only does a relaxed InGaN template avoid additional strain associated with InGaN on GaN, but it also relies on the indium “compositional pulling” effect [82] to allow growth at hotter temperatures. The compositional pulling effect is observed when growing thick InGaN layers: higher percentage InGaN layers beget higher indium incorporation during growth. This means that the temperature can be increased to incorporate the same amount of indium before layer degradation. Several groups have used this technique with mixed success, hindered by defects in the high indium content templates [83]. Recently, research out of UCSB demonstrated a high indium content decomposition layer allowing growth of relaxed templates [84]. This work is immature but holds a new avenue for the development of long wavelength III-nitride emitters.

While significant discussion has been made in this thesis about the optical advantages of using porous GaN in optoelectronic devices, it can be used for mechanical compliance to create relaxed templates with high indium content. Pasayat *et al* used highly porous GaN material under etched mesas as a mechanically compliant layer allowing strain relief for InGaN material. Full µLEDs were grown and fabricated on the relaxed porous templates resulting in 2.5% EQE, among the highest reported in literature [46-48] at these dimensions.

5.1 Development of relaxed InGaN on silicon substrates

Initial porous GaN results were on were on sapphire substrates, but the enormous capacity and portfolio for silicon based technology and global fabrication facilities offer major research and manufacturing advantages for LEDs heterogeneously fabricated on

silicon. LEDs grown on silicon substrates have been pioneered with strain engineering by using buffers of various III-nitride compositions, including AlN and AlGaN [85]. The following experiments targeted improved performance of GaN μLEDs at longer wavelength grown on silicon substrates with strain engineered templates.

5.1.1 Relaxed InGaN tiles

Porous GaN was first implemented below basic bulk InGaN films to measure the change in strain states. Basal plane GaN-on-Si templates were purchased by Enkris with a proprietary AlGaN/AlN based buffer capped with nGaN. On top of that was nGaN with requested Si doping levels designed to be used as mechanically compliant porous layer. The samples were prepared with BHF, aqua regia, and solvent cleaning before growing a 200 nm InGaN superlattice (SLS) on the top surface at 960 °C. The SLS comprised of 8 loops alternating 20 nm of $In_{0.07}Ga_{0.93}N$ followed by 5 nm of GaN designed in a way minimize natural relaxation mechanisms. Samples were then patterned into squares at μLED relevant dimensions and etched with a Cl_2 reactive ion etch. There were 10 μm streets between the square mesas. Indium was soldered onto the edge of the sample which was electrochemically etched to create the porous GaN layer at 14 V for 15 min. Etch conditions were chosen for high porosity with large pores to promote mechanical compliance and stretching for the following layers.

Several parameters were varied to understand the relaxation mechanism. Three separate growths varied the InGaN SLS thickness from 200 nm, dropping 2 loops to 150 nm, and then two more loops to 100 nm. Several pieces were put into the 200 nm growth

to vary the mesa and etch conditions. Mesa size was varied to have edges of 4 µm, 6 µm, and 8 µm. A final sample was also etched at a higher voltage of 18 V.

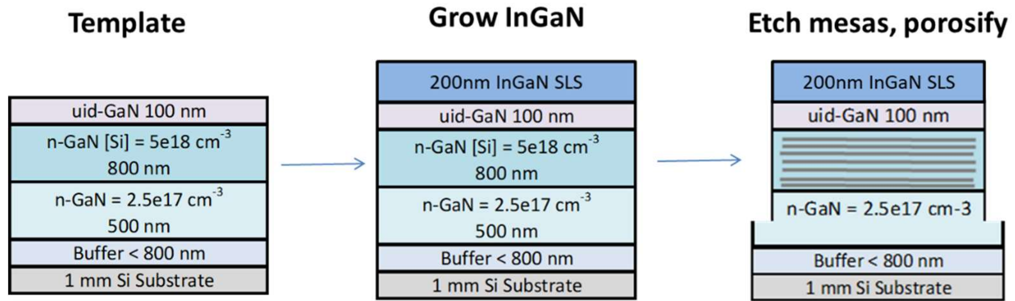

Figure 5-2: Process flow diagram for RSM measurement test structures

Degree of InGaN relaxation was measured with x-ray diffraction (XRD) reciprocal space mapping (RSM) at each stage of the process. This was a (ω-2θ)-ω scan over the off-axis (-1-124) reflection. The three central peaks correspond to AlGaN in the buffer, GaN, and InGaN from top to bottom. The locations of the GaN and InGaN peaks were used to get the degree of relaxation of the InGaN layer. The lattice constants of a_{GaN} = 0.31893 nm and a_{InN} = 0.3538 nm were use with Vegard's Law and relaxation percent to estimate the lattice constant of the InGaN layer.

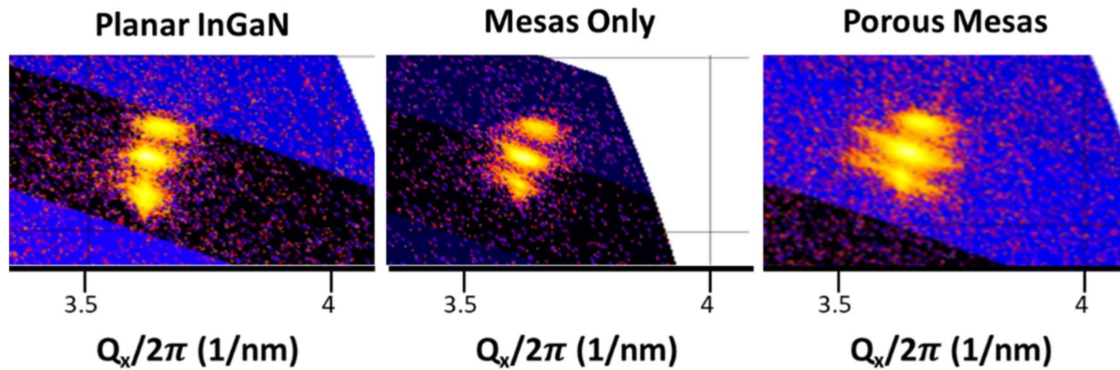

Figure 5-3: Representative reciprocal space map of a sample after growth, after etching mesas, and then after porosifying mesas.

The scans were performed immediately following growth of the InGaN layer (called planar), after etching mesas, and following the electrochemical etch of the highly doped layer into porous GaN. The large thickness and high indium content of the InGaN SLS exhibits partial relaxation even before patterning mesas, around 10%. This drastically increases after etching 6 µm square mesas to 30%. The edges of the mesa expand outward with the larger lattice constant due to increased indium content. Electrochemically etching these samples enhanced the magnitude of relaxation even further. Etching at 14 V raised relaxation to ~50%, and the higher porosity 18V etch increased the relaxation to 65%. Though not fully relaxed, evidence that the compliant porous layer is flexible allowing the compressively strained InGaN layer to expand.

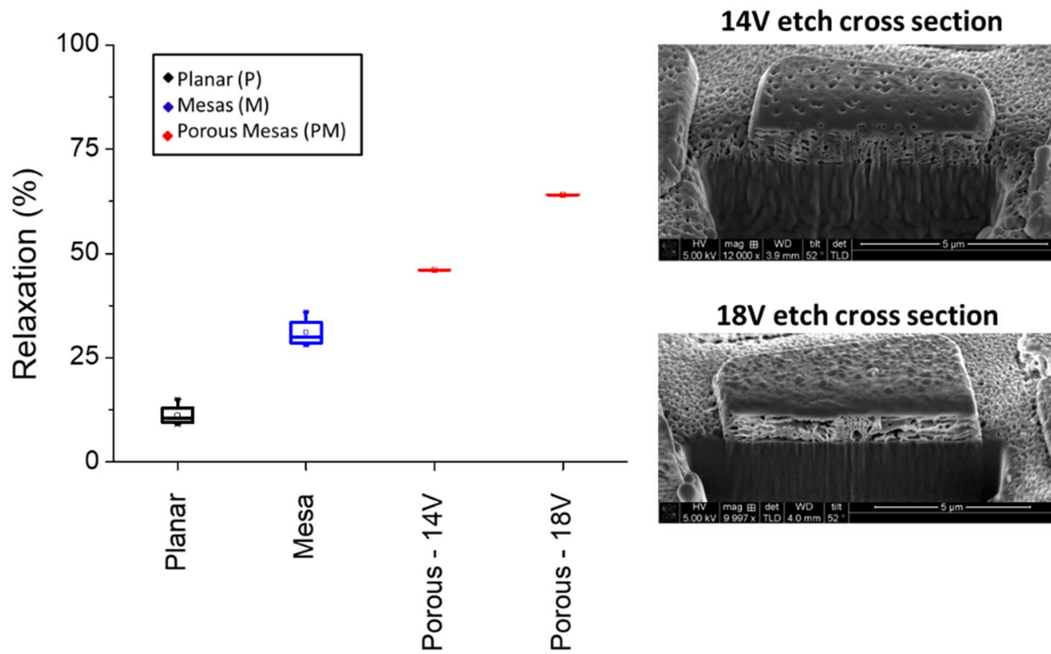

Figure 5-4: Relaxation measured for planar 200nm thick InGaN layer, then after etching 6 µm square mesas, and finally after electrochemically etching. SEM on the right are FIB cross sections of different etch voltage porous layers. The higher voltage etch led to higher porosity in the compliant layer.

The trend was repeated in samples with thinner InGaN layers. All were 6 µm squares etched at 14 V, confirming increasing levels of relaxation by etching mesas and then porosifying. An interesting subtlety was seen decreasing the thickness of the InGaN SLS which showed a reduction in relaxation. This agrees with the expectation that a thicker layer would have higher strain relieved by the porous GaN mechanism.

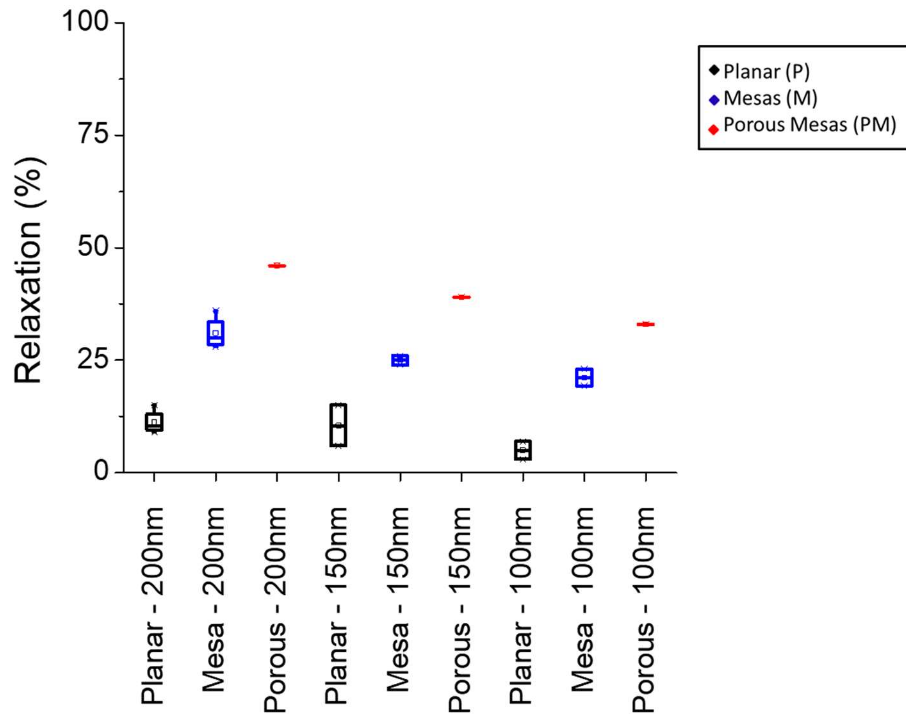

Figure 5-5: Relaxation of thinner InGaN

Comparing 200 nm InGaN layers at 14 V but varying the mesa size elaborated even further on the relaxation mechanism. In the 4 µm case, simply etching the mesas led to almost 50% relaxation and no additional relaxation was seen from porosification. This may suggest that 4 µm is a small enough mesa to allow maximum 2D relaxation of the strained InGaN layer. Conversely, the opposite trend is seen for the larger 8 µm mesas. Almost no relaxation is seen after etching the mesa, but a large relaxation happens after porosification, increasing to ~60%. While this is only a few samples, the trend implies that electrochemical etching of porous GaN likely only helps for µLEDs on the order of about 5µm or larger.

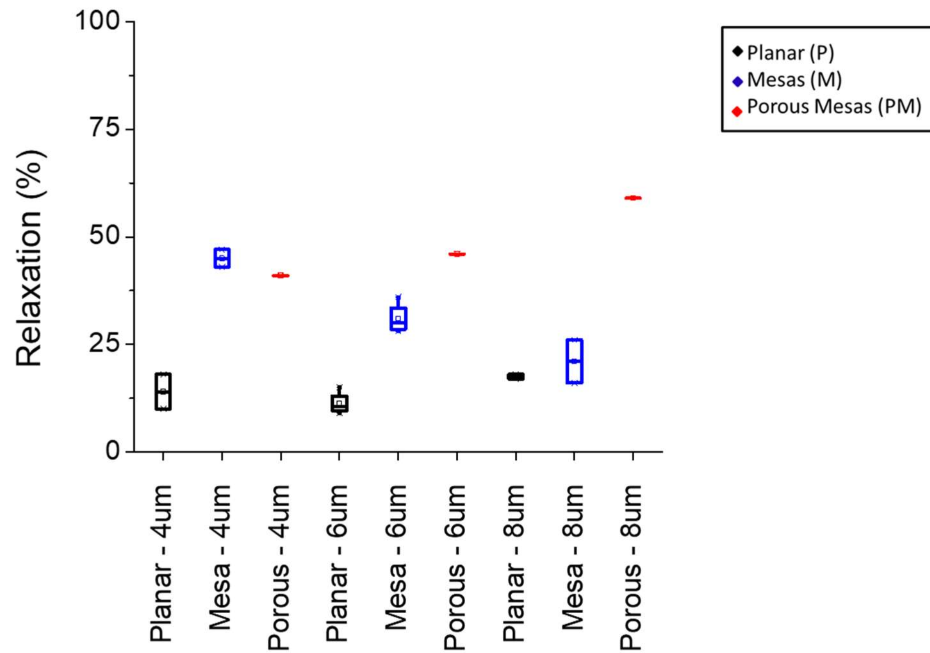

Figure5-6: Relaxation varying mesa size

5.1.2 Wavelength shifted MQWs

The samples with 60% relaxation (6 µm, 200 nm InGaN, 18V) were then prepared for regrowth by cleaning with aqua regia, BHF, and solvents. A single growth was done with 4 quantum well loops at 10 nm barriers and 3 nm wells, ending on a barrier at 870 °C targeting blue emission. An identical structure was grown but at 850 °C targeting green emission. Both growths included a planar sample, one with mesas, and one with porous mesas.

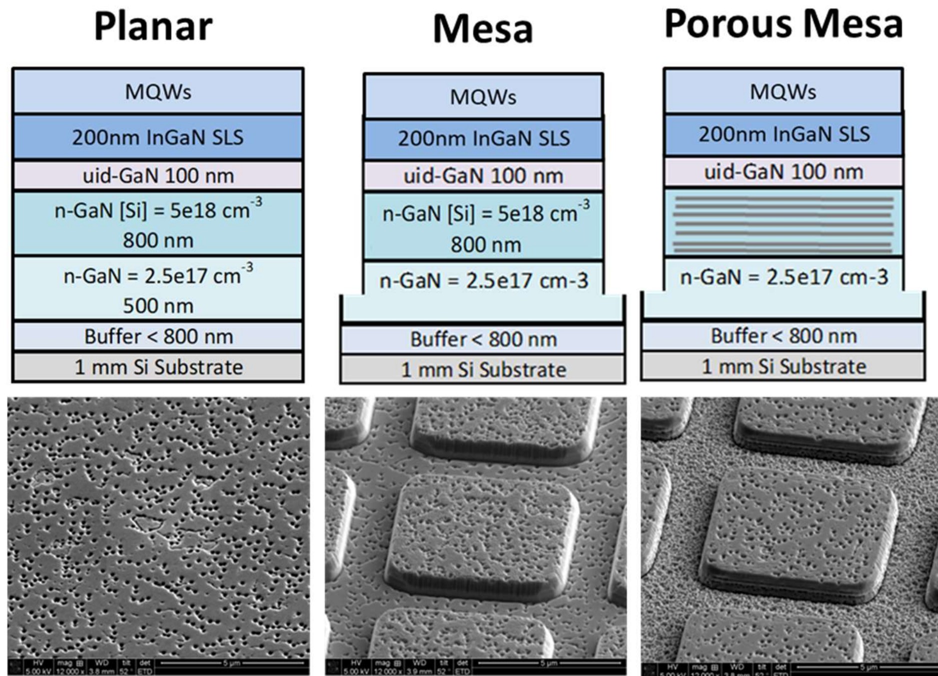

Figure 5-7: Structures and SEM images of wavelength shift experiment.

The relaxed InGaN samples are expected to incorporate more indium content into the quantum wells resulting in a wavelength red shift by photoluminescence. Macro-photoluminescence was extremely dim and did not imply this trend. In both cases, the mesas-only sample showed a wavelength blue-shift from the planar sample, opposite to the expected trend. In the experiment targeting blue emission, the porous sample did have a small shift longer into green, but the signal was very weak. The experiment targeting green showed extremely washed-out emission for the porous sample and no redshift.

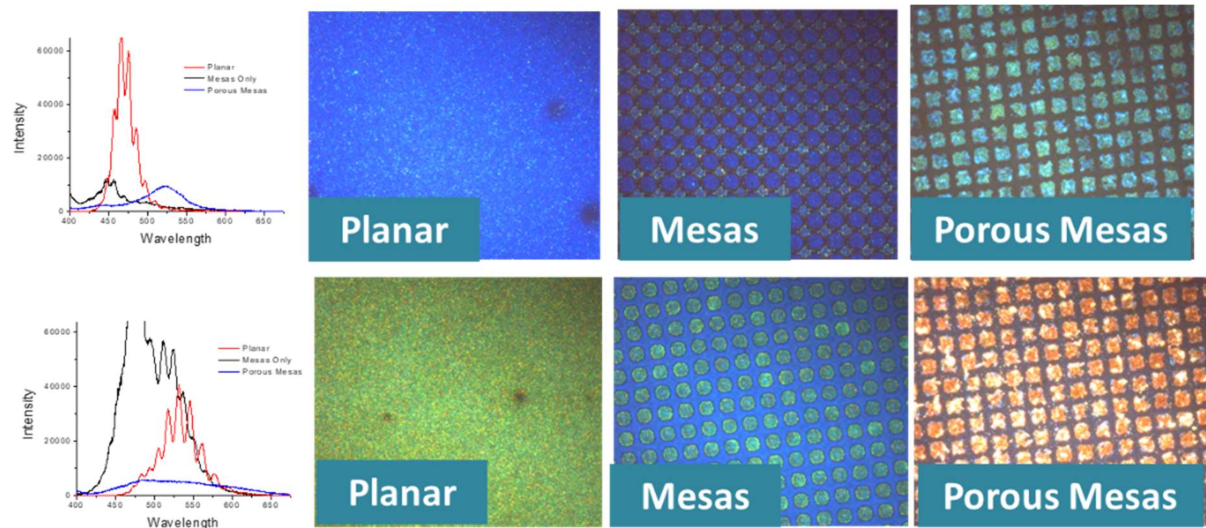

Figure 5-8: Macroscopic photoluminescent spectrum for each growth is on left. While there is no trend in the measured spectra, the micro-PL shows longer emission from the mesas and porous mesas in both cases.

Closer inspection of the samples by optical microscope revealed the blue-shifted emission of the mesas-only sample came from the streets and not the mesa, areas that are not relaxed. It also presented the porous mesas were wavelength red shifted - the hotter quantum wells case showed porous mesas emitting cyan, and the colder quantum wells showed porous mesas emitting orange. The emission was just too weak to be detected by the spectrometer, and very non-uniform. The apparent red shift on the porous mesas fit with our expected trend of higher indium incorporation on the samples with higher relaxation. Despite the weak emission, we continued processing LEDs to investigate behavior under electroluminescence.

5.2 µLED Fabrication

Relaxed porous mesas were prepared similar to the relaxation experiments except on a mask with space for µLED features and with several mesa sizes. Following porosification at 18 V for 15 min, samples were cleaned to prepare for MOCVD regrowth of a full LED stack. Starting with 150 nm of nGaN low doped at $2x10^{18}$ cm^{-3} grown at 920 °C, a 30 loop $In_{0.03}GaN_{0.97}N$/GaN superlattice was grown with approximately 2.5 nm thickness each. A 5-loop multiple quantum well was grown with 3 nm wells 850 °C targeting cyan emission, and 12 nm barriers at 950 °C. The temperature was kept at 950 °C to grow a 10 nm pAlGaN electron blocking layer doped with 9×10^{19} cm^{-3} of Mg. Finally, a 100 nm pGaN was grown at $5x10^{19}$ cm^{-3} doping capped with 10 nm at very high doping for electrical contact (estimated at $2x10^{20}$ cm^{-3}). Layer thicknesses were checked through XRD peaks of test growth individual layers and doping was verified by SIMS. Peculiar growth fronts were observed extending outward from the mesas. Under optical inspection and photoluminescence, the porous mesas can be seen to emit brighter and potentially longer wavelength than areas of the sample where the mesas remain bulk crystalline.

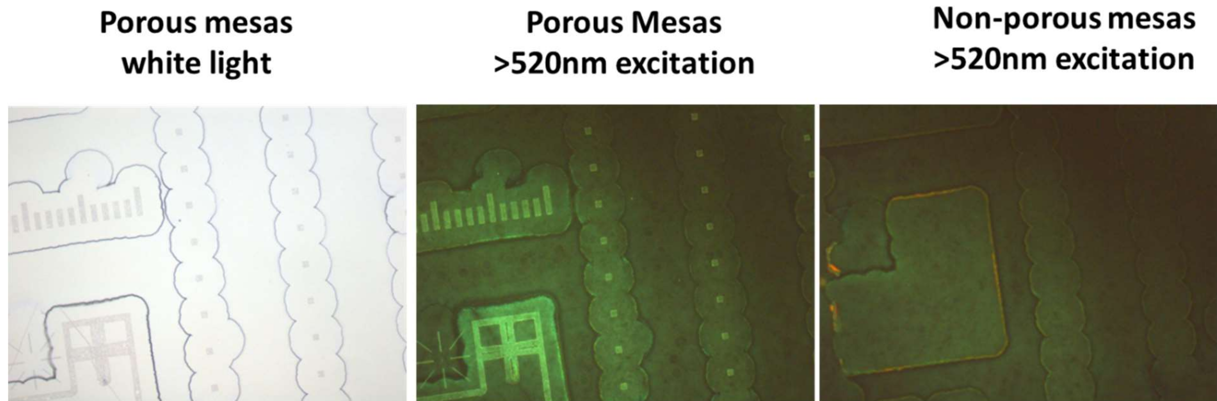

Figure 5-9: Optical images of LED material after growth. Porous mesas appear brighter and shifted longer than non-porous mesas under 520nm excitation

Samples were activated in atmospheric conditions at 600 °C for 15 min before being fabricated into chips according to [48]. 100 nm of ITO was blanket deposited by electron beam evaporation for the p-contact, and reactive ion etching with MHA was used to remove ITO in the field. A $SiCl_4$ based reactive ion etch was then used to etch mesa exposing the nGaN. The edge sidewalls were passivated with 30 nm of Al_2O_3 deposited by electron beam evaporation and 180 nm of SiO_2 deposited by ion beam deposition. These were etched in areas needed for n- and p-contacts, and finally metal was evaporated for probing pads in a 15 nm Ti/ 1 µm Au stack.

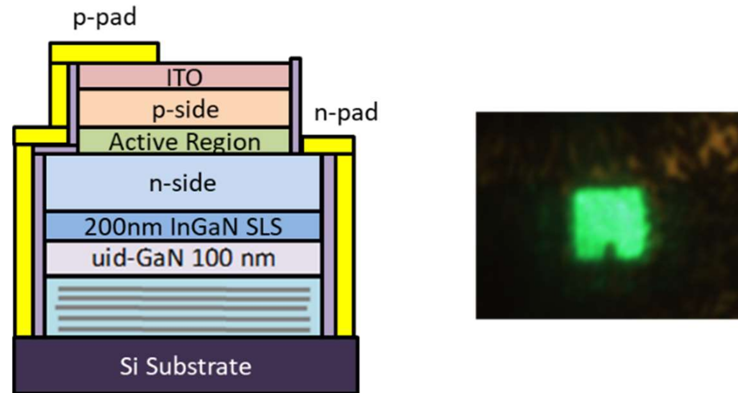

Figure 5-10: Fabricated µLED layer stack and optical microscope image of 4µm porous LED electrical testing.

Samples were tested with electrical injection for electroluminescent properties. Yield was very low, with only ~5% of devices emitting light for both the porous and non-porous mesas on the sample. Failing samples exhibited open circuits. The porous LEDs exhibit very high leakage current with a high rate of infant mortality. We speculate misalignment of the p-contact metal was the reason behind a majority of the leaky devices. It is also believed higher growth surface area of the porous sample may have led to thinner layers. Thinner barriers and electron blocking layer could explain a portion of the leaky porous devices, but this needs further investigation. The porous devices also have flickering, mottled emission, and inconsistent measurements.

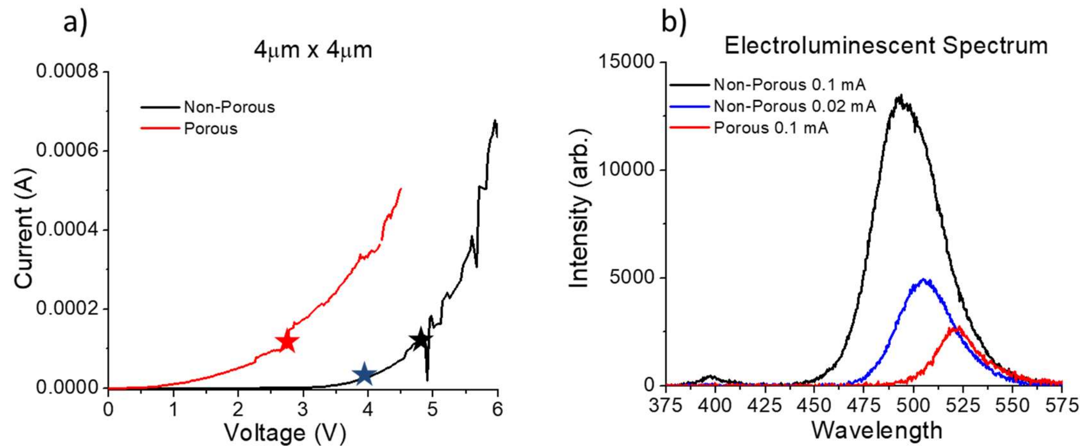

Figure 5-11: Electrical testing measurements for µLED devices. a) Current-density plots comparing the porous µLED to non-porous. Stars indicate the current densities measured in the b) electroluminescent spectrum. The non-porous spectrum was taken at two current densities for a better comparison with the porous µLED emission.

The most consistent measurements came from two 4 µm x 4 µm LEDs on top of 6 µm porous mesas. Higher current densities in the active region blue-shift the wavelength, so any comparison of the wavelength needs to be at the similar current density. This is confounded by the high leakage current of the porous µLEDs, making wavelength comparisons difficult. There is a measured redshift in the wavelength of the porous GaN LEDs of 20-40 nm that we attribute to the higher indium incorporation on a relaxed template, but the exact amount is hard to tell until the leakage current can be fixed. We attempted to measure power out of the topside of the device with an integrating sphere, but it was below the measurement limit of a 10 µW even at high current densities. The power is inhibited by the absorbing silicon substrate, which must be removed with a flip-chip fabrication scheme to get an favorable power measurement.

5.3 Strain relaxed template conclusions

Porous GaN has been used as a mechanically compliant strain relief layer on silicon substrates. While significant relaxation levels were achieved validating past reports on sapphire, quantum wells grown on the relaxed substrates produced dim emission and only achieved a small wavelength red-shift. Micro-LEDs were fabricated showing the red-shift in the electroluminescent spectrum, but power was immeasurably low. There were significant problems with the electrical characteristics and yield of the porous GaN µLEDs. While the wavelength red-shift is interesting, further work is needed to eliminate current leakage and attempt a new device geometry to know how effective porous GaN could be at improving LEDs at longer wavelengths.

6. Conclusions, Outlook, and References

6.1 Other potential porous GaN devices

The availability of tight control over the refractive index using NP-GaN lends itself to a wide variety of new device designs such as seen in other material systems. One example is using a graded index separate confinement heterostructure (GRINSCH) from GaAs based lasers. If pore size can be decreased to low scattering levels, there may be benefits to utilizing a graded porous layer like a graded refractive index separate confinement heterostructure [86]. In this design, the alloy is graded next to the quantum wells from AlGaAs to GaAs. This can lead to better optical confinement based on the change in the refractive index as well as an improvement to carrier confinement by altering the band gap

to "funnel" carriers into the quantum well, giving a lower threshold and improved efficiency. A similar method could be employed on NP-GaN lasers by grading the silicon levels during growth to grade the porosity.

There are a few issues using NP-GaN in a GRINSCH laser. The porous GaN grade in refractive index can only be achieved from one side of the quantum well (the n-side), so any improvement is cut in half from what is observed in GaAs GRINSCH lasers. Using a tunnel junction contact on the p-side may be able to get around this but would require protection of the highly doped tunnel junction during the electrochemical etch – not a trivial problem to solve. Although there could be an improvement to the optical confinement, the band gap of NP-GaN will not be graded towards the quantum barrier and will not provide a carrier funneling effect. The last problem is that the highest porosity layers would need to be pushed up right next to the QW, a major source of scattering and heat generation. The massive scattering loss is likely a deal breaker, unless the porous material can be kept with pores below ~10 nm.

Heat dissipation is a major issue with porous devices, and may be improved by controlling the lateral porosification depth. In this way, heat can conduct around the porous layer, like what is seen in thermal flow of GaN VCSELs between low conductivity dielectric DBRs [74,87]. There are improvements that can be made to the porous GaN VCSEL first made in [42]. In their structure, the NP-GaN undercuts the entire mesa. This feature hinders heat dissipation, a possible reason for lack of continuous wave performance. A novel VCSEL structure could be designed with NP-GaN undercutting only

the aperture, leading to better heat removal from the device and enabling better performance

Using a highly doped nGaN DBR (before electrochemically porosifying), a semi-enclosed circle could be patterned for etching or depositing a current aperture. In this way, during the electrochemical etch, the NP GaN will stop right at the edge of the aperture leaving bulk material around the side of the VCSEL for heat to escape. Next, the VCSEL epitaxial structure will be regrown on top and a standard VCSEL can be fabricated [79]. Porosification can take place after defining the mesa.

Another interesting development can be envisioned by surrounding the active region area with a full circle of NP GaN creating a NP GaN aperture, similar to oxide defined apertures in GaAs lasers. Though not an effective current aperture, NP GaN used as an optical aperture could be coupled with ion implantation or a buried tunnel junction to improve single mode efficiency. This would take some minor alterations in the fabrication scheme, by switching the ion implantation, aperture etch, and BTJ regrowth steps, it may be possible to etch the BTJ into NP GaN in an area surrounding the aperture. This could provide better optical confinement in the transverse direction, though would likely take additional development steps.

NP GaN could be used as a mirror in micro-cavity LEDs for extraction benefits by forming NP GaN mirrors. Micro-cavity LEDs (MCLEDs) have potential for greatly improving extraction efficiency and directional LED efficiency. As they need only a small amount of reflectivity, previous attempts have used metal mirrors to some benefit [29] but are difficult to process. Using a few period NP-GaN DBR mirror could be a key development in

improving the extraction efficiency in an MCLED. In this case, NP-GaN mirror conditions would need to be optimized in a similar way to the DBR for the VCSEL structure, then could be put in a simple MQW LED structure designed in the MCLED thickness regime.

Finally, there could be advantages to using NP GaN as a liftoff layer that remain unexploited. Many groups incorporate a sacrificial InGaN layer into growth in conjunction with a photo-electrochemical etch (PEC) process for liftoff [79] in flip-chip processing. Forming NP-GaN requires highly doped layers instead of strain-inducing InGaN layers, which can improve quality of layers grown on top of them in the epitaxial stack. While it has been shown that NP-GaN can be used as a sacrificial layer for simple liftoff in flip-chip process flows [45], the liftoff mechanism required regrowth in an MOCVD chamber to transform the NP-GaN into pillars. MOCVD is a transient process, and adjustments made to improve an LED structure will affect the NP-GaN transformation and may be difficult to reproduce. An improved process would porosify the sacrificial layer after full growth of the LED stack, and either fully electropolish the NP-GaN with a high voltage EC etch, or instead transform into pillars with an anneal or other processing step.

6.2 Conclusions and Future Directions

This work showed porous GaN being used in visible edge emitting laser diodes, vertical cavity surface emitting lasers, and strain relaxed µLEDs.

In EELDs, the porous GaN was shown to exhibit lateral optical confinement of a lasing mode as well as cladding for vertical confinement in both blue and green lasers. Parasitic etching during the electrochemical etch was a critical problem requiring

engineering of the silicon doping in the layer stack to achieve high etch selectivity. Any parasitic etch paths are detrimental to laser performance from scattering in pores near the active region. Fixing the etch selectivity in the green lasers reduced internal loss even though the mode was less confined and should have seen higher loss due to absorption. Scattering from the porous cladding is problematic but can be kept low with small pore sizes and high porosity to reduce the overlap of the optical field.

Other properties of the porous GaN were investigated for how significantly they impact EELD performance. The electrical conductivity of the porous GaN material was found to be low for optimal driving of the device, but not low enough for a current aperture. The thermal conductivity of the porous GaN is also low, a fundamental issue with no obvious solution. Although laser behavior was seen under continuous wave electrical injection for the blue lasers, it rolls over quickly due to heat generation. It was also not achieved for green lasers in part because of the resistive porous GaN.

Green EELDs with porous GaN cladding were comparable to some of the best lasers fabricated at UCSB with similar threshold current density and much lower voltage, but lag far behind state of the art. The p-side needs optimization to fix the low injection efficiency, and reducing the losses associated with absorption needs to be a priority to drop the threshold and improved the slope efficiency. Lasers targeting 589 nm emission were modeled comparing porous GaN with lattice matched InAlN cladding indicating the potential for similar performance. Further design work will be needed, but porous GaN cladding could be a fruitful path to ultimately broaden the applicable wavelength of GaN EELDs.

The optical properties of porous GaN were used to create distributed Bragg reflector mirrors. While they exhibit over 95% reflectivity, issues with uniformity, large pores, and inconsistent measurements make it difficult to evaluate the true performance near 100% reflectivity. These mirrors were used to fabricate an LED capped with a dielectric DBR to form a cavity for a VCSEL, though laser behavior was not achieved. We conclude that the measurement and uniformity issues with the porous DBR need to be fixed before development of the cavity, and a VCSEL will soon follow.

The mechanical properties of porous GaN were leveraged to create strained relaxed InGaN templates on silicon substrates for long wavelength µLED applications. $In_{0.07}Ga_{0.93}N$ layers were grown and measured with 65% relaxation on top of porous GaN layers on silicon templates. MQWs grown on these samples appeared to have a wavelength redshift investigated under optical fluorescence, though the emission was very dim. µLEDs were fabricated on top of the relaxed porous mesas to test electroluminescent properties. Although they showed potentially red-shifted wavelength from the relaxed templates, leakage current on the porous mesas was too high for a useful device and the power was so low as to be immeasurable by our integrating sphere setup. Development of the device geometry for small mesas is needed to fix the leakage on the porous mesas. Growth on top of the porous mesas also needs investigation to better understand the front seen in the LED regrowth. While there may be opportunities to achieve higher efficiency at longer wavelengths, significant development is needed with potential be size limitations.

6.3 References

1. “LED adoption report”, <https://www.energy.gov/eere/ssl/led-adoption-report>, (21 June 2022)
2. “U.S. renewable electricity generation has doubled since 2008”, <https://www.eia.gov/todayinenergy/detail.php?id=38752#:~:text=U.S.%20solar%20generation%20has%20increased,installations%20or%20utility%2Dscale%20installations>, (21 June 2022)
3. Claude Weisbuch 2020 ECS J. Solid State Sci. Technol. **9** 016022
4. “Google acquires Raxium”, <https://blog.google/inside-google/company-announcements/google-acquires-raxium/>, (21 June 2022)
5. “Facebook renames itself Meta”, <https://www.nytimes.com/2021/10/28/technology/facebook-meta-name-change.html#:~:text=The%20social%20network%2C%20under%20fire,digital%20frontier%20called%20the%20metaverse.&text=As%20a%20subscriber%2C%20you%20have,can%20read%20what%20you%20share.>, (21 June 2022)
6. “MICRO LIGHT EMITTING DIODE (LED) MARKET - GROWTH, TRENDS, COVID-19 IMPACT, AND FORECASTS (2022 - 2027)”, <https://www.mordorintelligence.com/industry-reports/micro-led-market>, (21 June 2022)
7. “MicroLED displays could disrupt LCD and OLED supply chains”, <https://www.electronicspecifier.com/products/displays/microled-displays-could-disrupt-lcd-and-oled-supply-chains>, (21 June 2022)
8. “What is Light Fidelity?”, <https://lifi.co/what-is-light-fidelity-technology/>, (21 June 2022)
9. “Smart adaptive headlights are finally coming to the US”, <https://www.theverge.com/2022/2/17/22937489/nhtsa-allows-adb-adaptive-driving-beam-technology>, (21 June 2022)
10. Lantian Mi, Chao Ping Chen, Yifan Lu, Wenbo Zhang, Jie Chen, and Nizamuddin Maitlo, "Design of lensless retinal scanning display with diffractive optical element," Opt. Express 27, 20493-20507 (2019)
11. Sangu, S., Shimokawa, T. and Tanaka, S., “Ultracompact eye and pupil tracking device using VCSEL arrays and position sensitive detector,” Opt. Archit. Displays Sens. Augment. Virtual, Mix. Real. (AR, VR, MR) 11310, B. C. Kress and C. Peroz, Eds., 50, SPIE (2020).
12. “LED Basics: Electrical properties”, < https://sites.ecse.rpi.edu/~schubert/Light-Emitting-Diodes-dot-org/chap04/chap04.htm>, (21 June 2022)
13. L. Coldren, S. Corzine, and M. L. Masanovic, 2012 *Diode Lasers and Photonic Integrated Circuits,* 2nd ed. (Wiley, 2002)
14. Emmanouil Kioupakis, Qimin Yan, and Chris G. Van de Walle , "Interplay of polarization fields and Auger recombination in the efficiency droop of nitride light-emitting diodes", Appl. Phys. Lett. 101, 231107 (2012) “Title”, <url>, (21 June 2022)
15. Wierer, Jonathan & Tsao, Jeff & Sizov, Dmitry. (2013). Comparison between blue lasers and light-emitting diodes for future solid-state lighting. Laser & Photonics Reviews. 7. 10.1002/lpor.201300048.
16. P. Blood, G. M. Lewis, P. M. Smowton, H. Summers, J. Thomson and J. Lutti, "Characterization of semiconductor laser gain media by the segmented contact method," IEEE Journal of Selected Topics in Quantum Electronics 9, 5, 1275-1282 (2003)
17. Basil W. Hakki and Thomas L. Paoli , "cw degradation at 300°K of GaAs double-heterostructure junction lasers. II. Electronic gain", Journal of Applied Physics 44, 4113-4119 (1973)
18. Zhu, D. and Humphreys, C. J., “Solid-state lighting based on light emitting diode technology,” [Optics in Our Time], Springer International Publishing, 87–118 (2016).
19. “GaN – Gallium Nitride Band structure and carrier concentration”, <http://www.ioffe.ru/SVA/NSM/Semicond/GaN/bandstr.html >, (21 June 2022)
20. Mashita, M. T. and S. O. and M. M. and M. (1987). On the Reaction Mechanism of the Pyrolyses of TMG and TEG in MOCVD Growth Reactors. Japanese Journal of Applied Physics, 26(5A), L564.

21. Denbaars, S. P., Feezell, D., Kelchner, K., Pimputkar, S., Pan, C. C., Yen, C. C., Nakamura, S. (2013). Development of gallium-nitride-based light-emitting diodes (LEDs) and laser diodes for energy-efficient lighting and displays. Acta Materialia, 61(3), 945–951.
22. Mishra, H. X. and D. S. G. and H. Y. and T. M. and P. K. and S. K. and S. P. D. and U. K. (2003). Memory Effect and Redistribution of Mg into Sequentially Regrown GaN Layer by Metalorganic Chemical Vapor Deposition. Japanese Journal of Applied Physics, 42(1R), 50.
23. “Aixtron expands MOCVD market share to 75% in 2021”, <http://www.semiconductor-today.com/news_items/2022/may/aixtron-250522.shtml#:~:text=According%20to%20 the%20report%20'Semiconductor,%25%20and%2011%25%2C%20respectively.>, (21 June 2022)
24. “Background Story of the Invention of Efficient Blue InGaN Light Emitting Diodes”, <https://www.nobelprize.org/uploads/2018/06/nakamura-lecture-slides.pdf>, (21 June 2022)
25. Ambacher, Oliver & Angerer, H & Dimitrov, R & Rieger, W & Stutzmann, Martin & Dollinger, Guenther & Bergmaier, Andreas. (1997). Hydrogen in gallium nitride grown by MOCVD. Physica Status Solidi (a). 159. 105-119.
26. Smalc-Koziorowska, Julita & Grzanka, Ewa & Czernecki, Robert & Schiavon, Dario & Leszczyński, Mike. (2015). Elimination of trench defects and V-pits from InGaN/GaN structures. Applied Physics Letters. 106. 101905.
27. Neugebauer, J., & Van de Walle, C. G. (1996). Role of hydrogen in doping of GaN. Applied Physics Letters, 68(13), 1829–1831.
28. Svensk, O. et al. "Effect of Growth Conditions on Electrical Properties of Mg-Doped p-GaN" Journal of Crystal Growth 298 (2007): 811 814.
29. Lundin, W. V, Sakharov, A. V, Zavarin, E. E., Sinitsyn, M. A., Nikolaev, A. E., Mikhailovsky, G. A., Tsatsulnikov, A. F. (2009). Effect of carrier gas and doping profile on the surface morphology of MOVPE grown heavily doped GaN:Mg layers. Semiconductors, 43(7), 963–967.
30. Huseyin Ekinci, Vladimir V. Kuryatkov, Chris Forgey, Amir Dabiran, Robert Jorgenson, Sergey A. Nikishin, Properties of InGaN/GaN MQW LEDs grown by MOCVD with and without hydrogen carrier gas,Vacuum,Volume 148,2018,Pages 168-172.
31. Leonard, J. T. (2016). III-Nitride Vertical Cavity Surface Emitting Lasers, (March).
32. Cheyenne Lynsky, Ryan C. White, Yi Chao Chow, Wan Ying Ho, Shuji Nakamura, Steven P. DenBaars, James S. Speck, "Role of V-defect density on the performance of III-nitride green LEDs on sapphire substrates," Journal of Crystal Growth, Volumes 560–561, 2021, 126048
33. Alexey E. Romanov, Erin C. Young, Feng Wu, Anurag Tyagi, Chad S. Gallinat, Shuji Nakamura, Steve P. DenBaars, and James S. Speck , "Basal plane misfit dislocations and stress relaxation in III-nitride semipolar heteroepitaxy", Journal of Applied Physics 109, 103522 (2011)
34. Matthias Auf der Maur, Alessandro Pecchia, Gabriele Penazzi, Walter Rodrigues, and Aldo Di Carlo Phys. Rev. Lett. 116, 027401 – Published 15 January 2016
35. D. A. B. Miller, D. S. Chemla, T. C. Damen, A. C. Gossard, W. Wiegmann, T. H. Wood, and C. A. Burrus, “Band-Edge Electroabsorption in Quantum Well Structures: The Quantum-Confined Stark Effect,” Phys. Rev. Lett. 53, 2173 – Published 26 November 1984
36. Deng, Z., Jiang, Y., Wang, W. et al. Indium segregation measured in InGaN quantum well layer. Sci Rep 4, 6734 (2014).
37. Chang-Cheng Chuo, Chia-Ming Lee, and Jen-Inn Chyi , "Interdiffusion of In and Ga in InGaN/GaN multiple quantum wells", Appl. Phys. Lett. 78, 314-316 (2001)
38. Y. Nakatsu, Y. Nagao, K. Kozuru, T. Hirao, E. Okahisa, S. Masui, T. Yanamoto, S. Nagahama, "High-efficiency blue and green laser diodes for laser displays," Proc. SPIE 10918, Gallium Nitride Materials and Devices XIV, 109181D (2019)
39. T. Frost, A. Banerjee, K. Sun, S. L. Chuang and P. Bhattacharya, "InGaN/GaN Quantum Dot Red (λ = 630 nm) Laser," IEEE Journal of Quantum Electronics 49, 11, 13795229, (2013)
40. Guoen Weng, Yang Mei, Jianping Liu, Werner Hofmann, Leiying Ying, Jiangyong Zhang, Yikun Bu, Zengcheng Li, Hui Yang, and Baoping Zhang, "Low threshold continuous-wave lasing of yellow-green InGaN-QD vertical-cavity surface-emitting lasers," Opt. Express 24, 15546-15553 (2016)

41. S. Mehari, D.A. Cohen, D.L. Becerra, S. Nakamura, S.P. Denbaars, “Semipolar InGaN blue laser diode with a low optical loss and a high material gain by suppression of carrier accumulation in the p waveguide region,” Jpn. Journal of Applied Physics, 58, 020902 (2019)
42. S. M. Mishkat-Ul-Masabih, A.A. Aragon, M. Monavarian, T.S. Luk, D.F. Feezell, “Electrically injected nonpolar GaN based VCSELs with lattice matched nanoporous distributed Bragg reflector mirrors,” Appl. Phys. Exp. 12, 036504 (2019)
43. B R. ElAfandy, J. Kang, B. Li, T. Kyoung Kim, J. S. Kwak, and J. Han, "Room-temperature operation of c-plane GaN vertical cavity surface emitting laser on conductive nanoporous distributed Bragg reflector", Appl. Phys. Lett. 117, 011101 (2020)
44. C. B. Soh, H. Hartono, S. Y. Chow, S. J. Chua, and E. A. Fitzgerald, “Dislocation annihilation in regrown GaN on nanoporous GaN template with optimization of buffer layer growth Dislocation annihilation in regrown GaN on nanoporous GaN template,” vol. 053112, no. August 2006, pp. 2005–2008, 2012.
45. Yu Zhang, Benjamin Leung, and Jung Han, “A liftoff process of GaN layers and devices through nanoporous transformation,” Appl. Phys. Lett , vol. 181908, no. March, 2012.
46. Shubhra S. Pasayat *et al*, “Demonstration of ultra-small (<10 µm) 632 nm red InGaN micro-LEDs with useful on-wafer externalquantum efficiency (>0.2%) for mini-displays,” 2021 Appl. Phys. Express 14 011004
47. Shubhra S Pasayat *et al*, “Fabrication of relaxed InGaN pseudo-substrates composed of micron-sized pattern arrays with high fill factors using porous GaN,” 2019 *Semicond. Sci. Technol.* **34** 115020
48. Shubhra S. Pasayat, Ryan Ley, Chirag Gupta, Matthew S. Wong, Cheyenne Lynsky, Yifan Wang, Michael J. Gordon, Shuji Nakamura, Steven P. Denbaars, Stacia Keller, and Umesh K. Mishra , "Color-tunable <10 µm square InGaN micro-LEDs on compliant GaN-on-porous-GaN pseudo-substrates", Appl. Phys. Lett. 117, 061105 (2020)
49. Cheng Zhang *et al* ”Toward Quantitative Electrochemical Nanomachining of III-Nitrides,” 2018 *J. Electrochem. Soc.* **165** E513
50. Berg, S., Kutra, D., Kroeger, T. *et al*. “ilastik: interactive machine learning for (bio)image analysis.” Nat Methods 16, 1226–1232 (2019).
51. L. Megalini, D. Becerra, R. Farrell, A. Pourhashemi, J. Speck, S. Nakamura, S.P. Denbaars, D.A. Cohen, “Continuous wave operation of a $(20\bar{2}\bar{1})$ InGaN laser diode with a photoelectrochemically etched current aperture,” Appl. Phys. Express, 8(042701), 2015.
52. P. S. Hsu, F. Wu, E. Young, A. Romanov, K. Fujito, S.P. Denbaars, J. Speck, S. Nakamure, “Blue and aquamarine stress relaxed semipolar$(11\bar{2}2)$ laser diodes,” Appl. Phys. Lett., 103(161117), 2013.
53. M. T. Hardy, S. Nakamura, J. S. Speck, and S. P. Denbaars, “Suppression of relaxation in $(20\bar{2}\bar{1})$InGaN/GaN laser diodes using limited area epitaxy,” Appl. Phys. Lett., 101(24), 2012.
54. G. Yuan, K. Xiong, C. Zhang, Y. Li, and J. Han, “Optical Engineering of Modal Gain in a III-Nitride Laser with Nanoporous GaN,” ACS Photonics, 3(9), 2016.
55. S. Mehari, D.A. Cohen, D.L. Becerra, S. Nakamura, S.P. Denbaars, “Demonstration of enhanced continuous-wave operation of blue laser diodes on a semipolar $(20\bar{2}\bar{1})$GaN substrate using indium-tin-oxide/thin-p-GaN cladding layers,” Opt. Express, 26(2), 2018.
56. FIMMWave V.6.2, Photon Design, Oxford, UK.
57. C. Zhang, S.H. Park, D. Chen, D.W. Lin, W. Xiong, H.C. Kuo, C.F. Lin, H. Cao, J. Han, “Mesoporous GaN for Photonic Engineering-Highly Reflective GaN Mirrors as an Example,” ACS Photonics, 2(7), 2015.
58. C. Zhang, K. Xiong, G. Yuan, and J. Han, “A resonant-cavity blue–violet light-emitting diode with conductive nanoporous distributed Bragg reflector,” Phys. Status Solidi Appl. Mater. Sci., 214(8), 2017.
59. FEMM, “Finite Element Method Magnetics,” http://www.femm.info
60. Lumerical Inc. **MODE**
61. W. Gotz, N.M. Johnson, C. Chen, H. Liu, C. Kuo, W. Imler, "Activation energies of Si donors in GaN," Appl. Phys. Lett. **68** (22), 3144-3146 (1996)
62. M. Kuc, Ł. Piskorski, A.K. Sokół, M, Dems, M, Wasiak, R, P. Sarzała, T, Czyszanowski, "Optical simulations of blue and green semipolar InGaN/GaN lasers," Proc. SPIE 10532 (2018)

63. M. T. Hardy, F. Wu, C.-Y. Huang, Y. Zhao, D. Feezell, S. Nakamura, J. Speck, S. DenBaars, "Impact of p-GaN Thermal Damage and Barrier Composition on Semipolar Green Laser Diodes," IEEE Photonics Technology Letters 26, 1, 43-46 (2014)
64. R. Anderson, Daniel Cohen, Haojun Zhang, Emily Trageser, Nathan Palmquist, Shuji Nakamura, and Steven DenBaars, "Nano-porous GaN cladding and scattering loss in edge emitting laser diodes," Opt. Express 30, 2759-2767 (2022)
65. R. Anderson, D. Cohen, S. Mehari, S. Nakamura, S. DenBaars, "Electrical injection of a 440nm InGaN laser with lateral confinement by nanoporous-GaN," Opt. Express 27(16), 22764-22769 (2019)
66. C. Lynsky, A. Alhassan, G. Lheureux, B. Bonef, S. DenBaars, S. Nakamura, Y. Wu, C. Weisbuch, and J. Speck, Phys. Rev. Materials 4, 054604 (2020)
67. L. Hu, X. Ren, J. Liu, A. Tian, L. Jiang, S. Huang, W. Zhou, L. Zhang, and H. Yang, "High-power hybrid GaN-based green laser diodes with ITO cladding layer," Photon. Res. 8, 279-285 (2020)
68. E. Kioupakis, P. Rinke, C. Van De Walle, "Determination of Internal Loss in Nitride Lasers from First Principles," App. Phys. Exp. 3, 082101 (2010)
69. D. J. Kunzmann, R. Kohlstedt, T. Uhlig, and Ulrich T. Schwarz "Critical discussion of the determination of internal losses in state-of-the-art (Al,In)GaN laser diodes", Proc. SPIE 11280, Gallium Nitride Materials and Devices XV, 112800Y (16 February 2020)
70. M. Vanecek, J. Holoubek, A. Shah, "Optical study of microvoids, voids, and local inhomogeneities in amorphous silicon", Appl. Phys. Lett. 59, 2237-2239 (1991)
71. T. Zhou, C. Zhang, R. ElAfandy, G. Yuan, Z. Deng, K. Xiong, F.-M. Chen, Y.-K. Kuo, K. Xu, and J. Han, "Thermal transport of nanoporous gallium nitride for photonic applications", Journal of App. Phy. 125, 155106 (2019)
72. A. Tamboli, M. Schmidt, S. Rajan, J. Speck, U. Mishra, S. DenBaars, and E. Hu, J. Electrochem. Soc. 156, H47 (2009)
73. J.-F. Carlin, C. Zellweger, J. Dorsaz, S. Nicolay, G. Christmann, E. Feltin, R. Butté, and N. Grandjean, "Progresses in III-nitride distributed Bragg reflectors and microcavities using AlInN/GaN materials," Phys. Stat. Sol. (b), 242, 2326-2344 (2005)
74. R. P. Sarzała, Ł. Piskorski, T. Czyszanowski, and M. Dems, "Influence of Various Bottom DBR Designs on the Thermal Properties of Blue Semiconductor-Metal Subwavelength-Grating VCSELs," Materials 12, 3235 (2019).
75. Hsin-chieh Yu, Zhi-wei Zheng, Yang Mei, Rong-bin Xu, Jian-ping Liu, Hui Yang, Bao-ping Zhang, Tien-chang Lu, Hao-chung Kuo, "Progress and prospects of GaN-based VCSEL from near UV to green emission,"Progress in Quantum Electronics, Volume 57,2018, Pages 1-19
76. Jared A. Kearns, Joonho Back, Daniel A. Cohen, Steven P. DenBaars, and Shuji Nakamura, "Demonstration of blue semipolar (202¯1¯) GaN-based vertical-cavity surface-emitting lasers," Opt. Express 27, 23707-23713 (2019)
77. Masaru Kuramoto *et al*, High-output-power and high-temperature operation of blue GaN-based vertical-cavity surface-emitting laser, 2018 *Appl. Phys. Express* **11** 112101
78. Kearns, J. (2020). Development of Semipolar III-Nitride Vertical-Cavity Surface-Emitting Lasers. UC Santa Barbara. ProQuest ID: Kearns_ucsb_0035D_14842.
79. Kearns, J.A., Back, J., Palmquist, N.C., Cohen, D.A., DenBaars, S.P. and Nakamura, S. (2020), Inhomogeneous Current Injection and Filamentary Lasing of Semipolar (20-21) Blue GaN-Based Vertical-Cavity Surface-Emitting Lasers with Buried Tunnel Junctions. Phys. Status Solidi A, 217: 1900718.
80. Matthew S. Wong, Jared A. Kearns, Changmin Lee, Jordan M. Smith, Cheyenne Lynsky, Guillaume Lheureux, Hyoshik Choi, Jinwan Kim, Chaehon Kim, Shuji Nakamura, James S. Speck, and Steven P. DenBaars, "Improved performance of AlGaInP red micro-light-emitting diodes with sidewall treatments," Opt. Express 28, 5787-5793 (2020)
81. Li, P.; Li, H.; Wong, M.S.; Chan, P.; Yang, Y.; Zhang, H.; Iza, M.; Speck, J.S.; Nakamura, S.; Denbaars, S.P., “Progress of InGaN-Based Red Micro-Light Emitting Diodes.” Crystals 2022, 12, 541.

82. Yuya Inatomi *et al*, “Theoretical study of the composition pulling effect in InGaN metalorganic vapor-phase epitaxy growth,” 2017 Jpn. *J. Appl. Phys*. **56** 078003
83. Amelie Dussaigne *et al*, “Full InGaN red (625 nm) micro-LED (10 µm) demonstration on a relaxed pseudo-substrate,” 2021 *Appl. Phys. Express* **14** 092011
84. Philip Chan *et al*, “Demonstration of relaxed InGaN-based red LEDs grown with high active region temperature” 2021 *Appl. Phys. Express* **14** 101002
85. Dadgar, A. (2015), Sixteen years GaN on Si. Phys. Status Solidi B, 252: 1063-1068.
86. W. Krystek, M. Leibovithc, W.D. Sun, and F. H. Pollak, "Characterization of a graded index of refraction separate confinement heterostructure (GRINSCH) laser structure using contactless electroreflectance", J. of App. Phy. 84, 2229-2235 (1998)
87. C. Forman, S. Lee, E. Young, J. Kearns, D Cohen, J. Leonard, T. Margalith, S. Denbaars, S. Nakamura, "Continuous-wave operation of m -plane GaN-based vertical-cavity surface-emitting lasers with a tunnel junction intracavity contact," App. Phy. Letters. **112**, 071114 (2018)